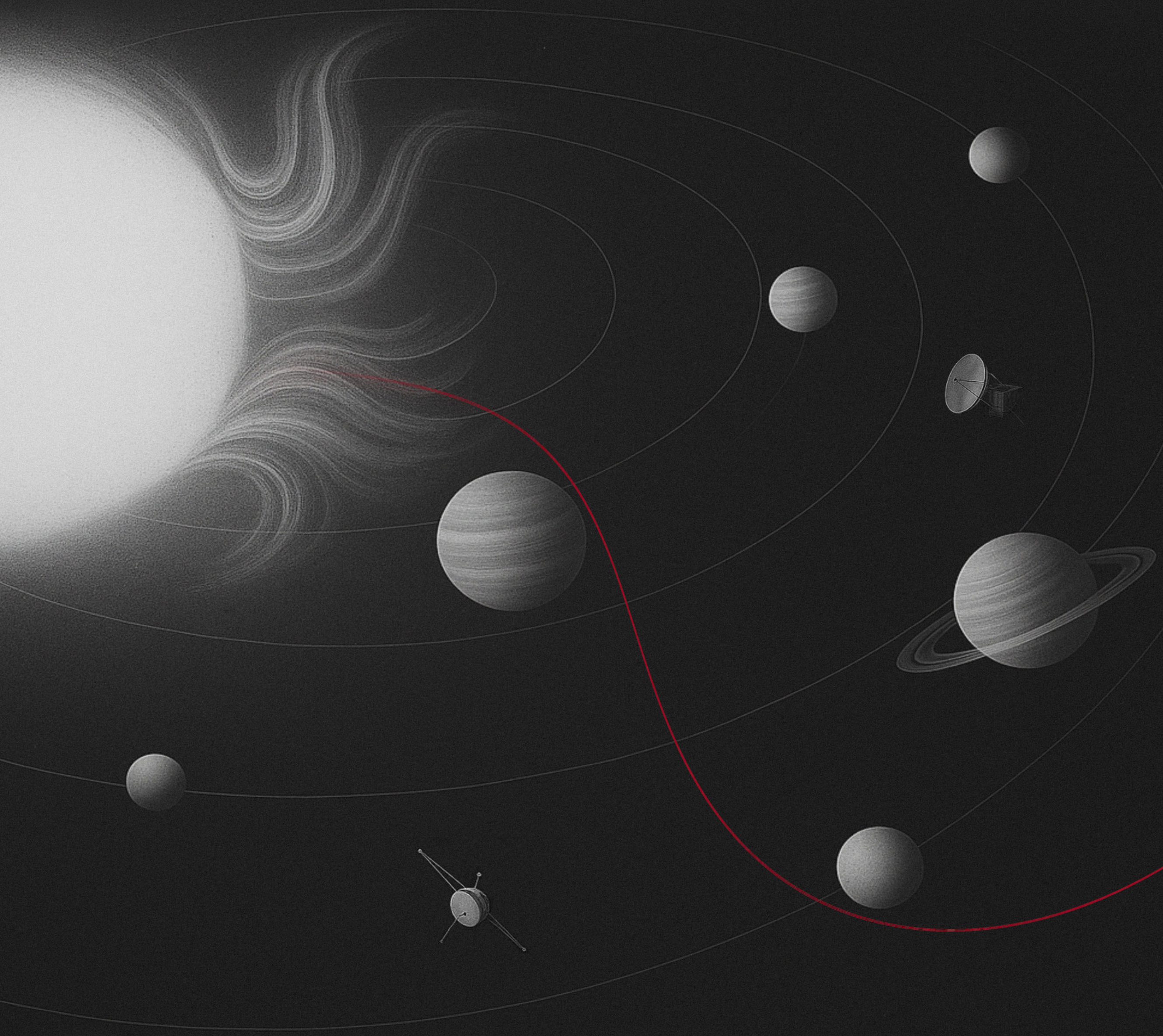

The P-DBM Beyond 1AU:
Forecasting CME arrival in the Whole Heliosphere

Supervisors:
Prof. Dario Del Moro
Prof. Robertus Erdelyi

Ronish Mugatwala
SWATNet ESR

The P-DBM Beyond 1AU:
Forecasting CME arrival in the whole heliosphere

Ronish Mugatwala

UNITOV Metricola: 0316836

UOS Registration Number: 210223257

Registration Date: 01 November 2021

PhD in
Astronomy, Astrophysics and Space Science
PhD Cycle XXXVII

The P-DBM Beyond 1AU: Forecasting CME arrival in the whole heliosphere

by

Ronish Mugatwala

Academic Year 2023/2024

The P-DBM Beyond 1AU: Forecasting CME arrival in the whole heliosphere

by

Ronish Mugatwala

A PhD Thesis submitted to

School of Mathematics and Physical Science,
The University of Sheffield

in partial fulfilment of the requirements for the degree of

Doctor of Philosophy

Year of Submission: 2025

Ronish Mugatwala
UNITOV Metricola: 0316836
UOS Registration Number: 210223257
The P-DBM Beyond 1AU:
Forecasting CME arrival in the whole heliosphere

Supervisors:

Prof. Dario Del Moro Università degli Studi di Roma “Tor Vergata”, Italy	Prof. Robertus Erdelyi University of Sheffield, UK

Advisors:
Prof. Michael Ruderman
University of Sheffield, UK

PhD Viva: University of Sheffield

Date: 15th April 2025
Examination Committee:

Prof. Dipankar Banerjee
Indian Institute of Space Science and Technology, India

Prof. Francesco Berrilli
Università degli Studi di Roma "Tor Vergata", Italy

Dr. Yi Li (chair)
University of Sheffield, UK

PhD Viva: Università degli Studi di Roma "Tor Vergata"

Date: 10th June 2025
Examination Committee:

Prof. Carmela Lardo
Università di Bologna

Prof. Nicola Bartolo
Università di Padova

Prof. Ivano Bertini
Università di Napoli "Parthenope"

Prof. Luca Pagano (Deputy)
Università di Ferrara

Acknowledgement

A Journey Through Turbulent Solar Storms and Calm Winds

My journey in the domain of space weather started during postgraduation. Courses on astrophysical fluid dynamics and space weather planted a little seed of curiosity for space weather in me, which has been nourished by my faculty advisor and M.Sc. thesis supervisor, Dr. Bhargav Vaidya. His constant guidance and mentorship acted as the magnetic field that shaped my path. It has been almost three years since I started my journey as a Ph.D. scholar, and there are many people whose encouragement and inspiration played a role as a guiding star that helped me to accomplish this journey. I am thankful to Dr. Bhargav Vaidya, who first pointed me towards this Ph.D. journey, and equal thanks goes to my classmate and dearest friend Dr. Koyena Das for being my ever-present solar wind and pushing me forward to make sure that I apply on time.

Now that I look back, the three best years of my life feel like a CME racing through the heliosphere- passed in the blink of an eye. I met numerous people during this Ph.D. journey, and many of them ended up becoming my lifelong specials in my personal as well as professional lives. In this final storm of thesis writing, extreme stress is getting converted to comfort through cherishing every moment spent with the remarkable people.

This journey truly began with an email from Dr. Dario Del Moro, congratulating me on securing the position—the best email and happiest moment of my life. It felt like the shock front of a CME hitting Earth's magnetosphere (intense, unexpected and life changing). On 17^{th} November 2021, I moved to Italy and met my supervisors, Prof. Dario Del Moro and Prof. Robertus Erdelyi (online). The warmth of their welcome was like the first rays of sunlight after a long polar night. Dario, I cannot thank you enough for providing me everything in this journey: freedom to explore more science, a wonderful learning experience, smooth sailing in all the bureaucratic storms, and many more. Beyond the academic realm, you and Valeria made sure that I was never alone in foreign land and had a family during Christmas Eve. You and Valeria both were my real Santa during this entire journey. The best gift of my life I have received from you, which is an observation run at Tiede Observatory (Tenerife). I can't put everything in words to describe your importance in this amazing journey.

Having two supervisors is basically more opportunity to learn new things. While Dario gave me the freedom, Roburtus pushed me to make the exploration worthy for my career. Robertus, your constant fuelling to make contributions in science during this PhD journey resulted in one peer-reviewed article, two datasets, and one GUI for the space weather research community. I am also thankful to you for believing in me and providing me an opportunity to learn how to keep the observatory habitably functional. I hope the nickname "Shiva" provided by you for destroying things at Gyula Bay Zolatan Observatory (Hungary) is erased after actually fixing stuff with Mariana, Balaz, and Szabolcs!

To my Roman brother Simone Chierichini, French family Gregoire Francisco and Irene Carranza, this journey could not be the same without you all. Being a different solar eruption phenomena, but the same manifestation of this PhD programme, you guys kept me going in research and social life with minimum drag. Simone and Greg, our discussion of scientific crimes over cedarata and beers kept my magnetic field stress low. Simone, you still have to help me to improve my culinary art for Italian pasta recipes. Gregoire and Ire, thank you for providing me a safe mode during high solar activity and making all the science meetings bearable. This Ph.D. journey cannot be completed without SWATNet solar system – Augustin André-Hoffmann, Slava Bourgeois, Guilherme Nogueira, Andreas Wagner, Shreeyesh Biswal, Mayank Kumar, Lidiya Annie John and Shifana Koya.

Dr. Tanja Amerstorfer, thank you for hosting me at the Austrian Space Weather Office (ASWO) and providing me valuable insight on HI images of CMEs and ELEvoHI model. My one month stay in Graz is really productive and fruitful just because of you and the entire ASWO team. Additionally, I want to thank Dr. Nandita Srivastava for the fruitful discussion about the ICME lineup work. The list of my academic mentors is always incomplete without Dr. Rajnikant Makwana, Dr. Ratan Kumar Singh and Dr. Ashwini Mahadik. At this point, I would like to sincerely thank my teachers and mentors — Hitesh Sir, Amisha teacher, and Chandrika teacher — whose guidance, support, and belief in me have deeply shaped who I am today. And it would be a crime to forget (Kamal S.) Rane Sir, whose exceptional teaching methods and life-changing advice have been a foundational force in my journey

— allowing me to proudly call myself a physicist.

To my safe mode provider, Matteo Cantoresi, Raffaele Reda, Chandana Hrishikesh, Archana Giri Nair, Fallon Konow and Letizia Casara, having amazing labmates like you during this period of minima and maxima is pure bliss. Matteo, you will be remembered forever for kicking me out of corridor D1 on the very first day of mine and the very passionate recipe of Arrosticini. Chandana and Archana, thank you so much for constantly pushing my health into the field of view of mine, feeding me deliciously healthy meals when I was too immersed in debugging my CME propagation model. Also, I would like to express my gratitude for disrupting the twisted loop of frustration caused by the immigration storm and enabling me to release some frictional energy time to time. Lastly, Letizia joined the solar and space physics group during the end of my cycle; she brought much-needed liveliness and fun during the silent phase of inactive solar physicists, planning various pranks and social outings Also, collective thanks go to Viviana Cuozzo, Claudio Mastromarino, Federico De Luca, Simone Mestici, Michele Berretti, Lorenza Lucaferri and Guglielmo Frittoli – you made sure I never felt like an outsider and fully immersed me in Italian culture and slang.

To my amazing friends in Italy, Parth, Aryan, Samiksha, Ravi, Arti, Neel, Anuj, Vikesh, Dinesh, Kishan, Aman, Hasti and Ankush. Parth, your concept "Gujju House" and people in it ensured that I have a place to get some infectious laughter and joy after a bad day. Every function, special dinner and outing became an unexpected ron-effective storms of happiness recorded permanently in my life cycle. Thanks to Samarth Ghoslya, for keeping a perfect blend of intellectual discussions and absolute nonsense, which I desperately needed. During the phase of minima, I met two remarkable phenomena Gautam Malik–elderly younger brother and Yoshita Sarin–sister from another mother; thank you so much for pulling me through the extreme magnetic field stresses when I was losing hope. I also want to say sorry to all of you for being a bizarre friend to walk with. I should not have made situations where I had to drag you; this deep felt sorrow is coming from my humanly heart. This transformation is the result of the debugging and system upgrade process led by Nancy Singh. I am thankful to you for playing role of magnetic reconnection in my life, breaking apart old patterns and reconnecting me with a completely new spectrum towards life observations. The new parameters added by you lately in my life simulation will always be appreciated.

In this journey through the heliosphere, my family – mom, dad, brother and sister – have been my inner magnetic field, always propelling me forward. My parents - Mrs. Jyoti and Mr. Himanshu, you are my solar core, the constant source of energy and strength that has fuelled every step on this path. To my brother, Mohit, you have been my interplanetary shockwave – always sweeping out the environment to reduce a drag. To my sister, Urvi Mistry, you have been my umbra and penumbra – offering both the comforting shadows when I needed rest (through comforting late-night calls) and bright light to inspire me when I needed to move ahead. Together you all have been my calming magnetic field, shielding me during life's most turbulent storms. Your presence reminded me that no matter how far I ventured, I would always be tethered to the home system that shaped me. As I continue to navigate through a minima and maxima, I will carry your presence like a guiding magnetic field, ensuring I stay on course.

- *Ronish*

Executive Summary

Space weather refers to the dynamic conditions within the magnetosphere, ionosphere, and heliosphere. One of the primary causes of space weather perturbation is the large-scale, magnetized plasma structures erupting from the Sun, known as Coronal Mass Ejections (CMEs). These CMEs propagate radially through the heliosphere, often produce interplanetary shocks, accelerate high-energy particles, and induce magnetic perturbations in planetary environments and spacecraft.

CMEs' intense magnetic field leads to significant disruption to the technosphere of human society that includes radio blackouts, power grid failures, satellite malfunctions, and also creates radiation hazards to astronauts and high-altitude aviation passengers. Precise forecasting of the arrival times of CMEs is thus necessary to counter their negative impacts through preventive measures. This study focuses on semi-empirical CME propagation models to make accurate CME arrival time predictions for operational space weather forecasting.

This thesis aims to extend the capabilities of Probabilistic Drag Based Model (P-DBM) through data-driven approach. One of the fundamental challenges in implementing DBM or its derivatives, such as DBEM and P-DBM, is the selection of appropriate values for the solar wind speed (w) and drag efficiency (γ). In this work, PDFs for those parameters are inferred from a catalogue of geo-effective CME-ICME pairs obtained through the mathematical inversion of the Drag Based Model (DBM).

Additionally, a two-dimensional version of P-DBM has been developed by incorporating a cone geometry representation for CMEs. Then P-DBM calculations have been refined to account for "Self-Similar-Expansion" and "Flattening-Cone-Evolution", and these advancements are made available through a simple graphical user interface.

Furthermore, a comprehensive list of ICME lineup events has been compiled for addressing the limitations of DBM, particularly its assumption of constant w and γ, by employing data-driven method. Additionally, variations in w and γ are also examined as a function of heliocentric distance. Correlations between CME and ICME properties with DBM parameters are also examined to increase modelling precision.

Keywords: Coronal Mass Ejection (CME), Probabilistic Drag Based Model (P-DBM), CME Arrival Prediction, Space Weather, Geo-effective Interplanetary Coronal Mass Ejection (ICME),

Outcome from this Thesis Research

Peer-reviewed publication:

1. ‘A catalogue of observed geo-effective CME/ICME characteristics’
   Ronish Mugatwala, Simone Chierichini, Gregoire Francisco, Gianluca Napoletano, Raffaello Foldes, Luca Giovannelli, Giancarlo De Gasperis, Enrico Camporeale, Robertus Erdélyi and Dario Del Moro,
   J. Space Weather Space Clim., 14 (2024) 6,
   DOI: https://doi.org/10.1051/swsc/2024004

2. ‘A Bayesian approach to the drag-based modelling of ICMEs’
   Simone Chierichini, Gregoire Francisco, **Ronish Mugatwala**, Raffaello Foldes, Enrico Camporeale, Giancarlo De Gasperis, Luca Giovannelli, Gianluca Napoletano, Dario Del Moro and Robertus Erdelyi
   J. Space Weather Space Clim., 14 (2024) 1
   DOI: https://doi.org/10.1051/swsc/2023032

Datasets and GUI:

- Mugatwala, R., Chierichini, S., Francisco, G., Napoletano, G., Foldes, R., Giovannelli, L., De Gasperis, G., Camporeale, E., Erdélyi, R., Del Moro, D. 2023, Wolpes11/PDBM-project-for-ICMEs (v3.1), Zenodo, doi:https://doi.org/10.5281/zenodo.8063404

- **Mugatwala, R.**, Chierichini, S., Francisco, G., von Fay-Siebenbürgen, R., Del Moro, D. 2024, A Catalog of CME–ICME Lineup Events, figshare, Dataset, doi:https://doi.org/10.6084/m9.figshare.25869190.v1

- P-DBM GUI : https://github.com/astronish16/P-DBM-GUI

Contents

List of Acronyms

ASWO	Austrian Space Weather Office
AI	Artificial Intelligence
AIA	Atmospheric Imaging Assembly
ADEOS	Advanced Earth Observing Satellite
ACE	Advance Composition Explorer
AU	astronomical unit
CME	Coronal Mass Ejection
CCMC	Community Coordinated Modeling Center
CDAW	Coordinated Data Analysis Workshop
CIR	Co-rotating Interaction Region
CSI	Critical Success Index
DBM	Drag Based Model
DONKI	Database Of Notifications, Knowledge, Information
DBEM	Drag Based Ensemble Model
ELEvoHI	Ellipse Evolution with Heliospheric Imager
ELEvo	Ellipse Evolution
ESA	European Space Agency
EUVI	Extreme Ultara Violet Imager
EUI	Extreme Ultaviolet Imager
EIT	Extreme ultraviolet Imaging Telescope
EUHFORIA	EUropean Heliospheric FORecasting Information Asset
ECA	Empirical CME Arrival
EAM	Effective Acceleration Model
SWASTi	Space Weather Adaptive SimulaTion
FOV	Field-of-View
GOES	Geostationary Operational Environmental Satellites
GCS	Graduated Cylindrical Shell
GUI	Graphical User Interface

HI	Heliospheric Imager
HELCATS	Heliospheric Cataloguing, Analysis and Techniques Service
HSS	High Speed Stream
HD	Hydrodynamics
ICME	Interplanetary Coronal Mass Ejection
ISRO	Indian Space Research Organization
ISWI	International Space Weather Initiative
ISWAT	International Space Weather Action Teams
LASCO	Large Angle and Spectrometric Coronagraph
MESSENGER	MErcury Surface, Space ENvironment, GEochemistry and Ranging
MHD	magneto-hydrodynamic
ML	Machine Learning
MAVEN	Mars Atmosphere and Volatile EvolutioN
MSL	Mars Science Laboratory
MAG	Magnetometer
ME	Magentic Ejecta
MAE	Mean Absolute Error
NASA	National Aeronautics and Space Administration
NOAA	National Oceanic and Atmospheric Administration
OSO	Orbiting Solar Observatory
P-DBM	Probabilistic Drag Based Model
PSP	Parker Solar Probe
PDF	Probability Distribution Function
PP	proton-proton
PIL	Polarity Inversion Line
POS	Plane-of-Sky
POD	probability of Detection
RSS	Residual Sum of Square
STEREO	Solar Terrestrial Relations Observatory
SECCHI	Sun Earth Connection Coronal and Heliospheric

	Investigation
SolO	Solar Orbiter
SOHO	SOlar and Heliospheric Observatory
SDO	Solar Dynamic Observatory
SEP	Solar Energetic Particle
SWPC	Space Weather Prediction Center
SEEDS	Solar Eruptive Event Detection System
STP	Solar Terrestrial Program
SCIP	Sun Centered Image Package
SUIT	Solar Ultaviolet Imaging Telescope
SSS	Solar Surface Source
SMM	Solar Maximum Mission
SOA	Speed of Arrival
SWEA	Solar Wind Electron Analyzer
SWIA	Solar Wind Ion Analyzer
SW	Solar Wind
SIR	Stream Interaction Region
SR	Success Ratio
TOA	Time of Arrival
vTEC	Vertical Total Electron Content
VELC	Visible Emission Line Coronagraph
VEX	Venus Express
WSA	Wang-Sheeley-Arge
WISPR	Wide-field Image for Solar PRobe Plus

List of Figures

List of Tables

Chapter 1

Introduction

This chapter gives a brief introduction to space weather, overall properties of the Sun, solar activity, and solar eruption phenomena such as CMEs, solar flares, SEPs. This chapter begins with a few significant geomagnetic storm events and their reported consequences to establish a base for the impact of space weather on modern human infrastructure and activities. Following this, a basic overview of the solar properties is provided along with the solar anatomy. Subsequently, the chapter provides a brief overview of solar activity and its historical observations. It also covers a concise explanation of key space weather events, including Solar Flares, CMEs, and SEPs. The chapter concludes by outlining the structure and organisation of the remaining chapters of the thesis.

1.1 What is space weather?

On 3rd February 2022, SpaceX launched 49 satellites for the Starlink constellation as part of its mission to expand internet coverage via satellites. However, shortly after the deployment, 38 satellites unexpectedly de-orbited and were lost as they re-entered Earth's atmosphere and burned up. The total economic loss from this event has been reasonably estimated at upward of $50 million [Sheetz, 2022]. This failure was attributed to enhanced neutral density resulting from a geomagnetic storm [Baruah et al., 2024, Fang et al., 2022, Hapgood et al., 2022]. Going back in time, during the 3rd and 4th November 2015, a powerful magnetic storm caused a radio blackout in Sweden, and flights disappeared from the air traffic control screens for more than an hour [Abd-Elghany, 2019]. On 17th March 2015, the notable increase in Vertical Total Electron Content (vTEC) is observed over the American region, while the largest decrease was recorded over the Asian region due to the largest geomagnetic storm of solar cycle 24 named as *"St Patrick's Day Storm"* [Nava et al., 2016]. In November 2003, a major geomagnetic storm referred to as the *"Halloween Storm"*, caused significant disruptions, including a one-hour-long power outage in Sweden, transformer damage in South Africa, momentary failure of the SOHO satellite, and damage to both the ACE and Japanese Advanced Earth Observing Satellite (ADEOS)-2 satellites. Additionally, auroras were observed at lower latitudes, including Texas and Mediterranean countries of Europe [Bergeot et al., 2011, Lopez et al., 2004]. One more major geomagnetic storm, known as *"Bastille day Storm"*, occurred on 14th July 2000 and caused similar effects [Watari et al., 2001, Andrews, 2001, Reiner et al., 2001]. An additional noteworthy event is the geomagnetic storm of March 1989, which caused an outage of Hydro-Québec's electricity transmission system, communication interruption to the GOES weather satellite and a few other impacts [Shirochkov et al., 2015, Boteler, 2019]. This event became widely known as the *"Great Quebec blackout"*, with many newspapers referring to it as "The day Sun brings the darkness". The 1972 Vietnam War also has a mysterious link with geomagnetic storms [Knipp et al., 2018]. On 4th August 1972, U.S. marine pilots observed the explosion of about twenty-four sea mines in the coastal waters of Northen Vietnam without any explanation. Between the 13th and 15th May 1921, the most intense geomagnetic storm of 20th century interrupted electrical service and sparked many fires worldwide, including the "Grand Central Terminal" that led to it being named the *"New York Railroad Storm"*. These types of events have been observed for many centuries, not just in recent times. A particularly noteworthy magnetic storm was recorded on 1 September 1859. Richard Carrington, an amateur British astronomer, was sketching a cluster of dark spots by projecting the Sun through his brass telescope in his private observatory. Suddenly, an extremely bright light patch over the sunspot caught his attention. Within a minute, this bright white light patch vanished, but during that same night, the effects of this event were felt across the globe. Colorful auroras illuminated the skies from the poles to low-latitude regions near the equator so brightly that people believed the Sun had risen early. On the next day, telegraph communication around the world failed, with many operators reporting sparks and electric shocks from their telegraph machines [Carrington, 1859, Hodson, 1859]. Also, many telegraph operators discovered that they could still transmit a message without batteries just by using the auroral current. These phenomena were the result of a powerful geomagnetic storm triggered by one of the largest solar flares ever recorded [Cliver, 2006]. Since Carrington had witnessed the root cause of these extraordinary events with his naked eyes, this incident became known as the *"Carrington Event"* [Hudson, 2021].

During the aforementioned incidents, the most extreme form of space weather was occurring. These events[1] serve as a good illustration of how the modern hi-tech society is vulnerable to space weather effects. A summary of the severe space weather effects on our technology-driven society is shown in Figure 1.1. Considering the severe effects of space weather events on technology-dependent human society, space weather is now regarded as a major societal risk alongside other natural hazards like earthquakes, tsunamis, volcanic activity, floods, etc. Therefore, detailed studies of the impact of a severe space weather event on modern society have been conducted by a few federal agencies and science institutions, such as the US National Research Council (NRC 2008), the Lloyds of London (2010), the UK Royal Academy of Engineering (2013) etc. The NRC report provided an estimate for economic loss due to this kind of storm of "$1 trillion to $2 trillion during the first year alone ... with recovery times of 4–10 years". While Lloyds' report says that "Sustained loss of power could mean that society reverts to 19th century practices. Severe space weather events that could cause such a major impact may be rare, but they are nonetheless a risk and cannot be completely discounted." [Cliver et al., 2022]. *"Space Weather"* is a collective term that refers to the environmental conditions on Earth and other planets that result from activity originating outside the planetary environment. Actually, this is not the only definition; the term "Space weather" has a very wide dynamic definition, but a formal definition was introduced in *"Understanding space weather to shield society: A global road map for 2015–2025 commissioned by COSPAR and ILWS"* Schrijver et al. [2015].

Space Weather: US National Space Weather

Conditions on the Sun and in the Solar Wind, magnetosphere, ionosphere and thermosphere that can influence the performance and reliability of space-born and ground-based technological system and can endanger human life or health.

---

[1] List of solar storms: `https://en.wikipedia.org/wiki/List_of_solar_storms`

Space Weather: A COSPAR definition

Space weather refers to the variable state of the coupled space environment related to changing conditions on the Sun and in the terrestrial atmosphere, specifically those conditions that can influence the performance and reliability of space-borne and ground-based technological systems and that can directly or indirectly endanger human well-being.

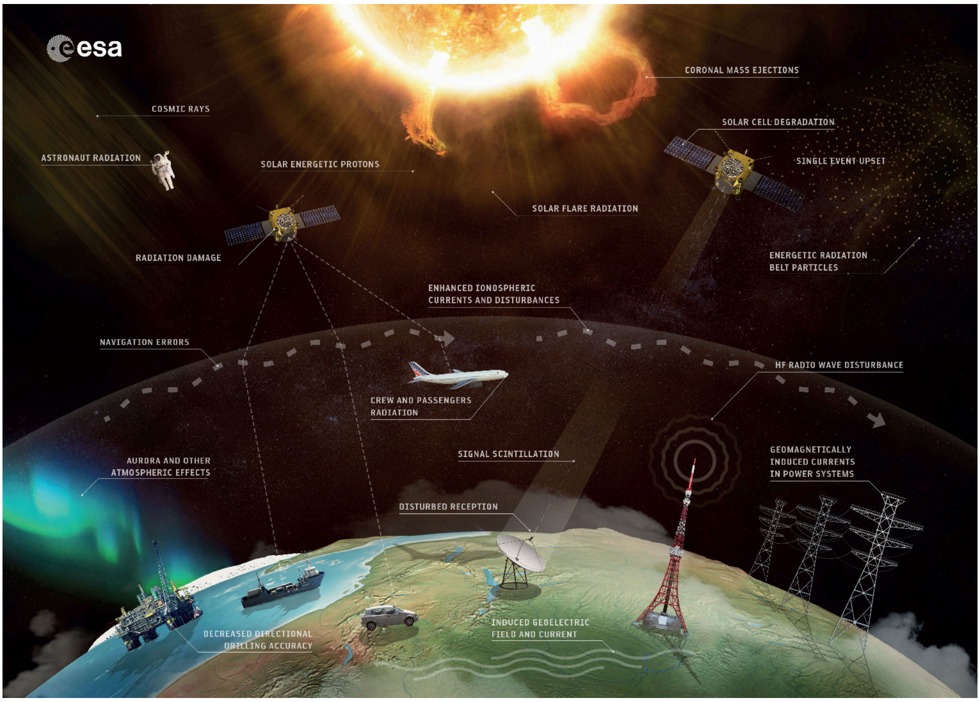

Figure 1.1: A conceptual illustration of the space weather effects on the modern human society. (Courtesy: ESA)

1.2 Primary cause of space weather: The Sun

Around 4.6 billion years ago, the remarkable yet typical star of our solar system was born. Since then, the Sun has been a source of life on Earth by maintaining Earth's atmosphere, influencing the planet's climate via light and heat, and playing a crucial role in human civilisation

1.2.1 Properties

The Sun falls on the main sequence of the Hertzsprung-Russell diagram, a region primarily occupied by typical stars. It came into existence as a result of the gravitational collapse of a molecular gas cloud. Currently, the Sun is in a state of hydrostatic equilibrium ($\nabla P = -\rho g$); however, this equilibrium is continuously influenced by various large-scale and small-scale dynamic processes such as convective flows, solar dynamo, etc. It is predicted that the Sun will enter into a red giant phase in another $\sim$ 5 billion years before ending its life as a white dwarf [Phillips, 1995, Byrne, 2010].

- **Mass** - The total mass of the Sun is $M_\odot = (1.9891 \pm 0.0012) \times 10^{30}$ kg. That is about 3,30,000 times the mass of Earth and more than 99% of the mass of the solar system. The average density of the Sun is 1.41 $\times$ 10^3 kgm^{-3} [Bhatnagar and Livingston, 2005, Moldwin, 2008].

- **Radius** - The radius of the Sun is $R_\odot = (6.9626 \pm 0.0007) \times 10^5$ km. The average Sun-Earth distance is 1.496 $\times$ 10^8 km, which is 215 times the solar radii $R_\odot$, called 1 astronomical unit (AU)

- **Luminosity** - The luminosity of the Sun is $L_\odot = (3.845 \pm 0.006) \times 10^{26}$ W and magnitude is 4.8 [Gombosi, 1998].

- **Composition** - The most common element in the Sun is hydrogen (92.1%) followed by helium (7.8%). The heavy elements such as oxygen, carbon, nitrogen and iron are collectively (0.1%) of the solar mass Moldwin [2008].

1.2.2 Solar Structure

The solar surface and atmosphere can be observed directly via imaging, spectroscopy, etc. [Minnaert, 1965, Nelson et al., 2006]. While it's difficult to make direct observations of the solar interior, scientists have developed a few indirect methods, such as helioseismology and solar neutrino observations, to infer the structure and processes of the Sun [Bahcall, 1978, Demarque and Guenther, 1999]. The Sun has a layered structure and can be divided into the interior and atmosphere, separated by the photosphere, the bright surface that we see. The solar interior is made of the core at the centre of the Sun and two more layers between the core and photosphere: the radiative zone and the convective zone. The solar atmosphere consists of the photosphere, chromosphere, transition region and the corona.

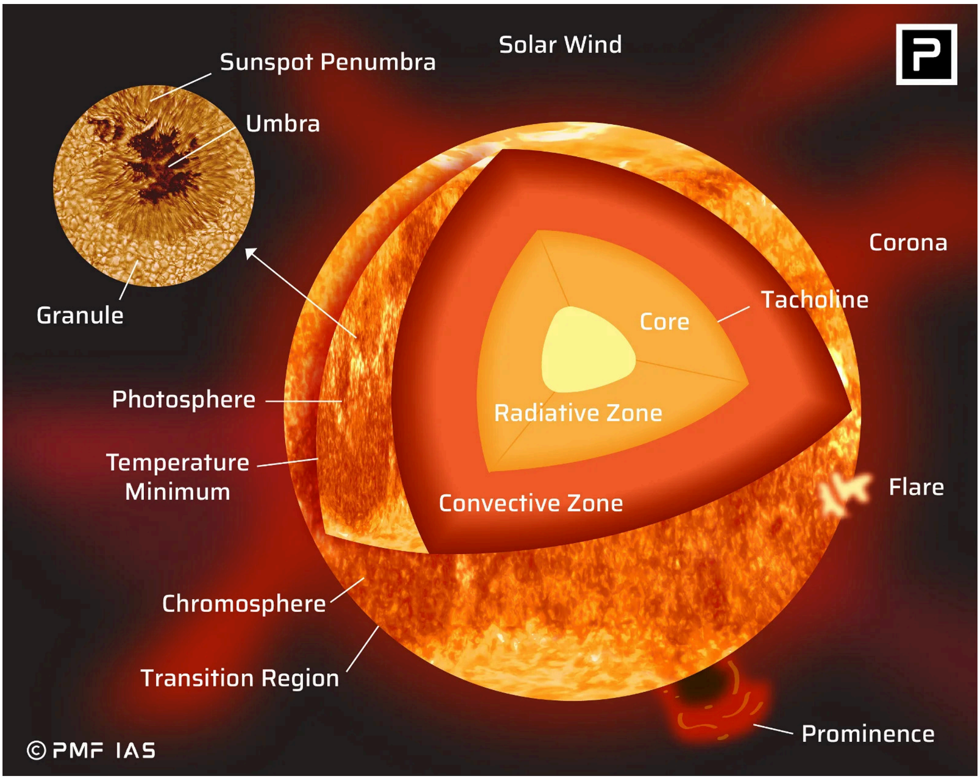

Figure 1.2: The layered structure of the Sun. (Courtesy: PMF-IAS)

1. **Solar Interior**

   The core—the central region of the Sun—holds half of the solar mass, with about one-fifth of the solar volume being the primary source of solar energy. The high temperature (1.5×10^7 K) and high pressure (2.3×10^{11} times the Earth's atmospheric pressure) conditions are enough for the thermonuclear fusion reaction. This reaction converts the hydrogen into helium via proton-proton (PP) chain and releases the energy in the form of photons. This part of the Sun also gave birth to a very well-known *solar neutrino problem* [Kirsten, 1995]. The energy generated in the core propagates continuously outwards to the radiative zone by gamma-ray diffusion. In this zone, photons from the core are scattered, absorbed, and re-emitted many times. The re-emitted photons have lower energy and a higher wavelength. The photons take more than 170000 years to reach the outer edge of the radiative zone. The uppermost 30% of the solar interior is called the convection zone. The convective zone transports the energy to the photosphere by convection. In this zone, the solar material is unstable due to the high radial temperature gradient. The core and the radiative zone rotate as a solid body, whereas the convection zone exhibits differential rotation. Due to this transition, there exists a strong shear layer between the radiative and convective zones known as tachocline [Spiegel and Zahn, 1992]. This shear layer is thought to be the source of the large-scale solar magnetic field powering the solar dynamo, which is the ultimate driver of space weather phenomena on the Sun.

2. **Solar Atmosphere**
   The part of the Sun from which photons can escape directly into space is defined as the solar atmosphere. The photosphere is the lowest and extremely thin layer (100–400 km thick) of relatively dense plasma with a temperature of $\sim$ 6000 K. The photosphere emits most of the solar radiation [Priest, 2014]. Above the photosphere lies a more rarefied and, hence, transparent layer of plasma, which is known as the chromosphere. The density of the plasma and hence the number of emitted photons decrease drastically with height [Moldwin, 2008]. Therefore, the chromosphere is not visible against the bright photosphere, but it can be seen for a few seconds at the start and end of a solar eclipse as the red colour of the Balmer spectrum [Priest, 2014]. The element He was discovered in the chromosphere before it was discovered on Earth. The chromosphere is also home to many solar phenomena such as spicules (hot jets of gas), supergranulation cells, filaments plages, and prominences [Beckers, 1972, Moldwin, 2008, Rincon and Rieutord, 2018]. The temperature decreases gradually from the photosphere to the base of the chromosphere, then slowly increases in the chromosphere. Above the chromosphere, there exists a thin transition region where temperature rises sharply from $\sim 2 \times 10^4$ K to $\sim 10^6$ K [Sachdeva, 2018]. The next layer is known as the solar corona, which is the outermost part of the solar atmosphere, that becomes visible when the bright photoshperic light is covered—as e.g. during an eclipse. The reason behind the drastic jump in temperature from the chromosphere to the base of the corona is unknown and giving

rise to an unsolved mystery known as '*coronal heating problem*'.

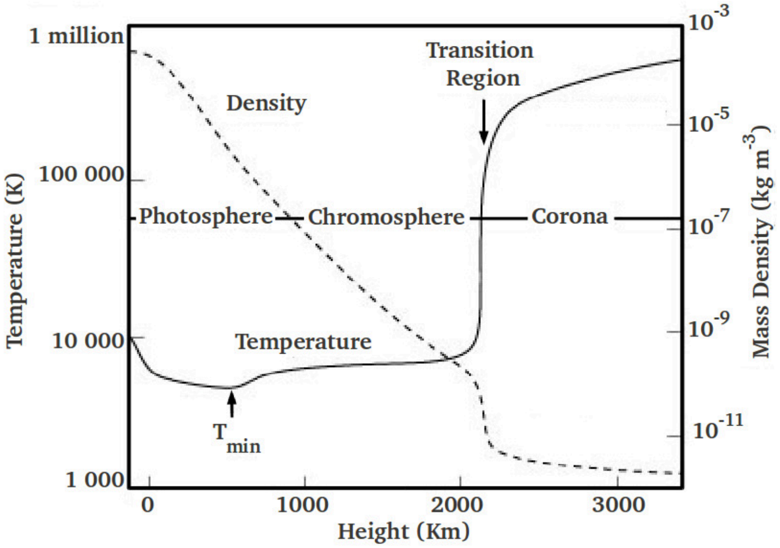

Figure 1.3: The thermal and mass density characteristics of the solar atmosphere. (Courtesy: de Patoul [2012]

1.2.3 Solar Activity and Sunspots

Powerful eruptions from the Sun are the source of intense space weather, which significantly affects solar system planets and the interplanetary space extending to the far reaches of the heliosphere. Ancient civilizations recorded the movement of the Sun by observing it with the naked eye and using it to develop the calendar system. In 1610, Galileo pointed his telescope to the Sun and discovered sunspots by focusing the image onto a piece of paper. The sunspot drawing by Galileo for the 6th July 1613 is shown in Figure 1.4. Somewhere near 1749—almost 150 years later—the first regular daily observation of sunspots began at the Zurich Observatory in Switzerland. The Swiss astronomer Samuel Heinrich Schwabe precisely recorded the position of every sunspot for 18 years, and with this dataset, he discovered the occurrence of the 11-year solar cycle in 1844. The time interval from the sunspot minimum to the next sunspot minimum is called the solar cycle, and the period from 1755 to 1766 has been chosen as Solar Cycle 1.

The present solar cycle 25 began in November 2019, which is supported

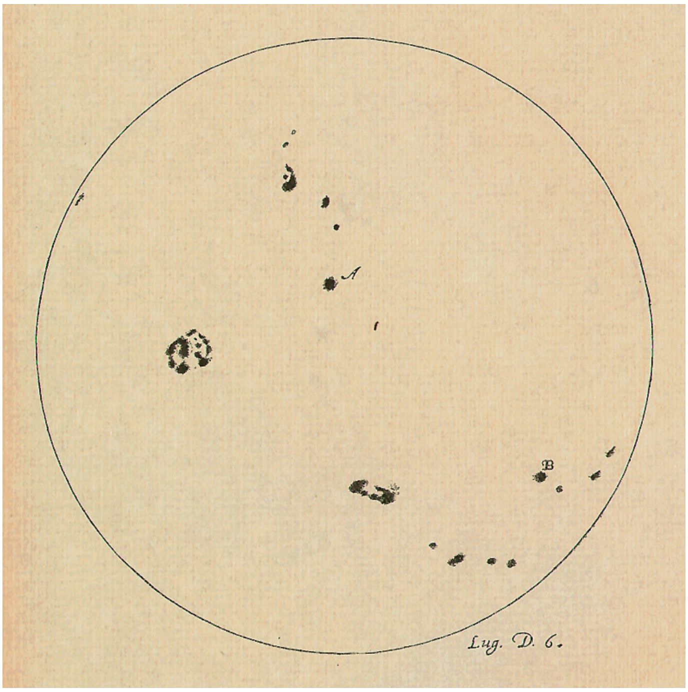

Figure 1.4: Sunspot drawing by Galileo for the 6th July 1613. (Courtesy: The Galileo Project)

by the appearance of two reversed polarity sunspots. The Space Weather Prediction Center (SWPC) of NOAA has predicted that the Solar Cycle 25 is expected to reach its maximum in July 2025, with a peak occurring between November 2024 and March 2026. Sunspots begin as small dark pores that gradually enlarge over the course of a day, eventually developing into full-fledged sunspots. These spots are associated with intense magnetic fields that rise from the convection zone to the photosphere. A sunspot consists of two main parts: a central darkest part called the "Umbra", where the magnetic field is approximately normal to the solar surface. Around the dark spot, there is an area of a more inclined magnetic field known as "Penumbra". In 1908, American astronomer George Ellery Hale discovered the existence of a magnetic field in sunspots [Hale, 1908, Koskinen, 2011]. Nowadays, we can measure the significantly weaker magnetic field on the Sun; sunspots still play a crucial role in studies of solar magnetism. Usually, the sunspots appear in pairs having opposite polarities, divided by a neutral line called the Polarity Inversion Line (PIL). The magnetic polarity of the leading spot is the same as the polarity of a hemisphere, while the trailing spot has the opposite polarity. This is known as “Hale’s law” [Hale and Nicholson, 1925, Koskinen, 2011, Maharana et al., 2024-08-28]. If the leading sunspot is in the northern hemisphere, then it exhibits positive polarity, and the leading spot shows negative polarity. This magnetic orientation of the bipolar group remains unchanged in each hemisphere over the whole 11-year cycle. Then in the next cycle, the magnetic orientation of the sunspot group reverses. It takes two sunspot cycles to return to the state of original magnetic orientation; this magnetic cycle of the Sun is 22 years and is known as the “Hale cycle”, Whereas the 11-year cycle is known as the “Schwabe cycle” [Schwabe and Schwabe Herrn, 1844, Koskinen, 2011]. It was observed that the sunspot numbers closely correlate with solar activity. In 1848, the Swiss astronomer Rudolf Wolf introduced the relative sunspot number R, which is also known as the sunspot index [Wolf, 1861, Wilson, 1998, Gombosi, 1998].

$$R = k(10g + f)$$

where k is a correction factor, g is the number of sunspot groups that are recognizable, and f is the number of individual sunspots. During a cycle of 11 years, Sunspots emerge at mid-latitudes (around 30–40°) on both sides of the solar equator. Over time, sunspots migrate to lower latitudes near the equator. The evolution of sunspots’ position over the solar cycle is seen in the popular “butterfly diagram”[Maunder, 1904]. Figure 1.5 shows the movement of the sunspots over the initial observations done by Samuel Heinrich Schwabe, while Figure 1.6 shows the butterfly diagram for the sunspot observations from 1820 to 2020.

In the mid 19th century, British military officer Col. Edward Sabine (in charge of British observatories around the world that monitored surface weather and changes in the geomagnetic field) and director of Zurich observatory Prof. Rudolf Wolf independently showed the correlation between sunspots and geomagnetic activity [Wolf, 1861]. The systematic observation of three natural phenomena: the aurora, Earth’s magnetic field and sunspots, sail the study of space weather. Then, just after that, a number of discoveries were made that helped to connect the dots between solar activity, sunspots and geomagnetic fields [Refer: Section 1.3.4 of Moldwin, 2008].

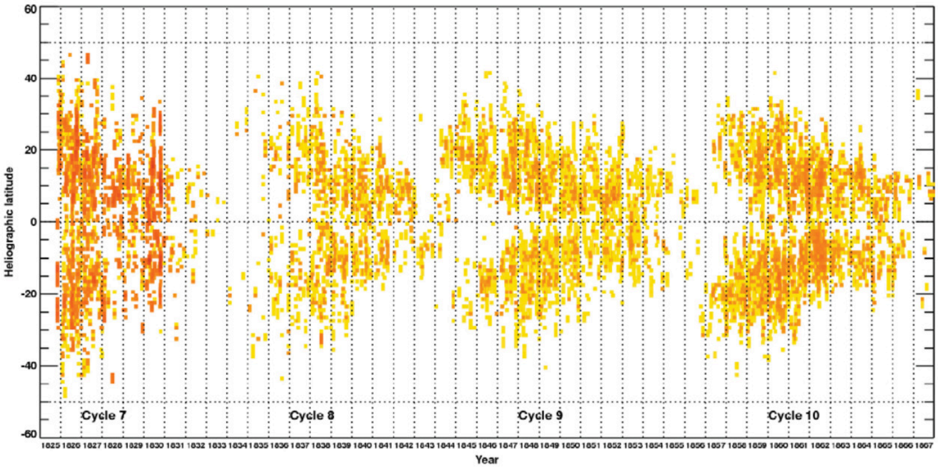

Figure 1.5: Butterfly diagram using observation of Heinrich Schwabe. The sunspot area is overestimated until solar cycle 8 due to the fact that Heinrich did not distinguish penumbra from umbra. Courtesy: Arlt and Abdolvand [2010]

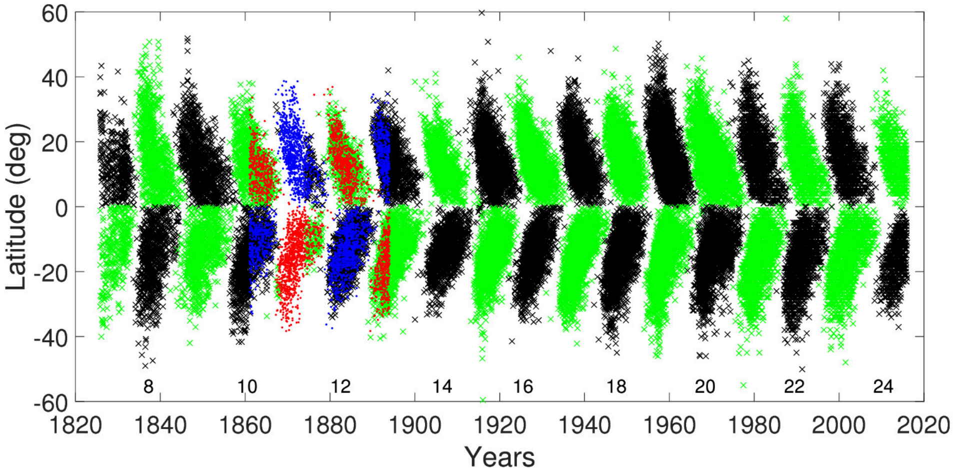

Figure 1.6: Butterfly diagram using three different sets of observation. Courtesy: Leussu et al. [2017]

1.2.4 Solar Wind: The ground state of heliosphere

The solar wind is a continuous outflow of plasma from the Sun and consists mostly of electrons and protons with energies of ∼ 1 keV [Byrne, 2010]. The existence of the continuous flow from the Sun was suggested by German astronomer Ludwig Biermann during the 1950s. He noticed that cometary tails always point away from the Sun even when the comet is moving away from the Sun [Biermann, 1951, Koskinen, 2011, Gombosi, 1998] Later, Alfvén emphasized that the flow must consist of magnetized plasma. The first direct in situ measurements of the solar wind were made by the Russian Lunik III and Venus I spacecraft in 1959. Definitive confirmation of the solar wind's continuous nature was provided by the U.S. Mariner II mission, conducted between 1962 and 1967 [Gombosi, 1998, Koskinen, 2011].

The corona has very little mass, and if spherical geometry is assumed, then a solution of hydrostatics corona is given as:

$$T = T_0 \left(\frac{r_0}{r}\right)^{2/7} \tag{1.1}$$

Where T denotes the temperature of the solar corona at an arbitrary distance r. which satisfy the boundary conditions that $T = T_0$ at $r = r_0$ and $T = 0$ at $r \to \infty$. When this solution is substituted in Euler's equation for hydrostatics. It gives us,

$$p = p_0 exp\left[\frac{7GM_\odot m}{5k_b T_0 r_0}\left\{\left(\frac{r_0}{r}\right)^{5/7} - 1\right\}\right]. \tag{1.2}$$

Where p denotes the pressure in solar corona as a function distance r, G is gravitational constant, $M_\odot$ is solar mass, m is coronal mass, k_b is Boltzman's constant, and p_0 is pressure at arbitrary distance r_0. This implies a non-zero asymptotic solution for pressure as r approaches infinity. From Equations 1.1 and 1.2, it becomes evident that as the temperature approaches zero with increasing distance, the pressure must increase. The asymptotic value of p is significantly higher than the typical pressure in the interstellar medium. Therefore, it is not feasible to derive a hydrostatic corona solution where both p and T hold physically meaningful values [See section 4.4 of Choudhuri, 1998].

In 1958, Eugene Parker[2] presented a detailed hydrodynamic model of the solar wind. He assumed steady spherical outflow in a radial direction with time-independent velocity. Under steady outflow conditions, mass conservation is given as:

$$\frac{\partial}{\partial r}(r^2 \rho v) = 0 \implies \frac{2}{r} + \frac{1}{\rho}\frac{\partial \rho}{\partial r} + \frac{1}{v}\frac{dv}{dr} = 0. \tag{1.3}$$

---

[2] With the discovery of solar wind, Dr. Eugene Parker built the foundation of modern solar and space weather physics. Fox [2022] is a wonderful article on the father of heliophysics.

Similarly, momentum conservation can be written as:

$$\rho v \frac{\partial v}{\partial r} = -\frac{\partial p}{\partial r} - \frac{GM_{\odot}\rho}{r^2}. \tag{1.4}$$

Under the isothermal conditions, the pressure of ideal gas is $p = R\rho T$ and if we define isothermal sound speed $v_c = \sqrt{RT}$. Then Equation 1.4 can be re-written as:

$$\left(v - \frac{v_c^2}{v}\right)\frac{\partial v}{\partial r} = \frac{2v_c^2}{r} - \frac{GM_{\odot}}{r^2}. \tag{1.5}$$

Integrating Equation 1.5 gives Parker's solar wind solution (see section 6.8 of Choudhuri [1998]).

$$\left(\frac{v}{v_c}\right)^2 - ln\left(\frac{v}{v_c}\right)^2 = 4ln\left(\frac{r}{r_c}\right) + 4\frac{r_c}{r} + C \tag{1.6}$$

where $r_c = \frac{GM_{\odot}}{2v_c^2}$ and C is a constant of integration. The different values of C give different mathematically admissible isothermal solutions. These solutions can be divided into five different types, as shown in Figure 1.7. Type I and II solutions are double valued and hence physically not admissible. Type III solution is supersonic everywhere while type IV solution is subsonic, which is known as 'solar breeze'. Type V solution is a standard solar wind solution. Inflow approximation for type V solution where the flow speed is low at infinity and high flow speed in the interior is known as "Bondi's solution".

The modern understanding suggests two primary types of solar wind [Feldman et al., 2005].

1. Fast Solar Wind: The fast solar wind originates from coronal holes and has a typical range of 500–800 km/s. The fast solar wind has low proton density and high proton temperature. It has a low abundance of highly ionised heavy ions, which indicates its source is the photosphere [Cranmer et al., 2017].

2. Slow Solar Wind: The slow solar wind is thought to emerge from a region of closed magnetic field lines near the solar equator and active regions. The slow solar wind is typically flowing at a speed below 500 km/s. It has high proton density and temperature compared to fast solar wind. The rich amount of highly ionised heavy ions indicates its source to be the solar corona.

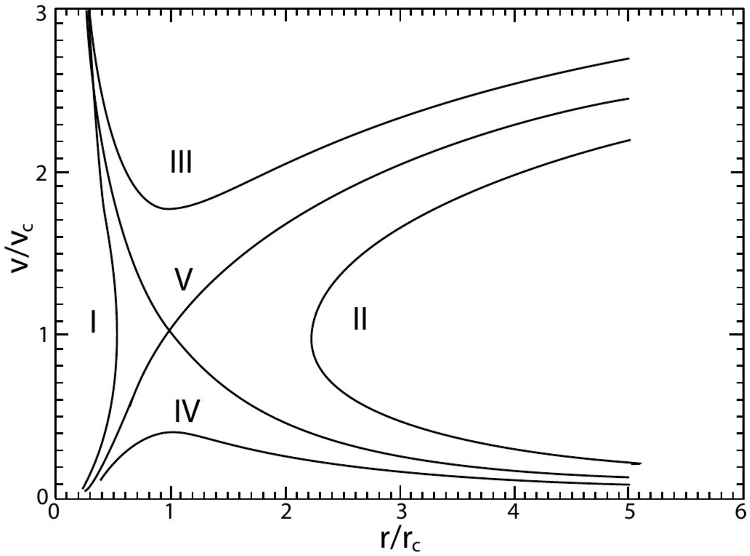

Figure 1.7: The five types of Parker's solar wind solution. Courtesy: Byrne [2010]

1.3 Space Weather Events

Transients in the solar wind are key drivers of space weather and are commonly referred to as space weather events. One such transient is the High Speed Stream (HSS), a fast solar wind that emerges from coronal holes and interacts with the ambient solar wind as it moves away from the Sun. This interaction generates compression zones with high plasma density, magnetic fields, and pressure–known as Stream Interaction Regions (SIRs). Over the course of solar rotation, the repetition of these SIRs leads to the formation of Co-rotating Interaction Regions (CIRs). Both SIRs and CIR are capable of inducing minor geomagnetic storms. Additionally, with the escalating reliance on space-based systems in modern society, our technosphere has become significantly susceptible to solar eruptive phenomena, such as solar flares, CMEs, and Solar Energetic Particles (SEPs). This thesis primarily examines CMEs, which are large discharges of plasma and magnetic fields from the solar corona, posing a considerable risk to technologies sensitive to space weather.

1.3.1 Solar Flares

A solar flare is a sudden, intense burst of energy and radiation from the Sun's surface and outer atmosphere, caused by the release of magnetic energy due to magnetic reconnection, which appears as a short-lived brightening. This energy is emitted in the form of electromagnetic radiation and energetic particles [Gombosi, 1998, Koskinen, 2011]. The total energy emitted during solar flare occurrence falls between $10^{21} - 10^{25}\ J$. Historically, flares were most effectively observed at the H-alpha wavelength, occurring in the chromosphere, while white light flares are occasionally detected in the photosphere. Presently, satellites are used to monitor solar flares at X-ray wavelengths. Figure 1.8 illustrates the solar flare observed by SDO/AIA in extreme ultraviolet light.

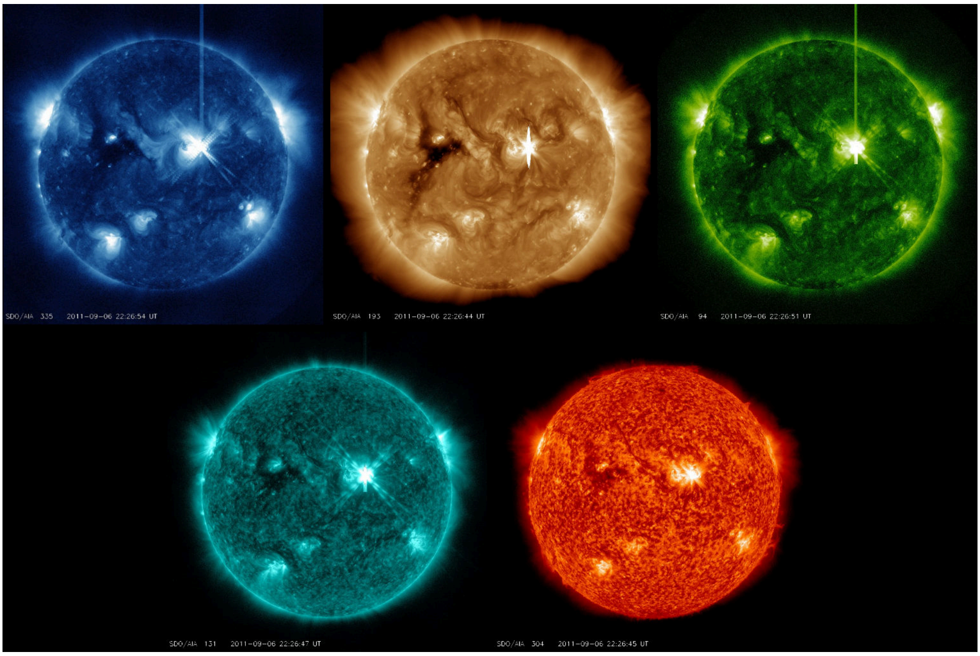

Figure 1.8: The X2.1 class flare took on 6th September 2011 is observed by SDO/AIA in various extreme ultraviolet wavelengths. Top panel: Blue - 335Å, Yellow - 193Å, Green - 94Å. Bottom panel: Cyan - 131Å, Orange - 304Å. Credit: SDO Team

Solar flares are observable across a broad spectrum of wavelengths, ranging from radio to gamma rays, and are classified according to their intensity and the duration of excess flux. Solar flares are classified as faint (F), normal (N) or brilliant (B) based on white-light observations [Gombosi, 1998]. While optical emission from flares typically increases by only a few percent, the X-ray emission can increase by several orders of magnitude. Therefore, the severity of a flare is classified via soft X-ray flux levels measured at Earth by Geostationary Operational Environmental Satellites (GOES) [Thomas and Teske, 1971, Fletcher et al., 2011]. According to their peak flux, flares are classified into five categories: A, B, C, M, and X, with each class being 10 times more intense than the previous one, and each class has nine subdivisions ranging from, e.g., X1 to X9, M1 to M9, etc. This numerical suffix denotes the strength of an event within a class, which means X2 flare is twice, and X3 flare is thrice in strength compared to X1. Table 1.1 summarises the GOES flare classification scheme based on the peak of soft X-ray measurements. In addition to the white-light and X-ray classifications, there exists an older classification scheme based on the H_α area [Thomas and Teske, 1971]. The X-ray and extreme ultraviolet radiation emitted by solar flares ionise the lower ionosphere, leading to the absorption or degradation of radio waves due to collisions with electrons. This process results in radio blackouts, which are categorised into five levels using the NOAA Space Weather Scale. These levels are directly related to the peak soft X-ray flux of the flare. Table 1.2 provides the classification of radio blackout caused by a solar flare and its relation to the solar flare class.

GOES class	Peak X-ray flux (W/m^2)	H_α class	H_α area (sq. degrees)
A	$< 10^{-7}$	S	< 2.0
B	$10^{-7} - 10^{-6}$	S	< 2.0
C	$10^{-6} - 10^{-5}$	1	2.0
M	$10^{-5} - 10^{-4}$	2	5.1
X	$> 10^{-4}$	3	12.4

Table 1.1: Classification Scheme of solar flares based on the peak value in GOES X-ray flux measurements and its relation with H_α classification scheme. Adapted from Fletcher et al. [2011].

Though solar flares involve the rapid release of electromagnetic energy, their observation across different wavelengths reveals distinct developmental phases. A typical flare evolves through three stages: the pre-flare phase, the impulsive phase, and the decay phase [Benz, 2008, Fletcher et al., 2011, Koskinen, 2011,

X-ray class	Radio blackout class	Severity indicator
M1	R1	Minor
M5	R2	Moderate
X1	R3	Strong
X10	R4	Severe
X20	R5	Extreme

Table 1.2: The relation between solar flare and radio blackout scale provided by NOAA Space Weather Scale.

Temmer, 2021]. The pre-flare phase is characterized by thermal emission in soft X-ray and extreme ultraviolet wavelengths. During the impulsive phase, most of the energy is released, accompanied by non-thermal emissions in hard X-ray. Once the maximum intensity of a solar flare is achieved, the decay phase begins, during which the flare's intensity levels gradually return to normal. The decay phase can last from 30 minutes to over an hour, depending on the flare's strength. Figure 1.9 illustrates the evolution of a solar flare among various wavelengths.

1.3.2 Coronal Mass Ejections

The classic definition of a Coronal Mass Ejection (CME) refers to the massive eruption of plasma and magnetic field from the Sun [Howard, 2011, Koskinen, 2011, Webb and Howard, 2012, Moldwin, 2008]. The mass carried out by a CME typically ranges from $10^{11} - 10^{12}$ kg [MacQueen et al., 1997], with an average value of 1.7×10^{12} kg derived from LASCO observations [Vourlidas et al., 2002]. CMEs generally exhibit angular sizes between 40-50°. The magnitude of kinetic energy carried out by CME is the order of $10^{24} - 10^{25} J$, comparable to that of a solar flare [Koskinen, 2011]. CMEs typically travel at speeds between 400 and 1000 km/s.

CMEs can erupt from a wide range of latitudes, but mostly they are confined to the lower latitude regions during the solar minima [Hundhausen, 1993]. The number of CME occurrences is correlated with the solar activity; one eruption a day during solar minima and 4-5 eruptions per day during solar maxima [Webb and Howard, 1994, Robbrecht et al., 2009, Gopalswamy et al.,

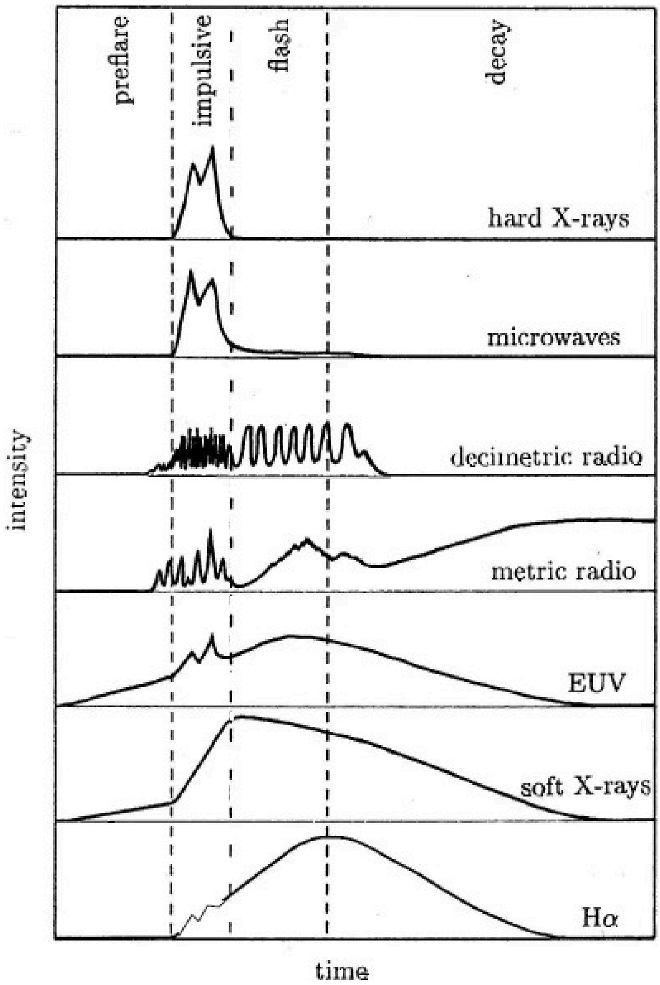

Figure 1.9: The flare intensity profile observed at several wavelengths. The various phases are indicated at the top. Adpated from Benz [2008]

2009, Webb and Howard, 2012, Howard, 2011]. The correlation between CME occurrence and sunspot number was first identified by Webb and Howard [1994]. A long-standing debate has persisted regarding whether CMEs are best described as "coronal-mass ejections" (emphasizing the ejection of mass from the corona) or "coronal mass-ejections" (highlighting the observation of mass in the corona). The composition of CME is uncertain up to a significant level, it can be answered by a complete understanding of CME launch mechanism and its interaction with the environment during propagation. Two primary possibilities regarding CME composition have been proposed:

1. Case-I: If CME initiates in the corona, it consists of coronal material such as heavy ions.

2. Case-II: If the CME initiation took place in the lower atmosphere, the CME composition is mostly hydrogen, helium or other lighter elements.

In fact, CME may contain material from various regions. However, most of the CME mass originates from the lower solar atmosphere, with the term "coronal" denoting the observation of this material in the solar corona [Fludra et al., 1999, House et al., 1981, Koskinen, 2011, Howard, 2011].

1.3.2.1 Morphology of CMEs

CMEs are large, optically thin structures that propagate away from the Sun, appearing as bright structures in white light due to Thomson scattering of free electrons. The CMEs are imaged in white light, using a special instrument called a coronagraph, creating an artificial solar eclipse by blocking the light from the solar disk. The coronagraphs from various spacecraft are discussed in Section 2.2. The assumption of observing a CME in the plane of the sky in coronagraph images causes its apparent morphology to depend significantly on the observer's viewpoint. The CME leaving the Sun in the perpendicular direction to the observer provides an opportunity to observe the various CME structures. The coronagraphic observation reveals the "classic" three-part structure of CMEs: a bright central core, dark cavity and the front leading edge of the piled-up plasma [Illing and Hundhausen, 1985, Gopalswamy, 2004]. In the case of fast CMEs, a "five-part" structure better describes the CME morphology, including the sheath and shock front as additional components. Figure 1.10 illustrates the structure of a CME observed for two different events using the LASCO/C2 coronagraph.

Another important morphological parameter of CME is its size, quantified as angular width. It is important to note that the width observed in white-light images is the apparent width—essentially, the projected angular span of the CME on the POS, which differs from the true angular width. CMEs erupting close to the limbs are not affected significantly by the projection effect and their measured width is close to the true one. CMEs propagating along line-of-sight appears as a bright structure expanding around the central disc of the coronagraph, with their apparent angular width of 360°, is called

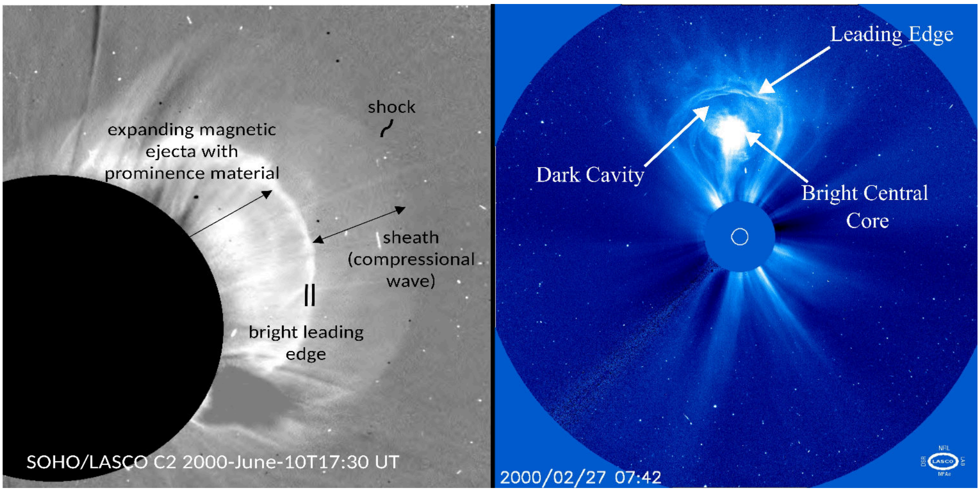

Figure 1.10: A schematic illustrating the various brightness features of a CME observed in SOHO/LASCO/C2 coronagraph. Left Panel: A five-part structure of a CME showing shock and sheath region. Adapted from Temmer and Bothmer [2022]. Right Panel: A classic three-part structure of a CME. Image Credit: NASA ESA/SOHO Team

"Halo" CME [Howard et al., 1982]. CMEs with an apparent angular width of $\geq 120°$ are referred to as partial halos. The average apparent angular width of non-halo CMEs, based on the SOHO/LASCO CME catalogue is reported in the range of $47° - 61°$ [Gopalswamy, 2004].

1.3.2.2 Kinematics of CMEs

The speed of CMEs can be determined by tracking the CME feature in the successive coronagraph image frames. The SOHO/LASCO CME catalogue allows to track the leading edge of a CME and generate the height-time ($h - t$) plots. A linear fit to the plot provides the average speed of the CME in Field-of-View (FOV) of the coronagraph. It is important to note that the speed derived from this approach is projected POS speed and should not be used in CME propagation models. The radial speed of CME front from the coronagraphic FOV vary between a few tens to 2000 km/s, with maximum value observed close to $\sim$ 3000 km/s [Gopalswamy, 2004, Gopalswamy et al., 2009, Temmer, 2021]. The average value of the CME speed in the POS is approximately 475 km/s, which is slightly higher than the slow solar wind speed Gopalswamy et al. [2009]. Figure 1.11 illustrates the distribution of apparent speed and width of all the CMEs reported in SOHO/LASCO CME catalogue. [Refer Gopalswamy, 2004, Gopalswamy et al., 2009, Webb and Howard, 2012, Temmer, 2016, 2021, and references in there to get more idea of various properties of the CMEs.]

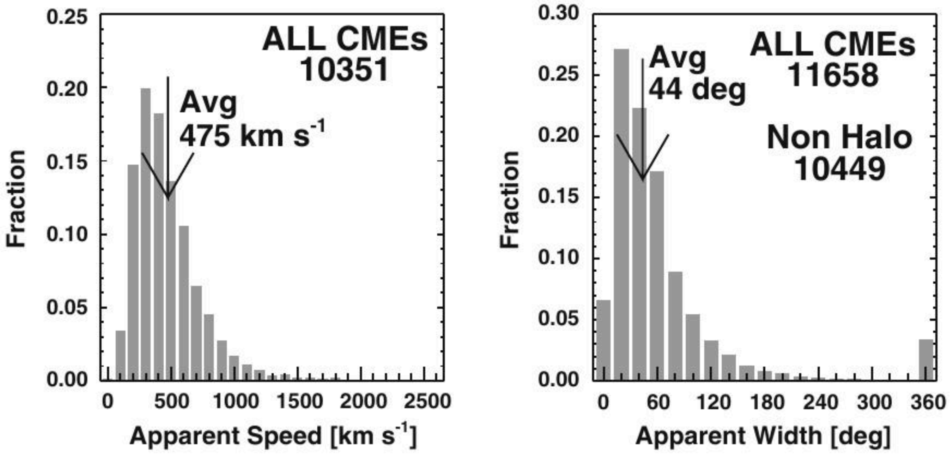

Figure 1.11: The POS speed and apparent angular width of all the CME identified up to end of year 2006. Adapted from Gopalswamy et al. [2009]

1.4 Thesis goal and outline

The discussions in the previous sections underscore the importance of studying impulsive solar phenomena, such as CMEs, solar flares, and SEPs, for effective space weather predictions. A deeper understanding of these phenomena is critical for enhancing our ability to forecast space weather events, thereby mitigating risks to modern, technology-dependent society. This improvement can be achieved either by refining existing theoretical models or developing new, data-driven models. However, the foundation of such studies lies in the availability of reliable, high-quality data.

This thesis aims to contribute to this field by compiling a robust catalogue of CME-ICME properties, with the overarching goal of improving the prediction of CMEs' behaviour in the heliosphere and, consequently, the space weather effects they induce. The research focuses on the Probabilistic Drag-Based Model [P-DBM, Napoletano et al., 2018], a semi-empirical model that describes CME propagation through the heliosphere using a probabilistic approach.

The first scientific objective of this thesis is to improve the prediction of CME arrival time and speed at 1 AU. This was accomplished by determining the PDF for the DBM [Vršnak et al., 2013] parameters using a catalogue of geo-effective CME-ICME properties. Since the values of DBM parameters are effectively unknown, the PDFs derived in this thesis offers a substantial improvement in predicting ICME arrival times.

The second science goal of this thesis is to extend the capabilities of P-DBM to predict CME arrivals in the whole heliosphere. To achieve this, a new catalogue of CME-ICME lineup events was compiled. The application of the P-DBM to this newly curated dataset provided key insights into how P-DBM parameters may evolve as a function of heliocentric distance.

A summary of each chapter is provided below.

- **Chapter 2: Coronal Mass Ejection: Observation and Cataloguing**
  This chapter discusses the various modes of CME observations and relevant spacecraft dedicated CME or space weather studies. It also reviews the in-situ signatures used to detect ICMEs After a detailed discussion of CME-ICME observation techniques, the chapter introduces several important catalogues of CME properties and ICME measurements. These catalogues form the basis for the data used in the studies conducted in this thesis.

- **Chapter 3: Coronal Mass Ejection: Propagation and Forecasting**
  This chapter focuses on the core research of this thesis. It discusses different versions of the DBM, including both the traditional and probabilistic approaches. The advantages of using P-DBM over traditional DBM are highlighted. Furthermore, the chapter outlines the methodology for refining the geo-effective CME-ICME list and the process of deriving PDFs from this list to strengthen the model.

- **Chapter 4: ICME Detection in the Heliosphere**
  This chapter addresses the detection of ICMEs throughout the heliosphere and is a key component of the thesis. It reviews several planetary ICME lists, which serve as the foundation for the extensive CME-ICME

lineup event database. The methodology for compiling this lineup catalogue is also described in detail.

- **Chapter 5: Discussion and Conclusion**
  The final chapter presents the results of these studies and explores the future scope of this research. It summarises the determination of the PDFs for DBM parameters using the geo-effective CME-ICME catalogue and compares these findings with those from previous studies. Additionally, this chapter discusses the application of the P-DBM to the CME-ICME lineup catalogue and the development of a Graphical User Interface (GUI) for future operational space weather forecasting using the P-DBM.

Chapter 2

Coronal Mass Ejection: Observation and Cataloguing

This Chapter focuses on observations of CMEs and ICMEs. The chapter begins with an overview of the historical evidence of CME observations. Subsequently, the current and future status of CME observation is elaborated, with reference to numerous spacecrafts such as SOHO, STEREO, SolO and others. Following the discussion of remote observations for CMEs, attention is shifted towards the in-situ measurements of ICMEs. The significant in-situ signatures of ICMEs have been systematically tabulated. After providing comprehensive discussion on the observational aspects of CMEs and ICMEs, chapter concludes with outlining various catalogues and datasets providing CME-ICME properties.

2.1 Introduction

CMEs have been observed for nearly 50 years with a wide variety of instruments as a result of the beginning of the space era. The launch of SOHO in 1996 led to the systematic observations of CME. In the pre-space era, the total solar eclipses provided a rare window for observing solar corona. During this small window, the chance of encountering a CME is extremely low. The 19th century witnessed many solar discoveries, and this century's photography era helped us discover CME. Figure 2.1 is a drawing of the eclipse observed on 18th July 1860 by Ernst Temple in Torreblanca (Spain) showed a bubble-shaped structure disconnected from the Sun. Later, Jack Eddy identified that bubble as CME and this drawing accredited as 1^{st} recorded CME observation.

Once the coronagraph was invented, continuous monitoring of the corona from space began with the "Mariner-2" spacecraft in 1962 [Webb and Howard, 2012]. One decade later, in 1973 CME was first observed by Richard Tousey using observation of Orbiting Solar Observatory (OSO)-7 [Webb and Howard,

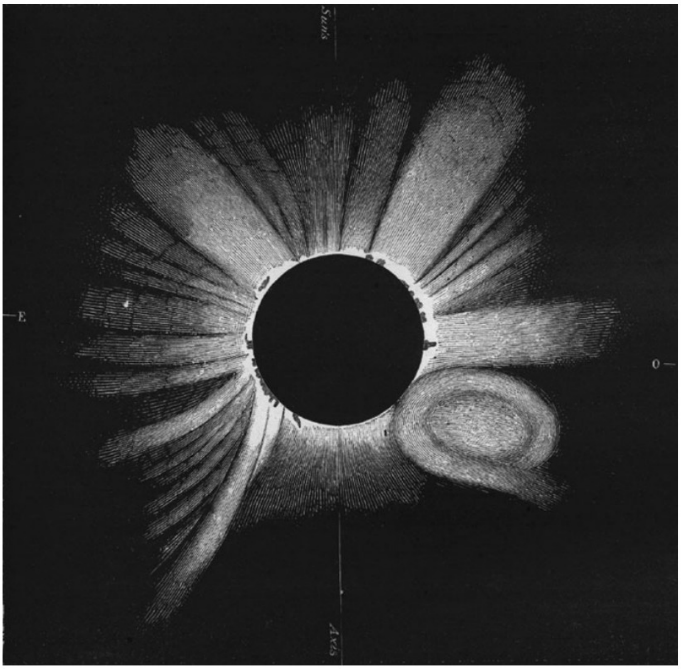

Figure 2.1: Drawing of the 1860 solar eclipse that is believed to be the first observation of CME. Adapted from Howard [2014]

2012, Howard, 2014, Sachdeva, 2018]. OSO-7 witnessed a total of 27 CMEs before entering Earth's atmosphere in 1974. The term "Coronal Mass Ejection" became popular with Skylab observations [Gosling et al., 1976]. The satellite P78-1 of the US Department of Defence witnessed the discovery of Earth-directed "halo" CMEs [Howard et al., 1982, Kunow, 2007, Webb and Howard, 2012]. The development in CME studies in the 1980s laid the foundation of the modern CME era. The classic three-part structure of CMEs was discovered by NASA's Solar Maximum Mission (SMM). Talking about the number of CME events reported from this era then Skylab reported 115 events, Solwind and SMM observed 998 and 1351 CME events respectively [Webb and Howard, 2012]. Figure 2.2 shows a timeline of the launch of spacecraft relevant to the investigation of CMEs.

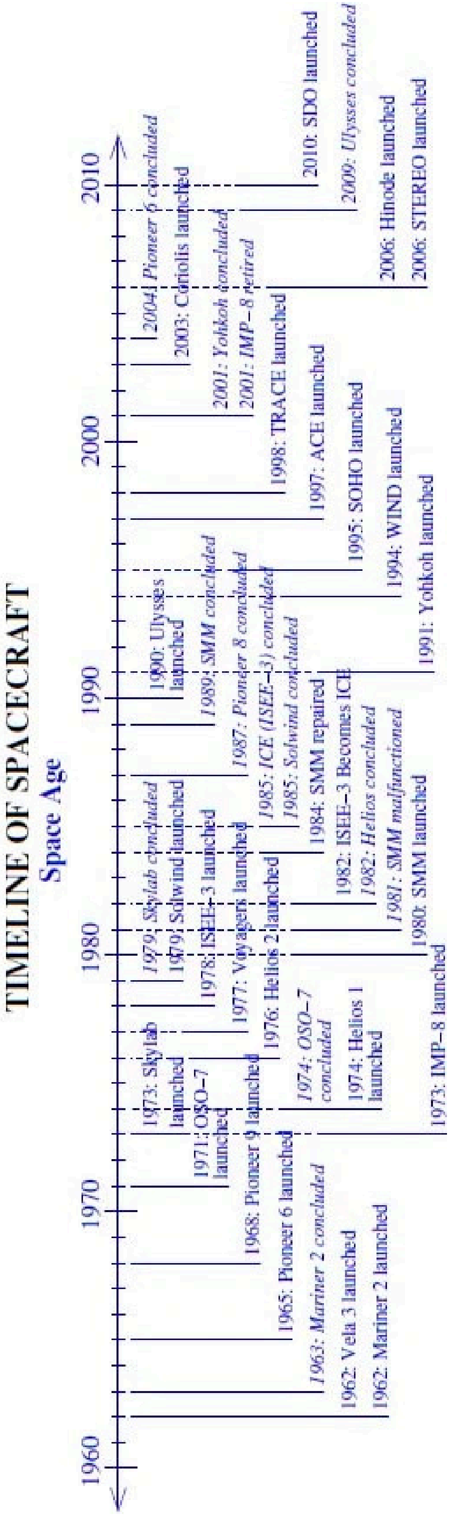

Figure 2.2: The timeline for historical observations of CMEs from space. Adapted From Webb and Howard [2012]

2.2 Coronagraph

2.2.1 SOHO/LASCO

The SOlar and Heliospheric Observatory (SOHO) is a collaborative mission between the National Aeronautics and Space Administration (NASA) and the European Space Agency (ESA), designed to study the Sun comprehensively from its deep core to its outer corona, as well as the solar wind. It was launched on the 2^{nd} December 1995 with three principal science objectives. (1) Study the interior structure of the Sun using helioseismology. (2) Study the physical process that heats the solar corona. (3) Investigate the physical mechanism that causes the solar wind acceleration [Domingo et al., 1995]. SOHO is equipped with a suite of 12 scientific instruments, categorized into three primary groups:(1) Helisesimology (2) Solar Atmosphere Remote Sensing and (3) Solar Wind 'In-situ'.

Among these instruments, the Large Angle and Spectrometric Coronagraph (LASCO) one of particular relevance to this thesis. LASCO is a package of three coronagraphs (namely C1, C2, and C3) with overlapping FOVs to address the essential question in coronal physics. These include: (1) What mechanisms are responsible for heating the corona? (2) How and where does the acceleration of solar wind occur? (3) What triggers coronal transients, and how do they contribute to the large-scale changes and evolution of coronal structures? [For further details regarding the scientific objectives and technical specifications of LASCO, refer to Brueckner et al., 1995]

- **C1 coronagraph:**
  C1 was designed to observe the innermost corona having FOV 1.1 to 3 $R_{\odot}$. It used the Fabry-Perot interferometer type spectral band pass filter, enabling the detailed observations of lower corona and identification of small-scale structures. Due to some technical difficulties, C1 ceased its operation during the early mission phase.

- **C2 coronagraph:**
  C2 has a field of view of 2 to 6$\mathrm{R}_{\odot}$ to capture images of the middle corona. It is a prime instrument for detecting CMEs in this range. C2 captures the larger and more distant structure of solar eruptions in broadband spectral filters.

- **C3 coronagraph:**
  C3 has a field of view of 3.7 to 30 $R_\odot$ to observe the outer corona. The wide field of view of C3 allows researchers to monitor the development of CMEs and their propagation in the heliosphere. C3 plays a crucial role in space weather forecasting by tracking CMEs from the Sun to interplanetary space.

From its operation start in January 1996 to August 2024, LASCO observed nearly 36000 CMEs. This collection of data over 28 years resulted in one of the most extensive catalogues of CME properties named SOHO LASCO CME Catalogue[Gopalswamy et al., 2009, 2024]. A more detailed discussion of this catalogue can be found in Section 2.6.1.

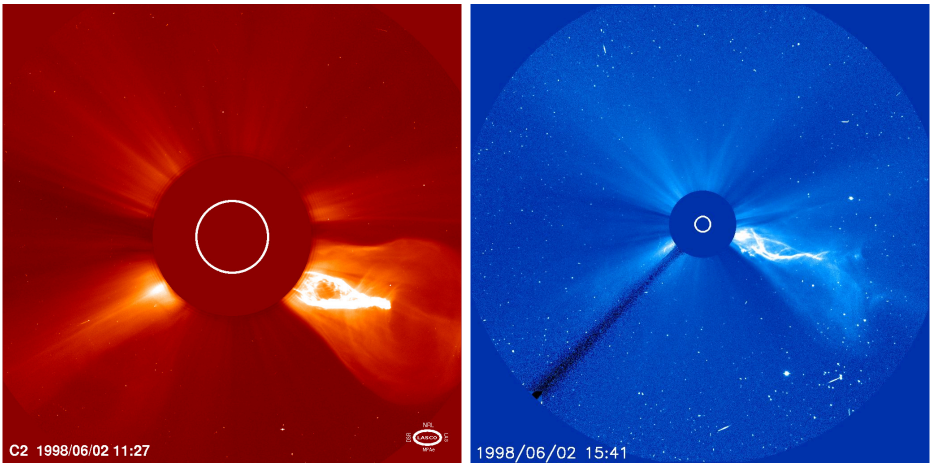

(a)

(b)

Figure 2.3: The twisted, helical shaped CME observed by LASCO. The width of CME blast is relatively narrow and plasma is twisted, which is unusual. Credit: NASA/NRL

2.2.2 STEREO/SECCHI/COR

The Solar Terrestrial Relations Observatory (STEREO) is the third mission in NASA's Solar Terrestrial Program (STP); under this mission, two identical space-based observatories were launched on 25th October 2006, one leading the Earth in its orbit (STEREO-A) and one trailing (STEREO-B). The two spacecraft gradually separate at a rate of 45° per year as viewed from the

Sun. This arrangement was done to obtain the stereoscopic observations of the Sun from different vantage points for the following scientific objectives: (1) Understand the cause and mechanism of CME initiation. (2) Characterise the propagation of CMEs through the heliosphere. (3) Discover the mechanisms and sites of solar energetic particle acceleration in the low corona and the interplanetary medium. (4)Develop a 3D, time-dependent model of the magnetic topology, temperature, density, and velocity structure of the ambient solar wind. These science objectives are achieved through four measurement payload packages, comprising a total of 13 scientific instruments [Kaiser, 2005].

The Sun Earth Connection Coronal and Heliospheric Investigation (SECCHI) [Howard et al., 2008] instrument suite is of particular relevance, consisting of five optical telescopes designed to observe the entire inner heliosphere, starting from the solar surface and extending to interplanetary space between the Sun and Earth. Since the primary objective of the STEREO mission is to deepen our understanding of CMEs, SECCHI specifically addresses the following key questions: (1) What configuration of the corona leads to a CME? (2) What is the 3D structure and kinematic properties of CME? (3) What is the 3D structure of various coronal transients? (4) How does a CME propagate in the heliosphere and interact with interplanetary space? [Howard et al., 2002] The SECCHI instrument suite accomplishes its scientific objectives through two groups of instruments: (i) Sun Centered Image Package (SCIP) which is set of two white light coronagraphs namely COR-1 and COR-2 and EUVI (discussed further in Section 2.3.2) (ii) two heliospheric imagers namely HI-1 and HI-2 (elaborated upon in Section 2.4.1)

- COR-1:
  The COR-1 is classic Lyot-type internally occulting and the first space-borne refractive coronagraph. It has a FOV extending from 1.4 to 4 $R_\odot$. The internal occultation enhances spatial resolution near the solar limb, although it introduces additional noise due to instrumentally scattered light. COR-1 performs observations in three states of linear polarization (-60°, 0° and +60°) to mitigate the effect of stray light. These polarisation sequences are captured within a 10-second interval to minimise variations caused by the dynamic evolution of the solar corona. Additionally, pixel binning is employed to enhance the signal-to-noise ratio. (For a more detailed discussion of the instrument's design and

operation, refer to Section 3 of Howard et al. [2008].)

- COR-2:
  The COR-2 is an externally occulted coronagraph, similar in design to the LASCO C2 and C3. It provides FOV ranging from 2 to 15 $R_\odot$ to complement the COR-1 observations. The spatial resolution of COR-2 is 5× compared to LASCO C3 and 3× temporal resolution. While the standard observational sequence of COR-2 mirrors that of COR-1, low-resolution total brightness images are generated by summing the polarised images, which are then transmitted via the beacon channel. Additionally, in certain cases, two images are taken with polarisation angle of 0° and 90° rapidly without reading CCD in between exposures. (Section 4 of Howard et al. [2008] provides detailed information on COR-2's design and operation.)

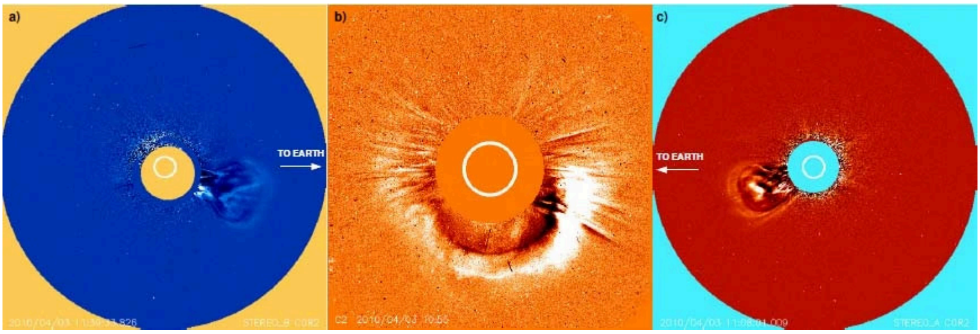

Figure 2.4: Image of the same Earth-Directed CME observed from different vantage points within an hour. (a) STEREO-B/COR-2 (b)LASCO/C2 (c) STEREO-A/ COR-2. Adapted from Webb and Howard [2012]

2.2.3 Solar Orbiter/ METIS

Solar Orbiter (SolO) was launched on 10th February 2020 with the mission of exploring the Sun and heliosphere from within 0.28 AU and conducting observations of the Sun's polar regions from outside the ecliptic plane. The mission seeks to address several key scientific questions: (1) What drives the solar wind, and where does the coronal magnetic field originate? (2) How do solar transients drive heliospheric variability? (3) How do solar eruptions produce energetic particle radiation that fills the heliosphere? (4) How does the solar dynamo work and drive connections between the Sun and the heliosphere? [Müller et al., 2020] To achieve these objectives, the SolO is equipped with four in-situ and six remote sensing instruments. (Refer Müller et al. [2020] to get a more scientific insight into the SolO)

Metis is one of the most advanced instruments onboard the SolO, as it is the first coronagraph capable of simultaneously observing the off-limb solar corona in both visible and ultraviolet light. The FOV of Metis is spanning the solar atmosphere from 1.7 $R_\odot$ to 9 $R_\odot$. Metis is designed to answer the following critical questions: (1) How is energy deposited in the polar regions where the fast solar wind is generated and accelerated? (2) What are the sources of the slow solar wind at lower latitudes? (3) How does the global corona evolve, and how does it give birth to the huge CME characteristic of solar activity? [Antonucci et al., 2020]. Metis is capable of imaging the solar corona in both the UV band at 121.6 nm (HI Lyman-α line) and the visible light band between 580-640 nm. This dual-channel capability permits it to capture reliable coronal dynamics and solar wind interactions across several wavelengths. Additionally, Metis utilizes a creative occulter design to reduce stray light and improve the contrast of coronal observations, particularly in adverse conditions close to the Sun. To get insight into the physical conditions of the corona, including electron density and outflow velocities, the sensor of Metis additionally combines polarimetry in visible light with intensity measurements in UV. (More details on science objectives and instrument design are provided in Antonucci et al. [2020].)

2.2.4 Aditya L1/ VELC

The Aditya-L1 is India's first space-based mission, launched by the Indian Space Research Organization (ISRO) to study the Sun. The spacecraft carries a total of seven payloads: four instruments dedicated to making remote observations of the Sun and three designed to perform in-situ measurements of particles and fields at the L1 point. Aditya-L1 is pursuing the following scientific objectives with the utilisation of these onboard instruments: (1) Diagnostics of the large and small scale structures in the solar corona (2) Magnetic topology and field measurements in the solar corona (3) Origin and dynamics of Solar flares and CME (4) Spectral energy distribution in solar flares (5) Spatially resolved solar spectral irradiance (6) Formation and dynamics of solar prominences

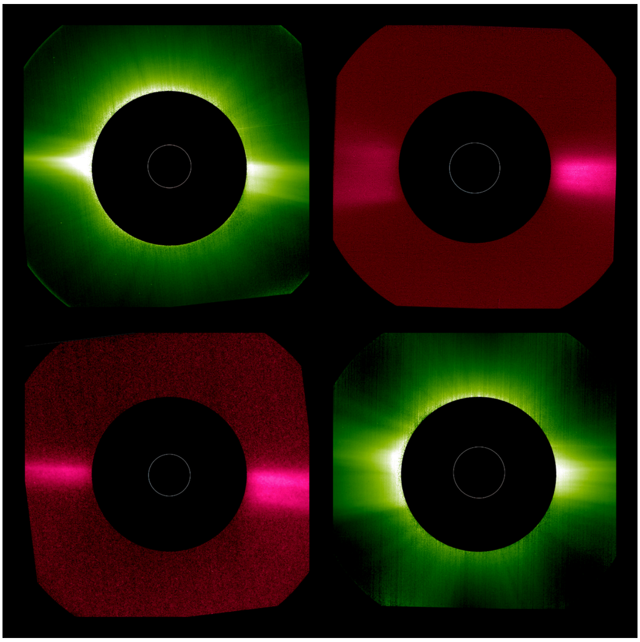

Figure 2.5: The first light captured by Metis on 15th May 2020 is shown in the left column. The visible light image (shown in green) shows the two bright equatorial streamers and fainter polar regions. The right column shows the image taken just after the Solar Orbiter's first perihelion. Credit: Metis Team

and filaments (7) Coronal abundances and first ionization potential effects (8) Solar wind composition and particle energy distribution (9) Measurements of the magnitude and variability of the interplanetary magnetic field. (Refer to Tripathi et al. [2023] for further details regarding the mission.)

One of the most notable instruments on board Aditya-L1 is the Visible Emission Line Coronagraph (VELC). It's an internally occulting coronagraph capable of performing observations in both visible and infrared wavelengths. The VELC is distinguished by its ability to carry out simultaneous imaging, spectroscopy, and spectro-polarimetry, especially near the solar limb. The FOV of VELC is 1.05 $R_\odot$ to 3 $R_\odot$ which enables the VELC to study the CME dynamics close to solar disk for the first time ever. Furthermore, VELC is the first space-based device capable of spectro-polarimetric observations in the Fe XIII 1074.7 nm infrared line, allowing for precise measurements of the coronal magnetic field's topology. This capacity represents a substantial leap in solar observation, providing fresh insights into the corona's magnetic structures from space. (Refer Prasad et al. [2017] for more details of the instrument.)

2.3 EUV Imaging

2.3.1 SOHO/ EIT

The Extreme ultraviolet Imaging Telescope (EIT) is an onboard instrument of SOHO, designed to provide images of the solar corona and transition region, including the solar disc up to 1.5 $R_\odot$. EIT acquires EUV images of the Sun in 4 emission lines (FeIX 17.1 nm, FeXII 19.5 nm, FeXV 28.4 nm and HeII 30.4 nm) corresponding to a temperature range of $6 \times 10^4 K$ - $3 \times 10^6 K$. EIT data are critical for understanding the dynamics and evolution of coronal structures over an extensive range of physical parameters, including time, size, and temperature. These data help to answer fundamental issues about the mechanisms governing coronal heating and solar wind acceleration. The He II line targets the transition zone, allowing for the tracing of coronal hole bases. In contrast, the Fe lines focus on observing the lower corona, providing insights into its structure and activity. (Refer Delaboudinière et al. [1995] for instrument design and science objective)

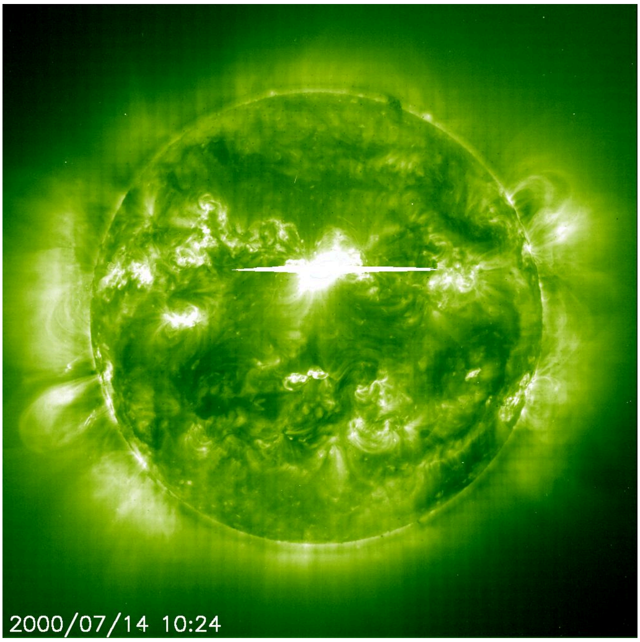

Figure 2.6: The solar flare observed on 14th July 2000 saturates the UV camera. Credit: EIT Team and NASA/ESA

2.3.2 STEREO/ EUVI

The Extreme Ultara Violet Imager (EUVI) is part of SECCHI-SCIP package to observe the chromosphere and lower corona of the Sun. It observes the Sun in four distinct EUV emission lines between 17.1 - 30.4 *nm*. These four emission lines are namely: HeII 30.4 *nm*, FeIX 17.1 *nm*, FeXII 19.5 nm and FeXV 28.4 *nm*, which are same as SOHO/EIT. The EUVI offers a FOV of ± 1.7 $R_\odot$, allowing for comprehensive observations of the solar atmosphere from the chromosphere through to the lower corona.

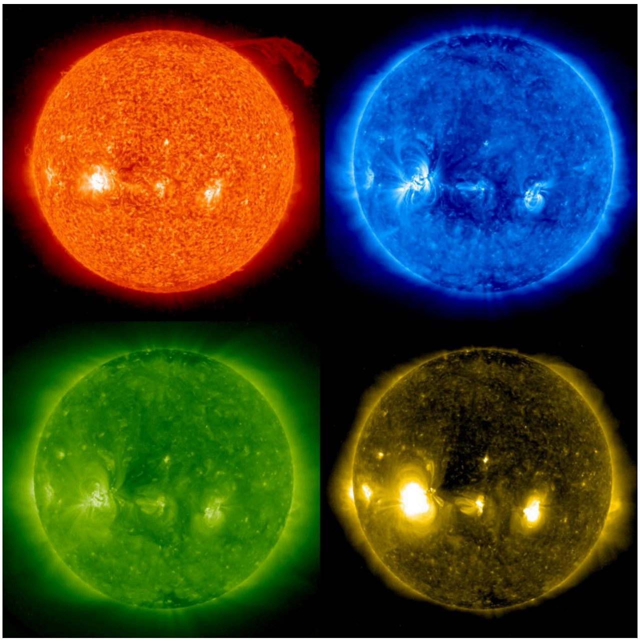

Figure 2.7: The image of the Sun taken by EUVI in all four wavelengths 30.4 *nm* (red), 17.1 *nm* (blue), 28.4 *nm* (yellow) and 19.5 *nm* (green) on the 6th June 2007. Active regions appear as bright patches in all the images. Also, eruptive prominence can be seen in 30.4 *nm* wavelength. Credit: STEREO Team

2.3.3 SDO/AIA

The Solar Dynamic Observatory (SDO) was launched on 11th February 2010 as the first dedicated space weather mission. The primary objective of SDO is to understand the solar variations that impact life on Earth and human technology, with the long-term goal of acquiring predictive capabilities for solar activity. The science objective of SDO is to answer the following key questions: (1) How is the magnetic field of the Sun generated? (2) How is the stored magnetic energy converted and released into the heliosphere and geospace in the form of solar wind, energetic particles and variations in solar irradiance? SDO is equipped with three instruments to accomplish its scientific goal. Together, these three instruments provide continuous monitoring of the Sun's outer atmosphere and magnetic activity. (Refer Pesnell et al. [2012] for mission's science goals and technical capabilities of SDO)

The Atmospheric Imaging Assembly (AIA) is a crucial instrument onboard SDO, consisting of four telescopes AIA provides simultaneous high-resolution full disk images of the solar corona and transition region extending up to 0.5 $R_\odot$. It provides narrow-band imaging in seven extreme UV and three UV channels [Lemen et al., 2012]. AIA has provided critical insights into solar flares and CMEs through its ability to observe solar corona in great detail. (Refer Lemen et al. [2012] for science objective and technical specification of AIA)

2.3.4 Solar Orbiter/ EUI

The Extreme Ultaviolet Imager (EUI) is another remote sensing instrument aboard the Solar Orbiter. TheEUI consists of a suite of three telescopes: a Full Sun imager and two high-resolution imagers to observe the chromosphere and corona. The full Sun imager has a FOV of 2 $R_\odot$ diameter at perihelion, allowing it to observe the entire solar disc even when the spacecraft is pointed at the solar limb. The instrument functions with two bandpasses—30.4 nm and 17.4 nm—facilitating imaging of the transition area and the corona. The UV observation from Metis complements those of the full Sun imager, together providing the SolO with the ability to image the solar corona in EUV up to 10 $R_\odot$. The two high-resolution imagers specialize in observing the Sun in Lyman-α and EUV channels, allowing for high-resolution studies of solar dynamics. (Refer Rochus et al. [2020] for more detailed technical and optical aspects of the instrument.)

2.3.5 Aditya L1/ SUIT

The Solar Ultaviolet Imaging Telescope (SUIT) is an instrument on board Aditya-L1, designed to measure the solar radiation emitted in the near ultra-

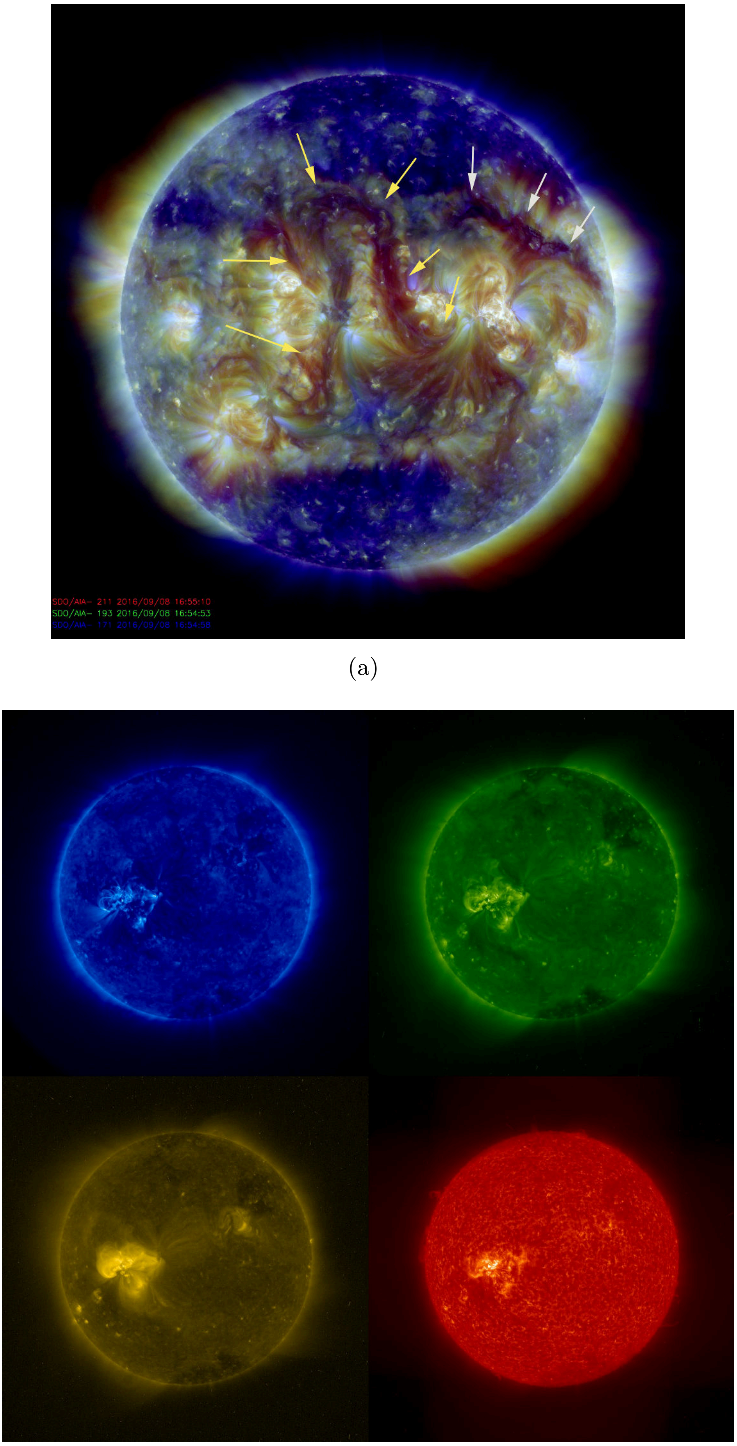

(a)

(b)

Figure 2.8: (a)The composite image using 17.1, 19.3 and 21.1 *nm* wavelengths is created. The white and yellow arrow shows two different elongated filaments on the solar disk. (b) Sun in four different extreme UV light wavelengths that AIA uses for observations. Credit: NASA SDO Team

violet wavelength range of 200-400 nm. SUIT provides full disk observations of the Sun across 11 wavelength bandpasses to address Aditya-L1's science objectives. The images captured through these 11 filters are useful for long-term study of spatially resolved solar irradiance. In addition to its 30-minute standard cadence time, SUIT also has another operation mode where images in 8 filters are captured every 30 s for the region of interest. This mode is particularly useful for studying the dynamics of the solar atmosphere. Furthermore, It is equipped with an automatic flare detection and location system on board. (See Tripathi et al. [2017] for instrument design and performance)

2.4 Heliospheric Imagers

2.4.1 STEREO/ SECCHI-HI

The main objective of SECCHI-HI is to make a visible light observation of CMEs and other structures as they transit from the corona into the heliosphere. At the time of its development, HI adopted an innovative method by carrying out all observations in a shutterless mode. There was just an opening cap to protect the instrument during launch time. The two imagers, HI-1 and HI-2, are positioned at angles of 13° and 53° from the spacecraft's principal axis, respectively. HI-1 has a FOV of 20°, while HI2 has a wider FOV of 70°. Due to their onboard optical arrangements, HI-1 and HI-2 shared a FOV of approximately 5°. Both telescopes are positioned at an opening angle of 45° from the solar equator, providing a comprehensive view along the Sun-Earth line, spanning from the COR-2 instrument to Earth. The HI-1 and HI-2 instruments have contributed significantly to the observation of CMEs, resulting in one of the most extensive catalogues of CMEs passing through the heliosphere since the start of the STEREO mission. The catalogue is publicly accessible under Heliospheric Cataloguing, Analysis and Techniques Service (HELCATS)[1] project framework.

2.4.2 Solar Orbiter/ SolOHI

SolOHI is designed to make remote observations of Thompson scattered light of the outer corona. Although it is based on SECCHI-HI's design, substantial

---

[1] Link to HELCATS project: `https://www.helcats-fp7.eu/index.html`

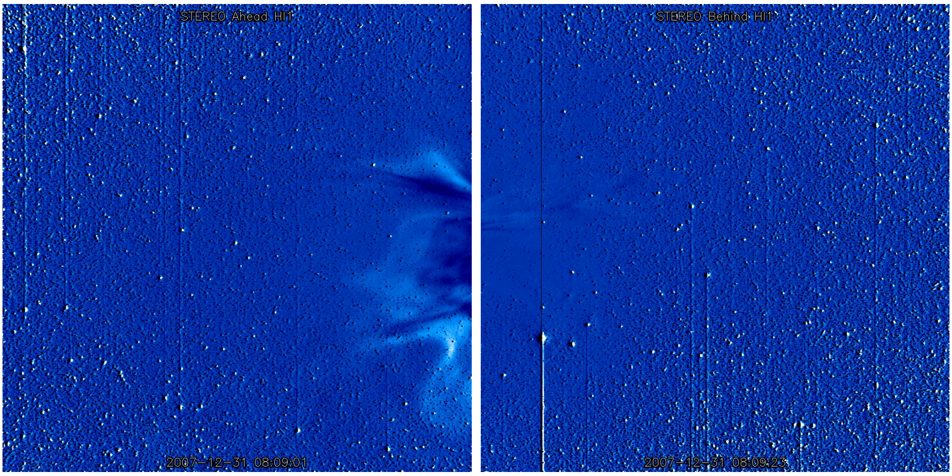

(a) (b)

Figure 2.9: The CME event observed by STEREO-A/B on 31^{st} December 2007. (a): STEREO-A/HI-1. (b): STEREO-B/HI-1. CME leading edge clearly visible in the left column. Credit: NASA

modifications have been made to optimise resources and satisfy the unique scientific goals of the SolO. The SolOHI uses a single telescope design contrast to SECCHI-HI, with double FOV compared to SECCHI/HI-1. The wide FOV of SolOHI spanned over 5° to 40° elongation from the Sun, allowing it to capture both the solar wind and CMEs in an extensive area (see Howard et al. [2020] for a brief overview of the science objective and optical design of the instrument).

2.4.3 PSP/ WISPER

Parker Solar Probe (PSP) is NASA's historic mission to study the Sun from an unprecedented proximity—within 18.8 $R_\odot$ above the solar surface. During the 7 years of mission duration, the PSP will spend approximately 937 hours inside 20 $R_\odot$, 440 hours inside 15 R $R_\odot$ and 14 hours inside 10 $R_\odot$. The PSP has three primary science objectives: (1) Trace the flow of energy that heats the corona and accelerates the solar wind. (2) Determine the structure and dynamics of the plasma and magnetic field at the source of solar wind. (3) Explore the mechanisms that accelerate and transport energetic particles. The PSP was launched on 12th August 2018, carrying four instruments designed

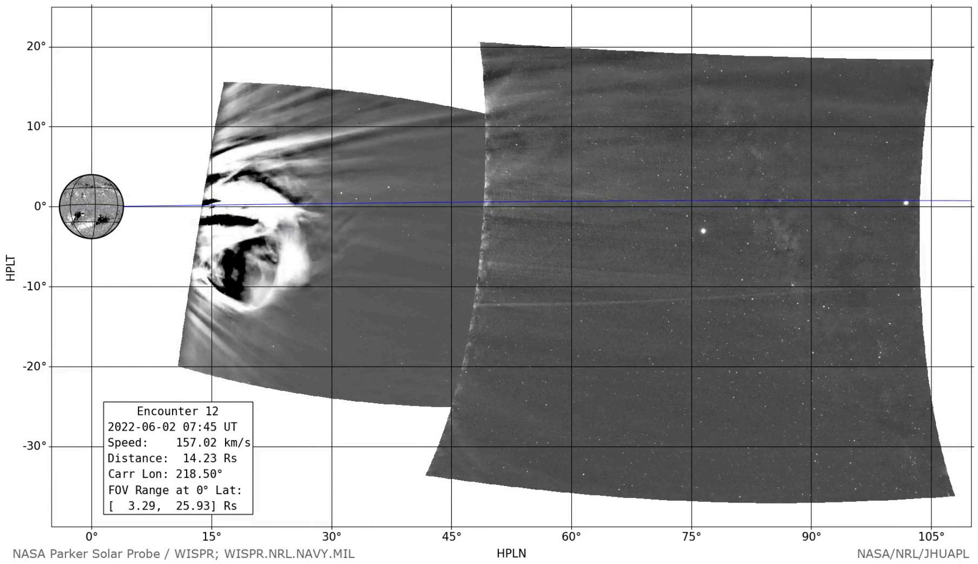

Figure 2.10: The CME event occurred on 2^{nd} June 2022 is recorded by WISPR during 12^{th} nearby approach of PSP. Credit: NASA/NRL/JHUAPL

to achieve these scientific goals. (Refer Fox et al. [2016] for more detailed information of the PSP)

Among the four instruments on board, WISPR is the only imaging instrument consisting of two telescopes. WISPR provides the continuous synoptic observation of the inner heliosphere. Its FOV is centred on the ecliptic plane with little offset from the Sun. WISPR images the inner corona in the range of 13.5° to 108° elongation angles with spatial resolution of 6.4 arcmin. (Refer to Vourlidas et al. [2016] for a more detailed review of the instrument)

2.5 In-situ measurement of CME

The final stage of CME observations deals with observing them on Earth or in the heliosphere. While coronagraphic observations offer vital information about CME behaviour, they do not provide information about the CME composition. However, ICMEs, which are responsible for major space weather effects, make their study vital. Thanks to the space era, the study of ICMEs is relatively easy.

One of the most studied signatures is the magnetic field. ICME boundaries are often identified as a tangential discontinuity in solar wind data. Although not all ICMEs exhibit obvious boundaries, this discontinuity has a small uncertainty in many instances. For instance, due to the complex structure of the ICMEs, boundaries in cases of field-line reconnection might be difficult to observe. [Vasquez et al., 2001, Zurbuchen and Richardson, 2006]. A common trait associated with ICMEs is the reduced variability of the magnetic field ($B3$). The magnetic field inside an ICME tends to be smoother compared to the turbulent "sheaths" observed ahead of fast ICMEs. The southward interplanetary magnetic field component (B_z) is strongly enhanced within ICMEs, making them a key driver of geomagnetic storms [Richardson et al., 2001]. In the "magnetic cloud" type of ICMEs, the magnetic field is enhanced and rotates slowly over a large angle. It also exhibits low proton temperature and plasma β [Klein and Burlaga, 1982].

In the ground state, an empirical correlation exists between the solar wind speed (v_{sw}) and the proton temperature (T_{p}) [Lopez, 1987]. However, ICME deviate from this correlation, exhibiting unusually low T_{p} [Cane et al., 1996]. ICME detection based on T_{p} has the advantage of making observations accessible since the beginning of the space era. When a CME passes through the spacecraft, plasma and magnetic field data are recorded in situ, and a time series of observations is created. Over many years, ICMEs are identified as major fluctuations in solar wind state using those in-situ data.

From the direct measurements of ICMEs in the early 1970s, our understanding of their composition has greatly improved. For example, it has been observed that He abundance is notably higher, along with a high ionisation state of O and Fe in the ICME shocks [Borrini et al., 1982, 1983, Bame et al., 1979, Howard, 2011]. However, the knowledge of ICME composition doesn't provide insight on the initial CME composition, as CMEs spend several days in the interplanetary medium before reaching the spacecraft. A detailed review of all the in-situ ICME signatures is provided by Zurbuchen and Richardson [2006]. Some of the signatures are summarised in Table 2.1. Figure 2.11 shows in-situ measurements taken by ACE spacecraft of various ICME events. [Also, refer to Davies, 2021, Pal, 2020, for the summary of ICME signatures.]

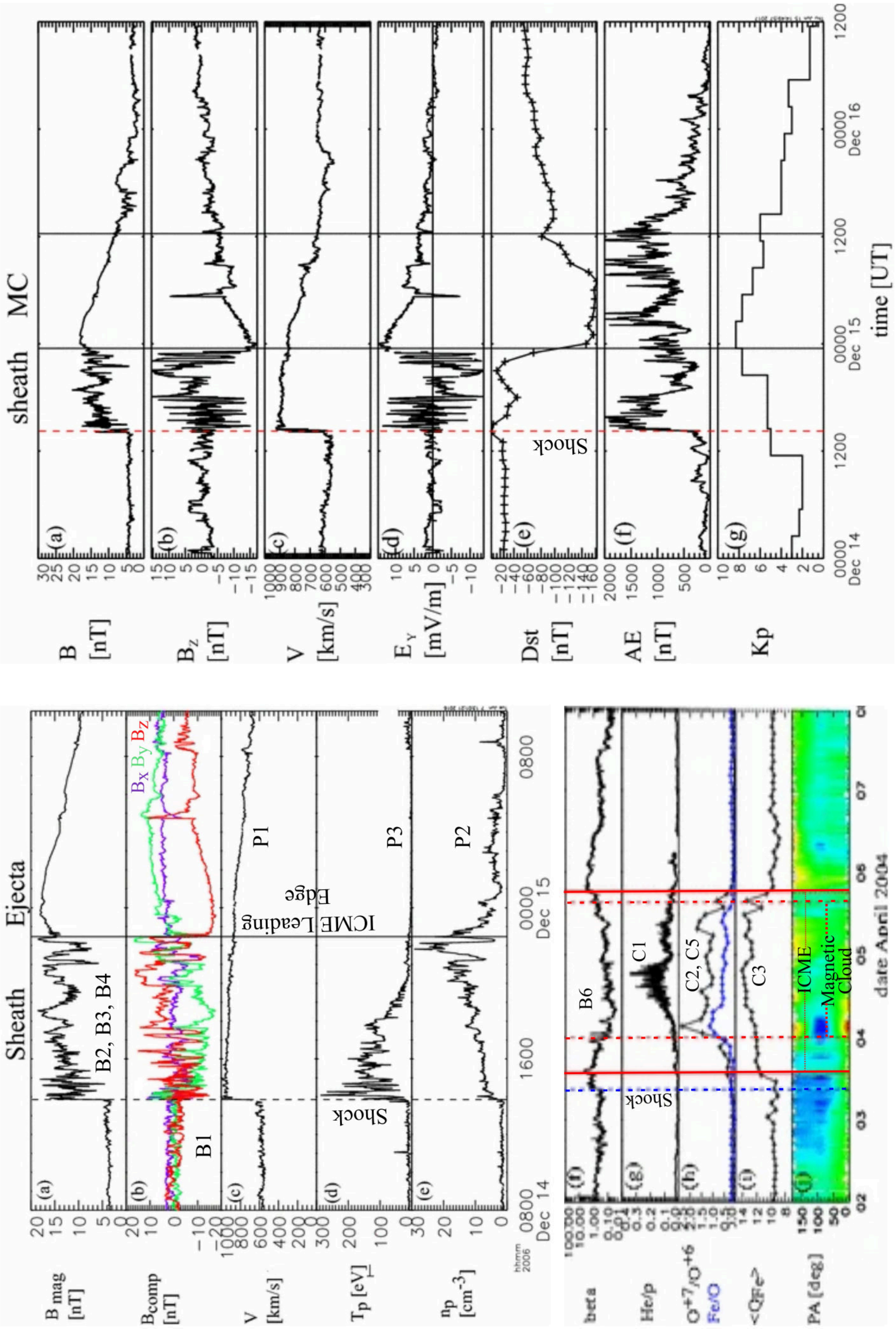

Figure 2.11: Examples of in-situ signatures of various ICMEs with a magnetic cloud (MC) and sheath region at 1 AU. The measurements are from the ACE spacecraft and OMNI[a] data. Adapted from: Kilpua et al. [2017]

[a] OMNIWeb : `https://omniweb.gsfc.nasa.gov/hw.html`

Signature	**Description**
B1: B rotation	$\gg 30°$, smooth
B2: B enhancement	>10nT
B3: B variance decrease	
B4: Discontinuity at ICME boundaries	
B5: Field line draping around ICME	
B6: Low plasma β	$\beta = \frac{\Sigma nkT}{B^2/2\mu_0} < 1$
P1: Monotonic declining velocity profile	
P2: Proton density decrease	$n_p \leq 1$ cm^{-3}
P3: Proton Temperature decrease	$T_p < 0.5\mathrm{T}_{exp}$, $T_p \ll T_e$
P4: Electron temperature decrease	$\mathrm{T}_e < 6\times10^4 K$
P5: Upstream forward shock	
C1: Enhanced α/p^+ ratio	$\mathrm{He}^{+2}/\mathrm{H}^+ > 8\%$
C2: Elevated oxygen charge states	$\mathrm{O}^{+7}/\mathrm{O}^{+6} > 1$
C3: High Fe charge states	
C4: Occurrence of He$^+$	$\mathrm{He}^+/\mathrm{He}^+2 > 0.01$
C5: Enhancement of Fe/O	
C6: High ^{3}He/^{4}He	$\frac{CME}{Photosphere} > 2$
W1: Ion acoustic waves	
S1: Bidirectional electrons strahl	
S2: Bidirectional $\sim$ MeV ions	
S3: Cosmic ray depletions	
S4: Bidirectional cosmic rays	

Table 2.1: List of in-situ signatures of ICMEs at $\sim$ 1 AU heliocentric distance. These signatures are mainly categorised into magnetic field (B), plasma dynamics (P), plasma composition (C), plasma waves (W), and suprathermal particles (S). Adapted from Table-1 of Zurbuchen and Richardson [2006]

2.6 CME databases

Since CMEs typically appear as diffuse objects in the coronagraphs, current techniques for detecting them encounter several challenges. These challenges arise from both technological limitations and the inherent nature of CMEs, which display complex and dynamic behaviours. Some of the key obstacles include interference from background noise such as the presence of streamer, cosmic rays and SEPs. Additionally, the highly variable nature of CME and the difficulties in detecting weak CMEs pose significant challenges. Despite these drawbacks and limitations, various approaches have been developed to detect and track the motion of CMEs. These efforts have given birth to many CME catalogues, ranging from manual compilation to automatic detection algorithms.

2.6.1 CDAW

The CME catalogue hosted at Coordinated Data Analysis Workshop (CDAW)[2] provides simple but very efficient analysis of each CME events observed by LASCO, which has been operational since 1996 [Gopalswamy et al., 2009, 2024]. This catalogue is completely manual and requires human interactions, where the user tracks the CME through the running difference images of C2 and C3. The interface of the catalogue allows the user to produce a height-time plot of each CME event. The implementation of a linear fit to the height-time profile provides a first-order estimation of POS speed, while quadratic fit provides a second-order speed and acceleration. The first layer of the catalogue is a year-month matrix; each element of this matrix represents the monthly list of CME. This monthly list includes a detailed analysis of each CME event, that includes the time of its first appearance in C2, accompanied by a complete movie of C2 and C3 for that particular event, along with GOES X-ray flux data. The central position angle and angular width of CME is also derived from the observations. The value of angular width leads to the classification of the event as follows: “halo” when it spans 360°, a “partial halo” when it spans 120° or more, and “wide” when it covers 60° or more. Additionally, The catalogue provides essential kinematic data, including the linear speed, 2^{nd} order speed at final height and at 20 $R_\odot$, acceleration, mass, and kinetic energy. The catalogue provides remarks for each event and measured position angle (an angle along the CME height is measured) along with links to movies and plots for each event.

Research using the CDAW CME catalogue has provided great insights into

---

[2] Link to CDAW catalogue: `https://cdaw.gsfc.nasa.gov/CME_list/`

the occurrence, evolution and geo-effectiveness of CMEs. CDAW catalogue has a significant impact in improving space weather forecasting models and advancing our understanding of the Sun-Earth connection. Its extensive nature allows for a refinement of models that predict the arrival times of CMEs at Earth and evaluate their potential geomagnetic effects.

2.6.2 SEEDS

The human eye serves as an exceptional tool for identifying coronal mass ejections in coronagraphic observations. However, the process of manual cataloguing is quite labour-intensive and prone to errors due to operator bias, which adds errors to the data. Many automated catalogues have been built in an attempt to address these biases. These new methods provide robust CME analysis over massive datasets that are currently available and promise significant benefits for future missions.

The Solar Eruptive Event Detection System (SEEDS)[3] is a software tool to automatically detect CMEs based on time series of coronagraph using threshold segmentation technique [Olmedo et al., 2008]. In the first stage of development, this algorithm was implemented on LASCO data. This initial investigation reproduced 75% of CME events from CDAW catalogue, later on, the same algorithm was implemented on SECCHI/COR data. This system stands out from other CME catalogues through its focus on automation, which reduces the need for human intervention and ensures more consistent and frequent updates. The height, velocity, and acceleration of CMEs are automatically recognised by the detection algorithm, which is based on a 2D to 1D projection method. Additionally, the approximate shape of the CME leading edge has been extracted using a threshold segmentation technique, ensuring a more accurate and efficient analysis.

2.6.3 CACTus

CACTus[4] is a software package for 'Computer Aided CME Tracking'. Initially, CACTus was developed to detect the CMEs in an image sequence from LASCO. Later on, it is upgraded for COR-2 and HI-1 data. It uses the Hough transform to detect the CME as bright ridges in (time, height) maps [Berghmans et al.,

---

[3] Link to SEEDS catalogue: `http://spaceweather.gmu.edu/seeds/`

[4] Link to CACTus: `https://www.sidc.be/cactus/`

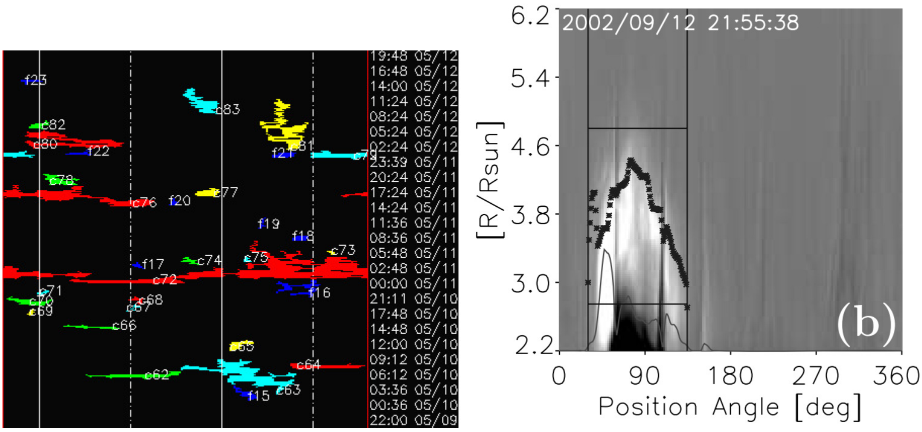

(a) (b)

Figure 2.12: (a) Snapshot of CACTus CME list. where CME events are marked in (time, height) map. Credit: CACTus/SIDC. (b) Identification of CME leading edge along CME position angle. Adapted from Olmedo et al. [2008].

2002, Robbrecht and Berghmans, 2004]. After CME detection, it applies clustering and morphological closing operations to mark out different CMEs. The output of this software is a list of CME events, the same as the previously described CDAW catalogue. The only difference is CACTus doesn't require any human intervention, and hence, CME detection can be done on real-time data immediately.

2.6.4 DONKI

The Database Of Notifications, Knowledge, Information (DONKI)[5] catalogue is managed by NASA's SWPC, which acts as a centralised resource for monitoring and analysing space weather events, especially focusing on CMEs and their linked solar and interplanetary phenomena. As a real-time space weather notification system, DONKI provides in-depth analysis and forecasts of space weather events. While it tracks a variety of solar activity, its primary focus is on CMEs. It offers a comprehensive, publicly accessible record of solar activity, allowing scientists to follow CME events from their solar origin to their potential impacts on Earth and other solar system planets.

---

[5] Link to DONKI: https://ccmc.gsfc.nasa.gov/tools/DONKI/

DONKI provides several parameters that are critical for understanding the nature of space weather events. It provides an exact time of the first detection of a CME using LASCO, STEREO or SDO images. Additionally, it often includes crucial information about the associated source region, which is crucial information to understand the triggering mechanism and estimate the propagation direction of a CME. Furthermore, it provides detailed information on CME kinematics and morphology, including angular widths, expansion rate, CME speed, propagation angle and many more. DONKI stands out in terms of its data products by providing CME impact predictions such as predicted arrival time at Earth, expected geo-effectiveness, Kp index and associated phenomena. This functionality allows scientists, students, model developers and global partners to access information stored in DONKI via comprehensive API web services. The API service returns the following key quantities: unique CME id, time at 21.5 $R_\odot$, latitude, longitude, half angle, speed at 21.5 $R_\odot$, CME detection instrument, specific note for each events. Additionally, it offers a link for Wang-Sheeley-Arge (WSA)-ENLIL simulation results.

DONKI has made significant contributions to space weather research and forecasting. Its operational use transforms it into an online tool for the space weather community and industries to monitor space weather.

2.7 ICME databases

The space era brings vast in-situ solar wind data from different spacecraft. This huge amount of data has opened a gate for the creation of multiple ICME catalogues. However, compilation and maintenance of these datasets involve several challenges due to incomplete observations, data fragmentation and inconsistency, different criteria for ICME identification, difficulties in ICME identification because of multiple interactions or structures and many more. Despite these obstacles, the extensive in-situ data acquired from many spacecraft has significantly improved our understanding of ICMEs. Various studies have been performed to investigate ICME morphology and compositions using in-situ data from multiple spacecraft. These studies resulted in different datasets or catalogues.

2.7.1 Richardson and Cane

The “Near-Earth Interplanetary Coronal Mass Ejection Since January 1996”, popularly known as ’Richardson and Cane ICME list’[6] is one of the most robust list of ICME properties measured at L1 point. Spanning from 1996 to the end of 2023, this catalogue has recorded close to 400 ICME events. This catalogue considers solar wind composition and ion charge state observations for ICME identification and provides detailed information on various properties of ICME, starting with an observed time of ICME related disturbance [Cane and Richardson, 2003, Richardson and Cane, 2010]. In the case of fast CMEs, ICME induced shock arrival time is considered. Following this, ICME start and end time are inferred from plasma and magnetic field data. Additionally, the catalogue provides the start and end times of abnormal solar wind composition and magnetic clouds. Once ICME timings are derived, plasma and magnetic field time series data are analyzed to provide indicative measures of bidirectional suprathermal electrons and ions. This measure helps to determine ICME associated SEP events. From the same time series data, mean ICME speed and mean magnetic field strength are obtained. It also feeds the information regarding the presence of magnetic cloud-like structure in ICME and its geo-effectiveness through the Dst index. In this catalogue, efforts have been made to associate each ICME observation with the probable CME observed by SOHO or STEREO. (Refer Cane and Richardson [2003] and Richardson and Cane [2010] for the brief discussion on ICME identification method and primary datasource for this catalogue)

2.7.2 WIND ICME list

Another important catalogue of ICME is “Wind ICME Catalogue”[7]. This catalogue is compiled using the 20 years of Wind observations of interplanetary transients at 1AU to understand and develop an analytical model for the internal magnetic field of ICMEs. It provides ICME start and end times, the presence of an interplanetary shock, and start and end times of magnetic obstacles. Apart from this, necessary plasma and magnetic field measurements

---

[6] Link for Richardson and Cane (R&C) ICME list: `https://izw1.caltech.edu/ACE/ASC/DATA/level3/icmetable2.htm`

[7] Link to Wind ICME catalogue: `https://wind.nasa.gov/ICME_catalog/ICME_catalog_viewer.php`

are provided along with magnetic obstacle type information such as flux-rope, complex or ejecta [Nieves-Chinchilla et al., 2018]. This catalogue is a one-stop source for the ICME magnetic properties of solar cycle 23 and contains a total of 337 ICMEs events from 1995 to 2015.

2.7.3 GMU CME/ICME list

Another relevant dataset in this domain is "GMU CME/ICME List"[8]. It is one of the data products of George Mason University Space Weather Lab. It is a complete list of CME-ICME information from November 2007 to September 2017. This catalogue stands out in terms of the information it provides. This catalogue contains ICME start and end times derived from in-situ data of ACE spacecraft, along with a timestamp of the first appearance of CME in LASCO-C2 or STEREO-COR2 FOV. Additionally, it provides ICME type information similar to the Wind catalogue mentioned in Section 2.7.2. One of the key features of this catalogue is information on active regions and solar flares associated with the CME making it quite useful for the study of CME-Flare relationship. For the comparative study of CME speed, it provides CME speed recorded in SEEDS catalogue for LASCO-C2 and STEREO-A/B COR-2 instruments average velocity using in-situ data of ACE. It also provides a link to the LASCO-C2, STEREO-COR2, SOHO/EIT and SDO/AIA images for CME observations, along with in-situ data for the ICME measurements. The under-progress upgrade of this catalogue is ICME-CME-Solar Surface Source (SSS) catalogue[9], which is a comprehensive list of cause-effect of solar eruptive events from Sun to Earth.

2.7.4 Helio4cast ICME catalog

Helio4cast ICME catalogue, commonly known as ICMECAT[10] is a collective list of in-situ magnetic field and bulk plasma observations of ICME in the heliosphere. The initial version of this catalogue is an outcome of HELCATS project and it uses in-situ data from many spacecrafts, such as: Wind, STEREO-A/B, Venus Express (VEX), MErcury Surface, Space ENvironment,

---

[8] Link to GMU CME/ICME List: `http://solar.gmu.edu/heliophysics/index.php/GMU_CME/ICME_List`

[9] Line for the CME-ICME-SSS Catalogue: `http://solar.gmu.edu/heliophysics/index.php/ICME-CME-SSS_catalog`

[10] Link to Helio4cast ICME catalogue: `https://www.helioforecast.space/icmecat`

GEochemistry and Ranging (MESSENGER), ACE, BepiColombo, SolO, PSP, Juno, Mars Atmosphere and Volatile EvolutioN (MAVEN), Mars Science Laboratory (MSL), Ulysses [Möstl et al., 2017]. This catalogue provides ICME start time, magnetic obstacle start-end time, along with plasma and magnetic properties of both ICME and magnetic obstacle.

The list of CME and ICME catalogues mentioned in this thesis are just a few examples of publicly available datasets that are relevant to the work discussed in this thesis. Many other catalogues do exist. One of the noteworthy examples is the data product of HELCATS[11] project, where various datasets have been prepared using STEREO/HI observations.

---

[11] Link to Helcats Project data products: `https://www.helcats-fp7.eu/index.html`

Chapter 3

Coronal Mass Ejection: Propagation and Forecasting

This chapter provides a brief introduction to the Drag-Based Model (DBM) and its different variants (e.g., P-DBM). This chapter begins with a brief overview of various CME propagation frameworks and reported accuracy of the models to justify the focus on DBM Following this, DBM is discussed comprehensively, including the limitations, extension to the 2D approach, and ensemble formalism. Subsequent parts of the chapter are based on the publication Mugatwala et al. [2024]. These parts address the problems in implementing P-DBM for operational usage and the proposed solution to overcome them. The remaining part begins with an overview of geo-effective CME-ICME properties and covers the detailed explanation of the methodology used to refine this dataset. The chapter ends with a brief discussion on the obtained results, including PDFs associated to w and γ parameter and relabelling scheme for solar wind speed.

3.1 Introduction

Due to the profound impact of CMEs on space weather and the technological infrastructure of mankind, the study of CMEs has gained significant scientific attention. Accurately forecasting the arrival time of CMEs and their properties at Earth remains a crucial objective of numerous federal agencies, including NASA, NOAA, ESA, Austrian Space Weather Office (ASWO), UK Met Office and many more. Under various scientific projects, namely Community Coordinated Modeling Center (CCMC) CME Arrival Time Scoreboard[1], International Space Weather Initiative (ISWI)[2], International Space

---

[1] CCMC CME Scoreboard: `https://kauai.ccmc.gsfc.nasa.gov/CMEscoreboard/`

[2] `https://www.unoosa.org/oosa/sk/ourwork/psa/bssi/iswi.html`

Weather Action Teams (ISWAT)[3] researchers and scientists made efforts to predict CMEs properties as they arrived at Earth. These efforts resulted in the numerous CME propagation models. In 2018, CCMC CME Scoreboard had registered 32 distinct models to perform CME arrival time prediction [Riley et al., 2018].

Initially, CME propagation models were divided into two primary classes: (1) Empirical methods and (2) magneto-hydrodynamic (MHD) based models. Due to developments in Artificial Intelligence (AI) and Machine Learning (ML), a totally new set of models also emerged in the last decade. Additionally, between the empirical and MHD methods, there exists an intermediate approach where MHD-Hydrodynamics (HD) based analytical kinematic calculations are used for CME propagation. Then later on, ensemble frameworks are also developed for these forecasting models. Each class offers various benefits and drawbacks, which are outlined as follows:.

- **Empirical Models**:
  In this class, models exploit the statistical relationships established from historical CME observations. Empirical CME Arrival (ECA) [Gopalswamy et al., 2000, 2001], Effective Acceleration Model (EAM) [Paouris and Mavromichalaki, 2017, Paouris et al., 2021a], Ellipse Evolution (ELEvo) [Möstl et al., 2015] are some of the popular empirical models. Models from this class are computationally inexpensive but usually unreliabel due to their generalised assumptions.

- **Physics-based MHD Models**:
  This kind of model simulates CME propagation, in which a complete set of MHD equations governing heliospheric plasma dynamics are solved. Contrast to emperical models, these models require extensive computational power but provide a physically more realistic representation of CME evolution. WSA-ENLIL+Cone model [Odstrcil et al., 2004], EUropean Heliospheric FORecasting Information Asset (EUHFORIA) [Pomoell and Poedts, 2018, Poedts et al., 2020], Space Weather Adaptive SimulaTion (SWASTi) [Mayank et al., 2022] are some leading models from this class.

---

[3] `https://iswat-cospar.org/`

- **Machine Learning Models**:
  Machine learning models utilise large datasets to learn complex patterns and relationships in order to enhance CME prediction accuracy. Models of the class come with inseparable drawbacks of machine learning itself; many models work as "black boxes," making it difficult to interpret. Additionally, ML models require large, high-quality datasets, but incomplete observational data limit the availability of comprehensive training datasets. Sudar et al. [2016], Liu et al. [2018] are initial attempts to introduce ML methods to predict CME arrival time.

The performance of these space weather forecasting models plays a crucial role in their effective implementation in operational usage. The space weather research community has made numerous efforts to assess the accuracy, reliability, and scope for advancement of these models [Zhao and Dryer, 2014, Riley et al., 2018, Vourlidas et al., 2019, Verbeke et al., 2019, Temmer et al., 2023]. A comprehensive study by Riley et al. [2018], which analysed all the forecasts submitted to CCMC CME scoreboard between years 2013 and 2018, suggests that Mean Absolute Error (MAE) of DBM is 8.27 hrs, making it comparable to other models [See Table-3 of Riley et al., 2018]. Similarly, Vourlidas et al. [2019] found that MAE for DBM is 11.54 hrs using different CME samples [See Table-1 of Vourlidas et al., 2019]. The comparable accuracy among the models is due to uncertanities in CME input parameters [Paouris et al., 2021b, Brinkman et al., 2021]. The current limitations in CME observations, simplicity, and inexpensive computational cost of semi-empirical models make them a very popular choice among the space weather researcher community. Therefore, in this thesis a widely popular kinetic model called Drag Based Model (DBM) (Section-3.2) with probabilistic approach (Section-3.4) is studied extensively.

3.2 Drag Based Model

3.2.1 Model Description

The Drag Based Model (DBM) operates on the assumption that the dynamics of ICMEs is primarily governed by the "aerodynamic" simplification of the MHD drag [Vršnak et al., 2013]. This rather strong assumption is nevertheless supported by numerous studies [Cargill et al., 1996, Cargill, 2004, Vršnak, 2001, Vršnak et al., 2010, Owens and Cargill, 2004, Lara and Borgazzi, 2009]. Observations indicate that CMEs have a tendency to achieve ambient solar wind speed during the propagation, i.e., CMEs that are faster than background solar wind speed decelerate, whereas CMEs those are slower than background solar wind speed accelerate during the propagation [Gopalswamy, 2009]. This is similar to the viscous force experienced by a body as it traverses through a liquid. The acceleration of a CME due to drag in quadratic form is given as:

$$a(r)_{CME} = -\gamma\Big(v(r)_{CME} - w\Big) \mid v(r)_{CME} - w \mid \tag{3.1}$$

Where $a(r)_{CME}$ and $v(r)_{CME}$ are the instantaneous acceleration and speed of the CME, respectively, w is the instantaneous ambient solar wind speed, and γ is the drag parameter quantified measure of drag efficiency. It is crucial to recognise that all the quantities in Equation 3.1 are space (r) and time (t) dependent. The drag parameter γ measures the rate of change in velocity, indicating the degree to which the CME speed changes per unit distance. In other words, it denotes the strength of the interaction between CME and ambient solar wind. The mathematical expression for γ is

$$\gamma = C_d \frac{A_{CME}\, \rho_{sw}}{M + M_v} = C_d \frac{A_{CME}\, m_p\, n_{sw}}{M + M_v} \tag{3.2}$$

Here, C_d represents the dimensionless drag coefficient, which is typically of the order of unity [Cargill, 2004], and the terms A_{CME} and ρ_{SW} represent the CME cross-sectional area and solar wind density, respectively; M denotes the mass of the CME, m_p represents proton mass, and n_{sw} refers to the proton number density of solar wind. Additionally, the term M_v represents an additional virtual mass of the CME (due to the pile-up of Solar Wind (SW) plasma) and can be approximated as $\sim \frac{\rho_{sw} V}{2}$. The CME mass can be further explicated as $M = \rho_{CME} V$, where V is CME volume. When the thickness of CME L is introduced, Equation 3.2 is transformed into:

$$\gamma = \frac{C_d}{L(\frac{\rho_{ICME}}{\rho_{sw}} + \frac{1}{2})} \tag{3.3}$$

The Equation 3.3 has two obvious cases:

Case-I: $\rho_{sw} \gg \rho_{CME} \Rightarrow \gamma = \frac{2C_d}{L} \implies \gamma$ is independent of solar wind density.

Case-II: $\rho_{CME} \gg \rho_{sw} \Rightarrow \gamma = \dfrac{C_d\,\rho_{sw}}{L\,\rho_{CME}} \implies$ the virtual mass is negligible and γ is significantly lower compared to Case-I. As a result, massive ICMEs that have a much higher density than ambient solar wind are less affected by the drag.

Observational studies of ICME propagations suggest that Case-II represents a more realistic scenario. Under this regime with few additional approximations, such as, $\dfrac{\rho_{ICME}}{\rho_{sw}} \sim 10$, L $\sim 1R_\odot$ and $C_d = 1$ leads to $\gamma \sim 10^{-7}$ km^{-1}. (Refer to section 3.4 of Sachdeva [2018] for a very detailed description and calculation of the parameters mentioned in Equation 3.2, 3.3.)

For the simplified version of the model, the following approximations are valid at sufficiently large distances (typically, larger than $20R_\odot$): $A \propto r^2$ (due to "self-similar" expansion and supported by the fact), $\rho_{sw} \propto \dfrac{1}{r^2}$ (as in the empirical solar wind density model Leblanc et al. [1998]), M = constant, C_d = constant. Furthermore, inder the condition $\rho_{CME} \gg \rho_{sw}$, the drag parameter γ is considered constant (but see Vršnak and Gopalswamy [2002] for $\gamma \neq$ constant scenario). Additionally, isotropic solar wind flow condition implies that w = constant, which aligns with various empirical solar wind speed models [Vršnak and Žic, 2007, Sheeley et al., 1997, Leblanc et al., 1998]. The analytical solution of Equation 3.1 with the aforementioned approximations is given by:

$$v(t) = \frac{v_0 - w}{1 \pm \gamma(v_0 - w)t} + w, \tag{3.4}$$

$$r(t) = \pm\frac{1}{\gamma}\ln(1 \pm \gamma(v_0 - w)t) + wt + r_0, \tag{3.5}$$

Where $v(t)$ and $r(t)$ are the ICME speed and heliocentric distance respectively at time t. The parameter r_0 is the initial position of CME (which, by the assumptions, must be larger than 20 $R_\odot$), and v_0 denotes the initial speed of the CME at r_0. The ± sign depends on the deceleration/acceleration regime. From Equations 3.5 and 3.4, one can determine the "Transit-time" (T) and "Impact Speed" (v_1) of ICME at any chosen heliocentric distance. A detailed derivation of the Equation 3.5 and 3.4 is provided in Appendix A.1. The numerical outcome of the case when $w \neq$ constant and $\gamma \neq$ constant are also compared, and those numerical results show a minor difference with respect to the case described here above: calculated transit times from both cases differ by less than 1 hr.

Figure 3.0 shows several examples of the ICME kinematics calculated using the analytical solution of DBM provided by Equations 3.5 and 3.4. The full lines represent the kinematics of fast ICME cases for various values of γ and w, considering initial take-off speed $v_0 = 1000km/s$. Whereas the dashed lines correspond to the slow ICMEs cases where the initial speed is $v_0 = 200km/s$. The heliocentric distance as a function of time is illustrated in Figure 3.0(c). The x intercept defines the ICME transit time. For reference, the intercept that corresponds to r=214 $R_\odot$) provides the ICME fly time corresponding to 1 AU. Figure 3.0(a) represents the ICME speed versus heliocentric distance. The ICME transit speed at any heliocentric distance is obtained by taking the y-coordinate of the kinematic curve. Finally, in Figure 3.0(e) and 3.0(f) the ICME acceleration is presented as a function of heliocentric distance and time, respectively.

The plots in Figure 3.0(a) clearly indicate the tendency of ICMEs to achieve ambient solar wind speed under the DBM assumption. As expected, the speed adjustment is much faster in the high γ condition (represented by the red solid line and brown dashed line). Additionally, Figure 3.0(c) implies that a very fast ICME travelling through the fast solar wind may have a shorter transit time in a low γ regime (blue solid line). On the contrary, slow ICME travelling with slow solar wind under low γ regime takes longer travel time (purple dashed line). Lastly, 3.0(e) shows that the larger part of the acceleration/deceleration happens close to the Sun, typically before 50 $R_\odot$.

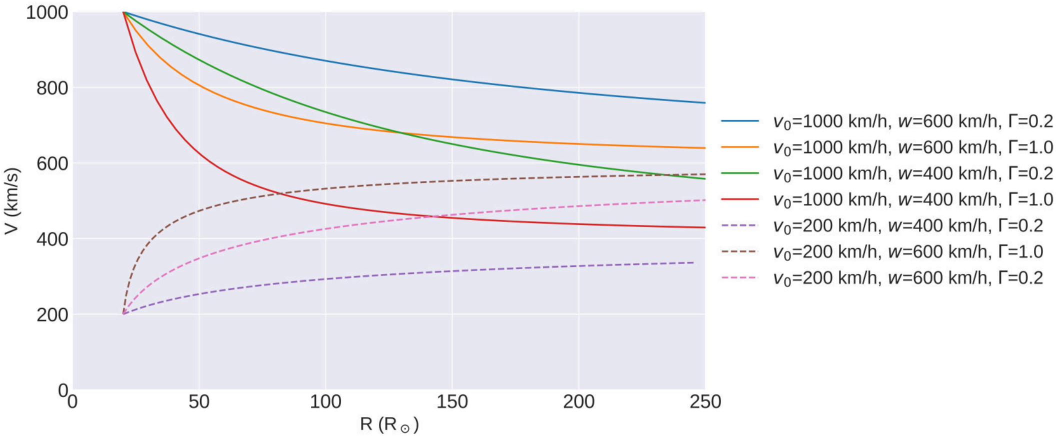

(a)

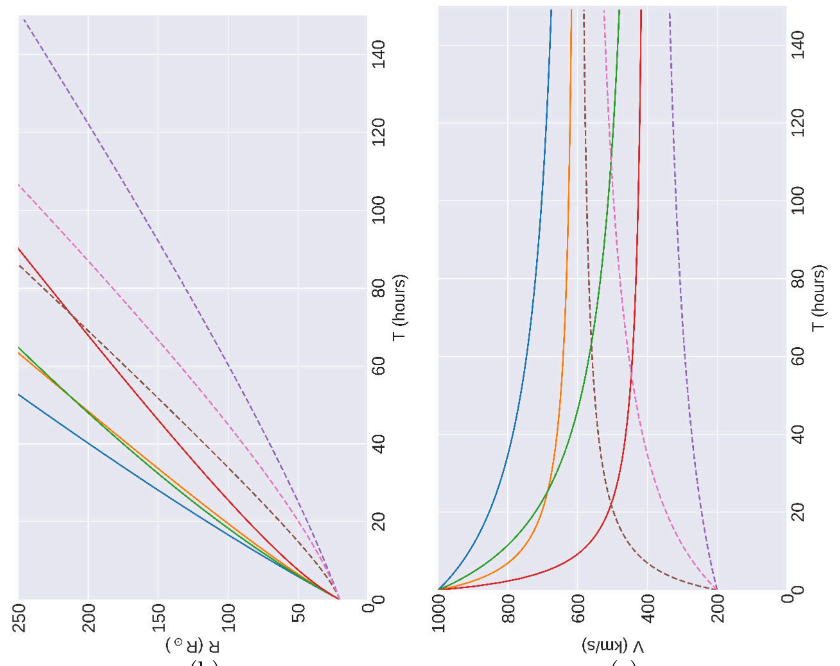

(b) (c)

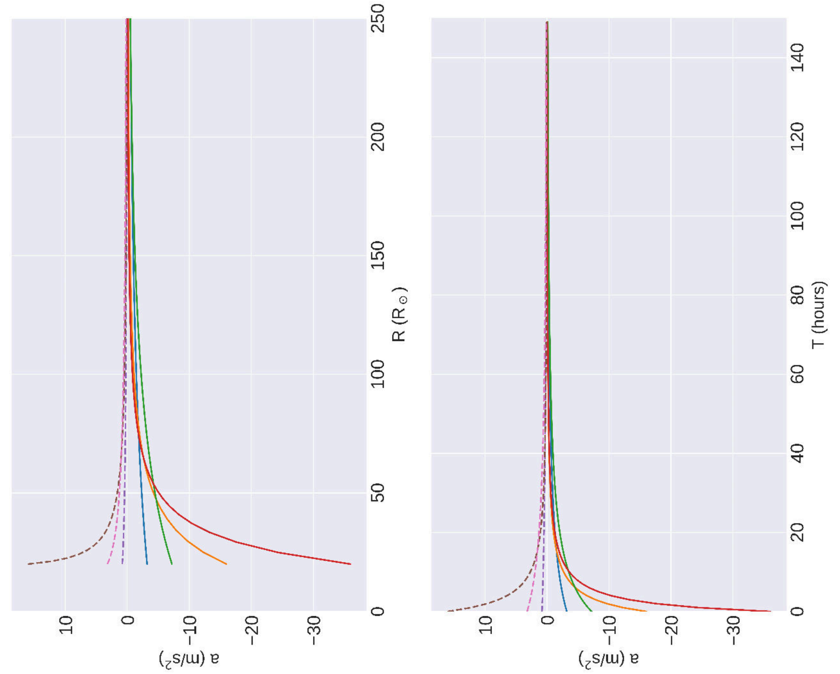

(d) (e)

Figure 3.0: Examples of ICME kinematics under DBM approximation. The initial heliocentric distance of ICME is set to r_0=$20R_\odot$. (a) ICME speed versus heliocentric distance. (b) ICME heliocentric position versus fly time. (c) ICME speed versus fly time. (d) DBM acceleration as a function of heliocentric distance. (e) DBM acceleration versus time The kinematic model parameters are shown in legend. Here Γ is a dimensionless abbreviation defined as $\gamma = \Gamma \times 10^{-7}\text{km}^{-1}$

3.2.2 Limitation of the DBM

The DBM treats the ICME propagation as a momentum exchange between the ICME and the ambient solar wind, subject to various assumptions. These assumptions led to the three major drawbacks of the model.

1. **Constant** γ:
   Approximations such as the $\frac{1}{r^2}$ decrease in ambient solar wind density, an effective cross-sectional area of ICME increase as $A \propto r^2$, and a constant ICME mass collectively resulted in a constant value of γ. Instead, the statistical analysis of the Helios, Voyager, and Pioneer data suggests that the cross-sectional area of ICME increases as $A \propto r^{1.6}$ and the proton density decreases as $\frac{1}{r^{2.4}}$ [Bothmer and Schwenn, 1997, Vršnak et al., 2013]. Additionally, C_d is likely not constant over the considered heliocentric distance range. Therefore, the constant γ might not be an appropriate approximation, and this affects the accuracy of the arrival-time and speed predictions [Cargill, 2004, Vršnak et al., 2010, 2013].

2. **Simple solar wind structure:**
   The DBM considers that the ICME is entirely embedded in an isotropic flow where the speed remains the same everywhere. However, the ICME can encounter changes in the ambient solar wind during propagation due to various reasons, such as an ICME entering a fast solar wind stream, a fast ICME catching up a previous slow ICME travelling in the same direction and interacting with it ... [Temmer et al., 2011, Temmer et al., 2012]. Also, the vast spatial extent of most ICMEs can probably lead to the interaction of the ICME with high-speed streams originating from polar coronal holes [Odstrcil et al., 2004].

3. **Drag term consideration only:**
   A major inseparable drawback of this model is that it considers only a drag term in the equation of motion by assuming Lorentz force does not act anymore in the upper corona. This is not true for every case; many fast ICMEs significantly accelerate beyond 20 $R_\odot$. This leads to wrong predictions [Vršnak et al., 2004]. Also, the inner boundary where Lorentz force and gravity become negligible compared to the drag force

varies from event to event [Sachdeva et al., 2015, Sachdeva, 2018]. This can be avoided by employing ICME kinematics measurements based on STEREO observations.

3.3 Advance Drag Based Model

The DBM analysis mentioned in Section 3.2 is a rather primitive approach that does not take into account the geometry of ICMEs. In Section 3.2, only a single ICME point (usually the apex of the ICME) is considered for propagation. However, the advanced version of the model incorporates the shape of ICME, enabling the model to provide information on whether or not a specific target will be impacted by ICME. This improved version of the DBM implements a 2D cone geometry by considering the CME angular span and its propagation direction. Observations fairly justify the choice of a cone geometry, and it is used in a wide range of heliospheric models such as ENLIL [Odstrcil et al., 2004] or EUHFORIA [Pomoell and Poedts, 2018, Poedts et al., 2020]. Therefore, the same inputs can also be applied in the DBM. Figure A.1 represents three standard cone geometries, and their detailed description is provided in Appendix A.2. In Figure 3.1, the distance ratio $\frac{R_\alpha}{R_0}$ is visualised as a function of angle α for various ICME half-width ω. A similar plot applies for the speed ratio $\frac{V_\alpha}{V_0}$. It is important to note that α ranges from $0 \leq \alpha \leq \omega$, where $\alpha = 0$ corresponds to the ICME apex and $\alpha = \omega$ is for the lateral edge of ICME. This geometrical consideration also introduces two different types of kinematic approaches in the CME propagation, namely self-similar expansion and flattening cone evolution.

- **Self-similar Expansion**: In this approach, CME maintains its shape during propagation. The DBM Equation 3.5 has been solved for the apex point, and then the geometrical transformations are applied to determine the kinetic properties of other points on the ICME leading edge.

- **Flattening cone evolution**: Here, the geometrical transformation is used before applying the DBM equation to each point of the ICME leading edge. This approach is more realistic compared to the previous one. Hence, we employ this approach in our model application and evaluation.

Figure 3.2 represents the differences in kinematics for self-similar expansion and flattening cone evolution approaches. The kinematic calculations were performed for ICME half angular width $\omega = 30°$, drag parameter Γ =0.2, Solar wind speed w= 400 km/s (Γ is a dimensionless quantity defined as $\gamma = \Gamma \times 10^{-7} Km^{-1}$). The initial conditions for ICME were set to R_{0i}= 20 $R_\odot$ and v_{0i} =1000 km/s. The figure shows the kinematics for the different segments of the ICME leading edge. The red curve corresponds to the ICME apex point, while the blue, orange, and green curves represent the ICME leading edge segments located at the 10°, 20°, and 30° respectively. Figure 3.2(a) clearly shows that the gradient $\frac{dv}{dR}$ is consistent across all radial distances, whereas in Figure 3.2(b) kinematics curves are converging towards a single point. It is evident that beyond a certain heliocentric distance, all the points on ICME leading edge are travelling with the same speed during the flattening cone evolution.

3.4 Ensemble Frameworks for DBM

The performance of any CME propagation model is heavily dependent on the observation-based inputs describing their properties. These inputs, which typically include parameters such as CME speed, direction, and angular width, are essential for achieving a good accuracy of the model's predictions. However, significant uncertainties often compromise the accuracy of the observations themselves. These uncertainties originate from several reasons, such as instrument errors, projection effects, and other observational restrictions, including uncertainty in the line of sight. It then becomes difficult to create extremely accurate propagation models because of these inherent errors in the CME observations. Consequently, ensemble forecasting techniques have been widely used to account for these errors and uncertainties in the input data. A similar approach has been applied by the WSA-ENLIL+cone model to study the sensitivity to the initial CME inputs and provide probabilistic forecasts [Mays et al., 2015]. The primary focus of this thesis is on the implementation of a probabilistic approach in DBM. In literature, two different kinds of formalism exist for DBM ensembles, namely Drag Based Ensemble Model (DBEM) and P-DBM.

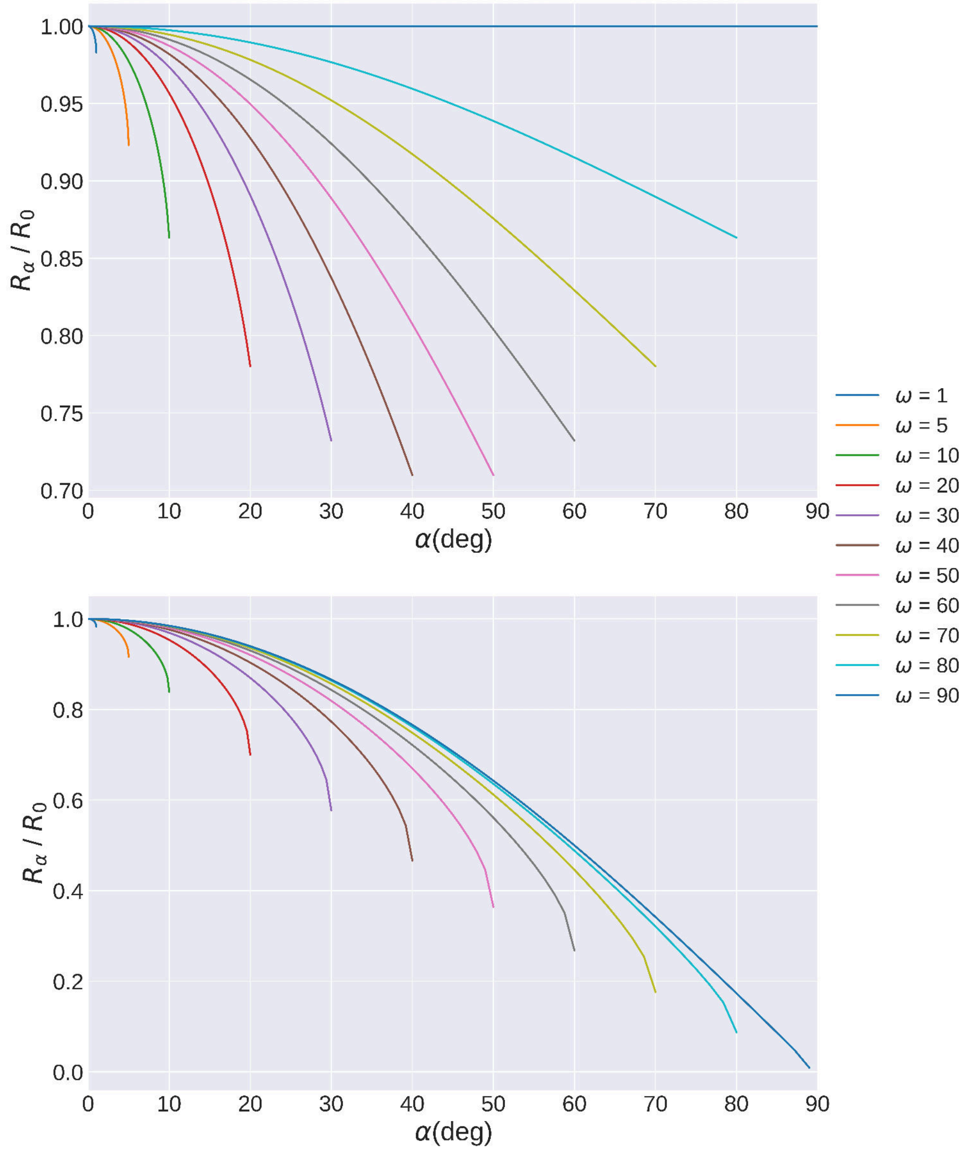

Figure 3.1: The ratio of the heliocentric distance of the ICME leading edge element positioned at the angle α to the distance of its apex, expressed as a function of α for different cone half-widths ω. Top: Ice-cream Cone, Bottom: Tangential Cone

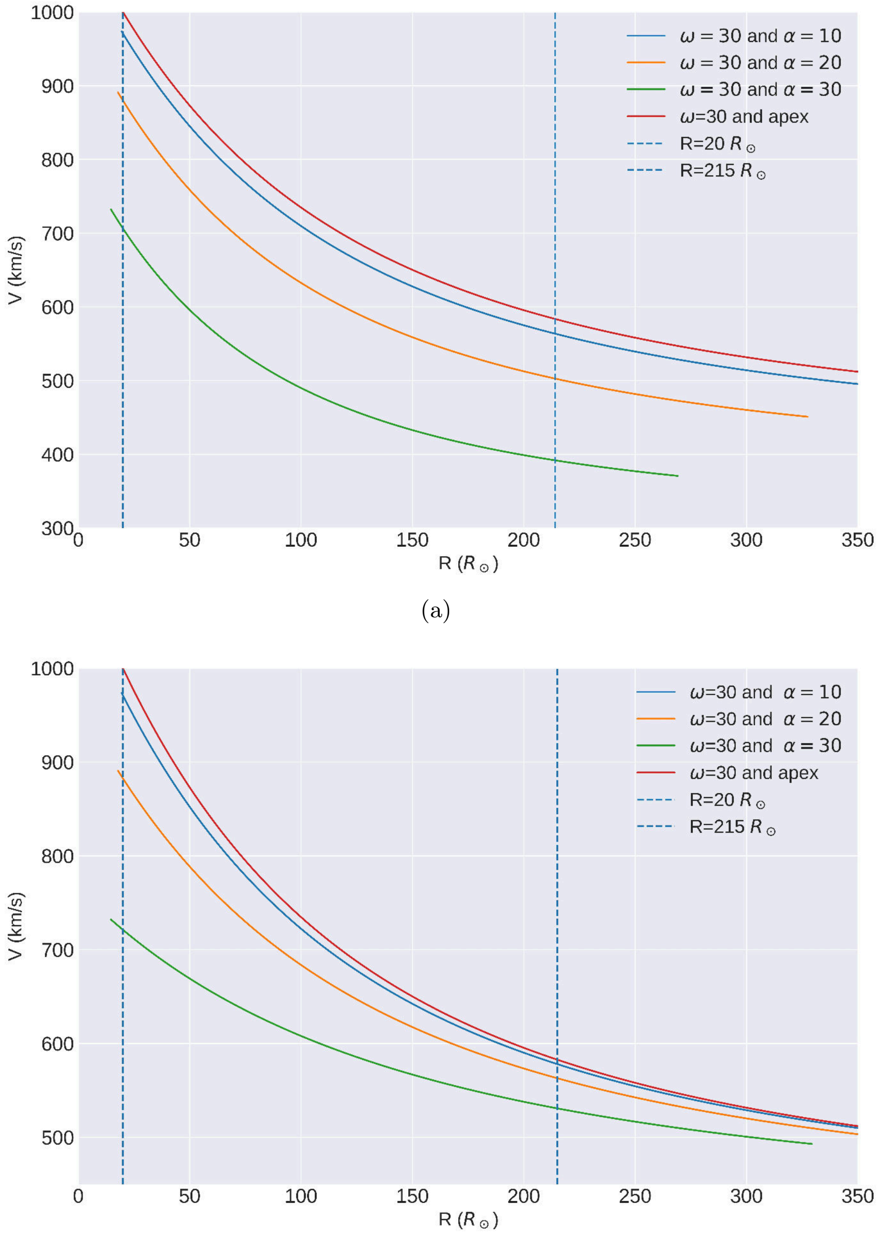

Figure 3.2: The kinematics calculation for ICME with initial speed $v_0 = 1000 km/s$ and model parameters are $w = 400 km/s$ and $\Gamma = 0.2$. (a) Self-similar expansion ICME kinematics. (b) Flattening cone evolution ICME kinematics.

3.4.1 Drag Based Ensemble Model

The DBEM is based on the DBM, which considers an ice cream cone geometry with flattening cone evolution [Dumbović et al., 2018]. The CME properties, such as speed, half-width, and propagation direction, are derived from the observations and used as DBEM input. In DBEM, the leading edge height of each CME is measured at two different times in two different coronagraphs multiple times to produce n ensemble measurements. The DBEM assumes that both w and γ follow the normal distributions, with $w = (350 \pm 50)\ km/s$ for the solar wind and $\gamma = (0.1 \pm 0.05) \times 10^{-7}\ km^{-1}$ for the drag parameter, using the empirical values derived in Vršnak et al. [2013, 2014]. Using these PDFs, m synthetic values of both parameters are produced. The synthetic values of the model parameters and an ensemble of CME's measurements give a final $n \times m^2$ input condition, which produces a distribution of $n \times m^2$ computed CME transit times and impact speeds. The value of m is valuable input for the DBEM as it affects the variability of transit time and speed; a larger value of m will decrease this variability but increase the computing cost. Analysis in Dumbović et al. [2018] suggest that for an ensemble with $n = 48$, an optimal value of $m = 15$. The total number of DBEM runs $n \times m^2 = 10800$ takes several minutes on an average computer, with a variation of 5% on the estimated transit time and 10% on the estimated impact speed. One of the most significant outputs of this model is the "probability of arrival", defined as $p = \frac{n_{hits}}{n_{total}}$. In this context, n_{hits} is the number of ensembles that are calculated to hit the target by implementing the $\omega \geq |\phi|$ condition, where ω is CME half width and ϕ denotes the CME source position.

For the operational forecast, the DBEM requires six synthetic measure values, including the CME launch time, speed, angular width, propagation direction, and the DBM w and γ parameters. If m is set to 9, then almost 530000 DBEM runs are performed to produce reliable results, but it takes more computer power and time for calculation. To overcome this issue, an upgrade is made to DBEM by adopting a random value generation from the normally distributed PDFs to produce an ensemble rather than making synthetic observations. In this way, DBEMv2 (version) converges to stable results much faster, enabling one to have a lower number of runs. Another great benefit is a selection of an exact number of DBEM runs, as it does not depend on a number of synthetic measurements. A study done by Čalogović et al. [2021] suggests that even for 10000 DBEM runs, results are almost fully converged. Later on, another upgrade DBEMv25 (version 2.5) was made by incorporating proper motion of a target in calculation and parallelisation of DBEM python code. The new version DBEMv3 (version 3) DBM results and CME propagation are included along with Graduated Cylindrical Shell (GCS) model for CME geometry [Thernisien et al., 2006, 2009, Thernisien, 2011].

Refer to Čalogović et al. [2021] for the detailed description of different DBEM formalism. See Table-1 of Dumbović et al. [2021], which provides a comparison of five currently available DBM versions, namely: (1) basic 1D DBM; (2) advanced DBM with 2D self-similar cone; (3) 2D flattening cone DBM; (4) DBEM; (5) DBEMv3. Table 2 of Dumbović et al. [2021] demonstrates the comparative results of various DBM results for the CME event that started on 3^{rd} April 2010 and hit the Earth on 5^{th} April 2010.

3.4.2 Probabilistic Drag Based Model

Similarly, Napoletano et al. [2018] consider a Gaussian PDF for the CME measured quantities and assume a priori PDFs for both model parameters w and γ. This consideration can enable the implementation of the probabilistic approach for DBM, called Probabilistic Drag Based Model (P-DBM). P-DBM essentially involves a Monte Carlo simulation for the Time of Arrival (TOA) and impact speed of ICMEs at a specified distance from the Sun, converting the input PDFs linked to the model into PDFs for both outputs: transit time and impact speed, providing best estimates and associated uncertainties. For each ICME, N different initial conditions $[r_0, v_0, w, \gamma]$ are generated from the assumed PDFs to compute N transit times and velocities using Equations 3.5 and 3.4. Figure 3.3 illustrates the kinematics of ICME for three different cases obtained using the P-DBM with $N = 1000$. It is worth mentioning that, even though initial conditions are generated from the Gaussian distribution function, the P-DBM output is not symmetric. The reliability of the results depends primarily on the realism of these PDFs and the extent of parameter space exploration, i.e., how large is N. Given the current computational resources and the simplicity of DBM Equations 3.5 and 3.4, N ranging from 10^4 to 10^6 can be used to effectively explore the parameter space, with the resulting output PDFs being computed efficiently in seconds. As an example, Figure 3.4 shows the distribution of transit time (TT) and arrival speed ($V_{arrival}$)

computed using P-DBM. As a result of different input PDF, CME fly time varies between 40 to 80 hrs, while the arrival velocity ranges from 400 to 800 km/s. This thesis primarily focuses on the P-DBM framework for all the following calculations and analyses.

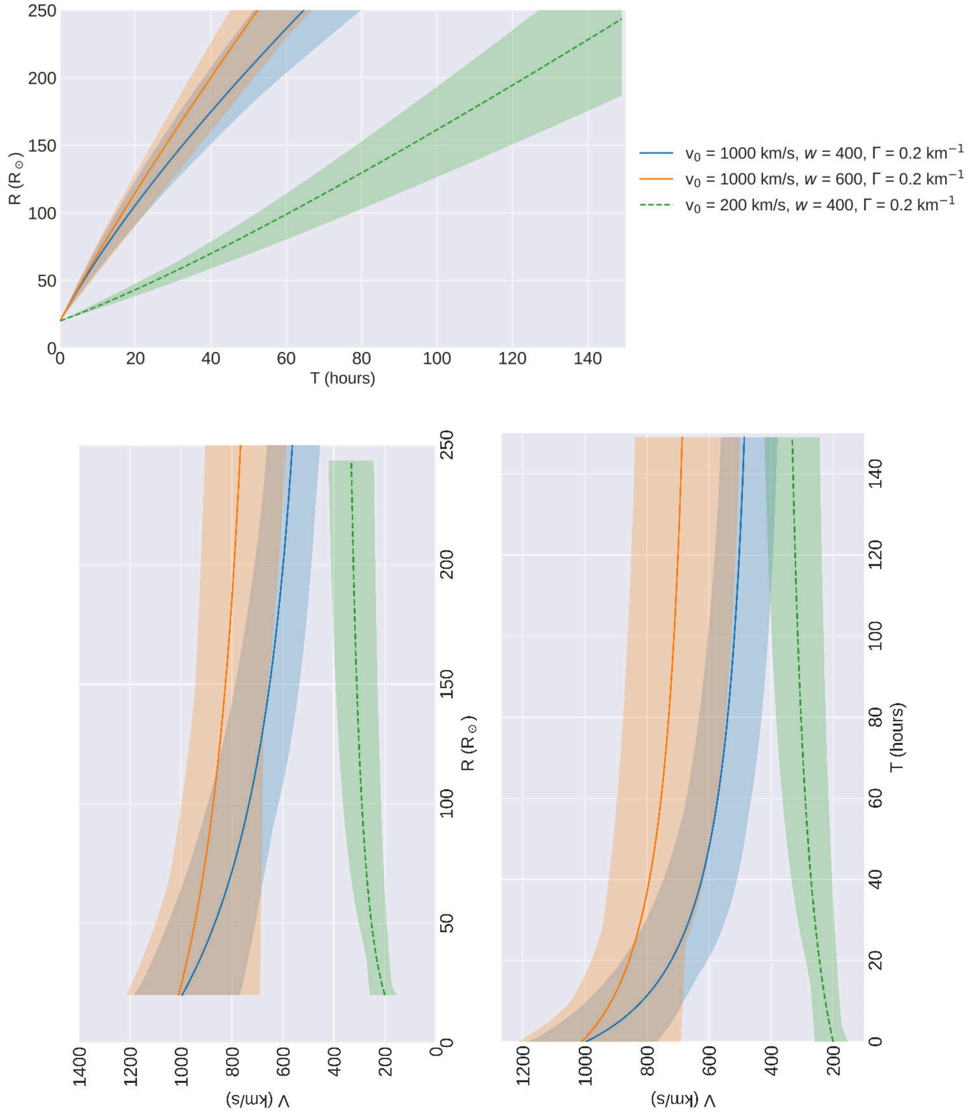

Figure 3.3: Example of ICME calculated using P-DBM approach. The initial conditions are generated using Gaussian distribution functions, whose mean values are provided in the legend, and 10% variation is taken as a standard deviation. A solid line denotes the mean value of the quantity, while a shaded area represents the associated uncertainties.

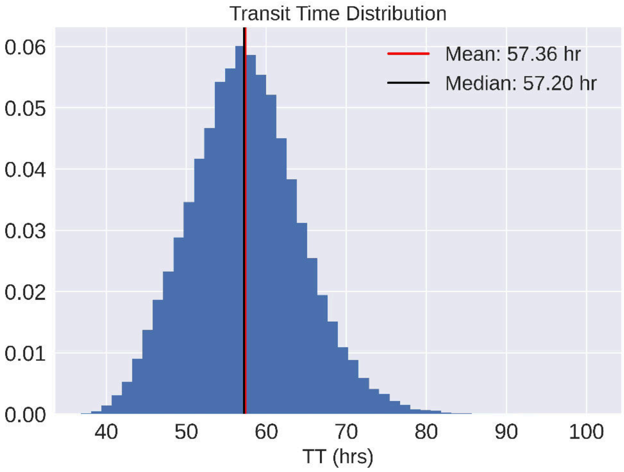

(a)

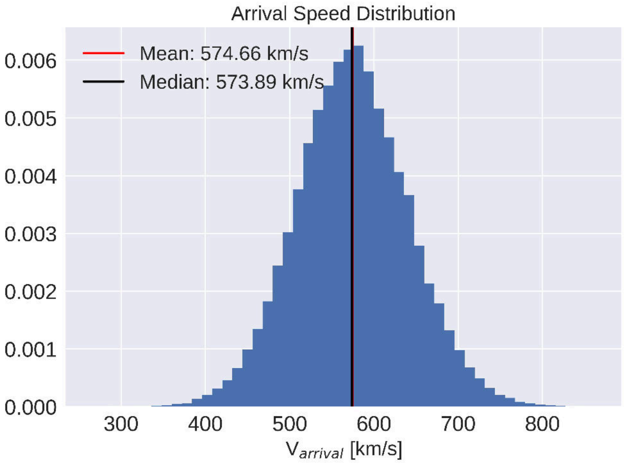

(b)

Figure 3.4: P-DBM output with N=50000 initial conditions for the event-7 studied in Čalogović et al. [2021] (See Table-1 of the article). (a) Distribution of the transit time. (b) Distribution of the arrival speed.

3.5 Parameter Estimation for Drag-Based Modelling

The ICME position and speed in the heliosphere at a specific time using DBM Equations 3.5 and 3.4 and suitable model inputs. The initial position r_0 and initial speed v_0 of ICME can be obtained from the coronagraphic observations, but the free parameters of the model, i.e., solar wind speed w and drag parameter γ are usually unknown. Therefore, Equation 3.1 can not be helpful for operational forecasting. This limitation makes it necessary to determine the possible value range of the w and γ parameters. In this direction, various studies have been conducted in recent years [Napoletano et al., 2018, 2022, Kay et al., 2020, Čalogović et al., 2021, Mugatwala et al., 2024, Chierichini et al., 2024, Paouris et al., 2021b]. This section describes the study that has been published in Mugatwala et al. [2024].

3.5.1 Revised Catalogue of Geo-effective CME-ICME

The DBM inversion described in Appendix A.3 requires $[r_0, r_{1AU}, t_{1AU}, v_0, v_{1AU}]$ as input to obtain the free DBM parameters w and γ. For this work, the CME-ICME dataset published by Napoletano et al. [2022] is fully exploited. This dataset contains 213 CME-ICME pairs from the years 1997 to 2018, spanning the two solar cycles 23 and 24. The kinematic properties of CME at launch time were retrieved from the SOHO/LASCO CME Catalogue mentioned in Section 2.6.1. Whereas TOA and Speed of Arrival (SOA) have been obtained from Richardson and Cane ICME list discussed in Section 2.7.1. The SOHO/LASCO catalogue provides CME speed in POS, but DBM requires deprojected radial speed, which is derived using Equation 1 of Gopalswamy et al. [2009]. A more thorough explanation of this is provided in Appendix A2 of Napoletano et al. [2022]. Later, the DBM inversion procedure has been applied to this dataset to derive the PDFs for solar wind w and drag parameter γ. Furthermore, the results of this procedure are used to refine the dataset in terms of various quantities. The refined version of this catalogue is publicly available at `https://zenodo.org/records/8063404` for further studies. A brief description of the refined catalogue is provided in Appendix A.4.

3.5.2 Mathematical Framework

To produce more robust distributions of the free parameters in the DBM, we apply this inversion technique to this revised catalogue. During the DBM inversion process, it was discovered that analytical solutions to Equations A.33 and A.34 may not be possible. This outcome contradicts the initial hypothesis, which assumed that DBM assumptions would hold true for the CME events in the dataset. However, this discrepancy resulted from neglecting errors in key variables, such as initial position (r_0), target position (r_1), transit time (t_{1AU}), impact speed (v_{1AU}), and initial speed (v_0). This same issue may arise when the CME dynamics may not be entirely represented by the DBM (e.g., constant solar wind is not a realistic consideration; CME-CME interaction may play a crucial role).

Nevertheless, for the purpose of this study, the initial hypothesis was maintained, and uncertainties for the measured CME properties were included in the investigation. A pairwise selection approach is adopted in the calculations to address the errors associated with these quantities. A similar approach was also employed by Napoletano et al. [2022] in the inversion procedure to estimate w and γ, assuming that the parameters $[r_0, r_1, v_0, v_1, t_{1AU}]$ followed a Gaussian distribution. They drew random samples, with most of the samples concentrated around the peak of the Gaussian curve. In contrast, the pairwise approach used in this thesis enables the exploration of a broader parameter space, including regions where less probable values might exist.

In this methodology, the two parameters r_0 and r_1 were assumed error-free as their values were fixed. Specifically, r_0 is set to 20 $R_\odot$, and r_1 is the actual Sun-Earth distance at a time when CME was at r_0. The arrival speed of ICME was calculated as the mean of the solar wind speed during the observed plasma disturbance. Indeed, the arrival speed has some intrinsic error, but it is relatively small compared to the uncertainties in the initial speed and transit time; therefore, the error associated with the arrival speed is neglected. Thus, v_0 and t_{1AU} were the remaining parameters with significant uncertainties. To incorporate these uncertainties, we performed a pairwise selection of (t_{1AU}, v_0) for each DBM inversion iteration. Here, we have drawn values for both quantities from a normal distribution where the mean μ was observed value ("Transit_Time" and "v_r" were taken as μ) and standard deviation σ was based on the associated error for each quantity ("Transit_time_err" and "v_r_err" serving as σ). It is important to note that the tails of the normal distribution function extended to 3σ from the mean. A total of 40000 possible parameter pairs were generated through the pairwise selection procedure, which involved the selection of 200 samples for both t_{1AU} and v_0. After that, the DBM inversion procedure was carried out to determine the values of w and γ.

The DBM inversion process followed a Monte Carlo approach, resulting in

40000 potential solutions. A significant number of these solutions can not be physically feasible, such as instances where the value of w is negative. Equation 3.2 reveals that γ is related to the mass and cross-sectional area of CME, as well as the ambient solar wind density, and therefore, the value of γ must be in a certain range, following simple physics considerations [Vršnak et al., 2013]. In our initial analysis, we observed that an unreasonably high value of γ was occasionally produced during the inversion procedure, which could not be explained by typical CME characteristics. Thus, imposing constraints on the values obtained through the inversion procedure became necessary. The following constraints have been imposed on the inversion values.

1. $0 \leq w \leq 1000$ km/s
   Solar wind speed cannot be negative, and the typical speed for fast solar wind in literature is $800 km/s$. It is worth noting that the condition of realistic solar wind speed in Paouris et al. [2021b] is 300-600 km/s, which is very narrow compared to us.

2. $0.1 \times 10^{-7} \leq \gamma \leq 3.0 \times 10^{-7}$ km^{-1}
   It is important to note that the typical range for the γ parameter, in Vršnak et al. [2013], is $0.2 - 2.0 \times 10^{-7}$, but we widen this range to accept a few more extreme solutions. Similarly, Paouris et al. [2021a] has a range of $0.01 - 0.59 \times 10^{-7}$ for realistic drag parameter, but the values they obtain are in the range of $0.21 - 0.48 \times 10^{-7}$ [See Table-4 of Paouris et al., 2021a]. This is comparable to our range.

Following this, we derived four key quantities: w_{mean}, γ_{mean}, w_{opt}, γ_{opt} based on the accepted values of w and γ. Here, the "opt" values correspond to the DBM inputs that produced the smallest deviation from the observed transit time. To assess the "goodness" of the inversion procedure, the "Acceptance Rate" is defined as the ratio of the number of feasible solutions to the total number of possible solutions, represented by the number of samples drawn.

$$\begin{matrix}\text{Acceptance Rate}\\ \text{(AR)}\end{matrix} = \frac{\begin{matrix}\text{no. of physically}\\ \text{feasible solutions}\end{matrix}}{\begin{matrix}\text{Total no. of}\\ \text{solutions}\end{matrix}} = \frac{m}{n \times n}. \tag{3.6}$$

Here m represents the number of solutions accepted after applying the constraints, and n denotes the total number of samples drawn from the t_{1AU} and v_0 distributions. Figure 3.5 illustrates the flow diagram of the DBM inversion procedure applied to the CME dataset and how the results of the inversion process were analysed.

3.5.3 Results

The inversion procedure was applied to the entire CME-ICME catalogue, and it was successful in 204 events out of 213. As a result of the inversion procedure, a total of 3,664,748 possible values for w and γ were obtained, making it possible to establish their statistical distribution. From the DBM Equation 3.1, It is obvious that during their propagation, CMEs either accelerate or decelerate. Based on these propagation direction mechanisms, two distinctive distributions were derived: accelerated CMEs and decelerated CMEs. Furthermore, solar wind parameter w can be categorised into two groups—slow and fast. Therefore, two additional joint distributions were derived depending on the solar wind condition. Figure 3.6 provides the visualisation of the (γ, w) phase space for all the CME events in the catalogue along with accelerated and decelerated CMEs events. In the plots, it is evident that each CME event creates a family of solutions that cluster together in stripes.

3.5.3.1 Goodness of DBM Inversion Procedure

The DBM inversion should have produced around 8,160,000 alternative values for γ and w, which is more than twice the number obtained, despite the fact that we reported the inversion working for 204 occurrences. This discrepancy is likely because of failed DBM inversion attempts or rejection of some (γ, w) pairs for failing to satisfy the constraints stated above. This issue is also evident in the (γ, w) phase space of the CME events. To address this, we categorised the events based on the density in the (γ, w)phase space, assigning them labels of "Optimal Fit," "Suboptimal Fit," or "Inadequate Fit." This categorisation allows us to evaluate the degree to which the DBM describes the propagation of single ICME events in the dataset. For consistency, the labels are determined by the "Acceptance Rate," defined in Equation 3.6. The specifications for each label are as follows:

1. Optimal (Nice) Fit: $\mathrm{AR} > 0.5$; the DBM approximation is highly accurate for this type of CME event, as the inversion procedure succeeds for more than 50% of the pairs, resulting in a clear stripe in the (γ, w)phase space

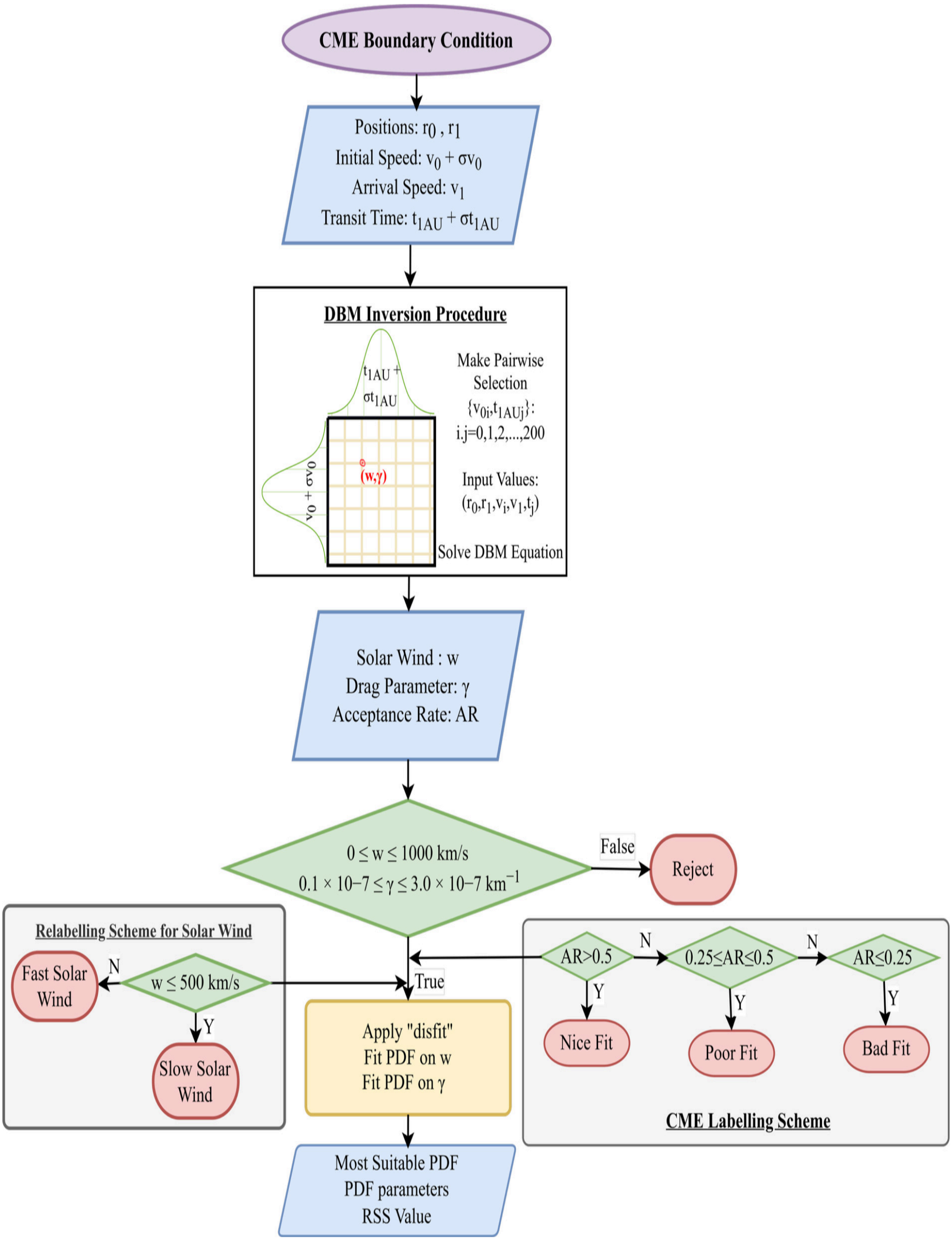

Figure 3.5: Schematic of DBM inversion procedure applied on the dataset and refinement process. The boundary value conditions are inserted into Equations A.33 and A.34 using a pairwise framework to obtain w and γ. The obtained values are checked for constraints. The accepted values are used to determine the solar wind condition, the most suitable PDF of parameters, and the CME labelling scheme. Adapted from Mugatwala et al. [2024]

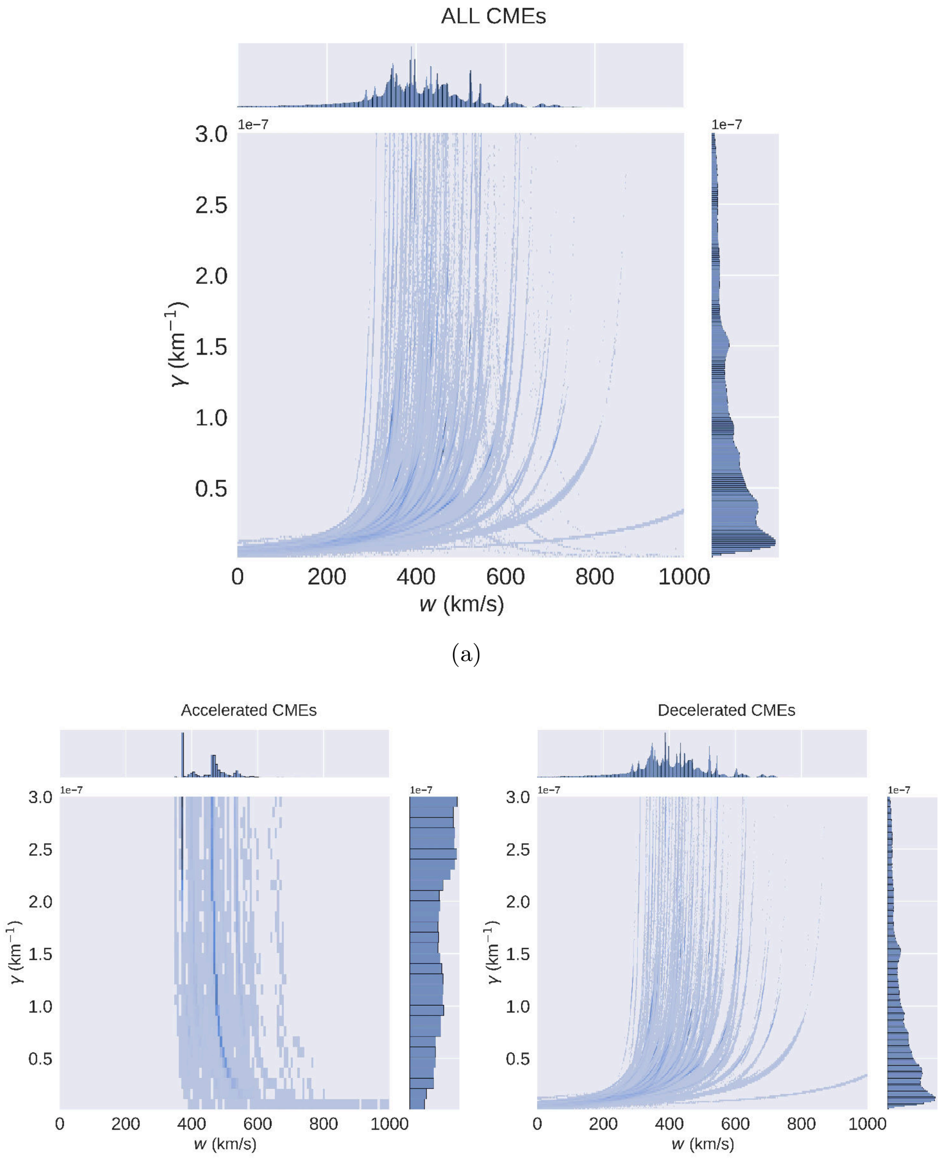

(a)

(b)

(c)

Figure 3.6: Joint distribution of (γ, w) arose as a result of the inversion procedure. (a): (γ,w) phase space for the whole catalogue (3,644,748 values). (b): (γ,w) phase space for accelerated CMEs (25,428 values). (c): (γ,w) phase space for decelerated CMEs. Adapted from Mugatwala et al. [2024]

2. Suboptimal (Poor) Fit: $0.25 \leq \text{AR} \leq 0.5$; the DBM is moderately accurate for these events, as a visible stripe is still present in the (γ, w) phase space.

3. Inadequate (Bad) Fit: $\text{AR} < 0.25$; the DBM approximation is less applicable to these events, leaving no discernible stripe in the phase space.

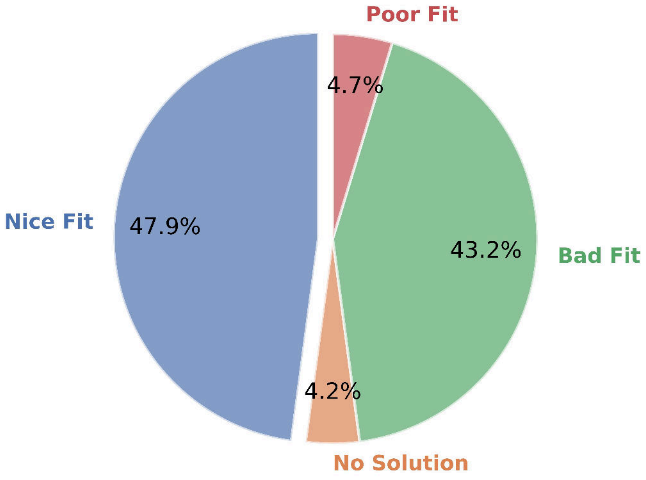

Figure 3.7: A pie chart showing a percentage of events in the "Optimal Fit", "Suboptimal Fit", and "Inadequate Fit".

Figure 3.7 shows the percentage of events allocated to each label. It is critical to stress that this labelling scheme is an important component of the dataset obtained by this study, providing information about which CME incidents are well defined by the DBM. Events labelled as "Suboptimal Fit" or "Inadequate Fit" require further investigation. Moving forward, we considered only the Optimal Fit events to derive the PDF for (γ, w), as this improves the statistical distributions. Finally, these updated statistics will improve the accuracy of CME arrival time estimates.

3.5.3.2 Relabelling Scheme for Solar Wind

It is essential to bear in mind that only 28 CME events from the catalogue exhibit acceleration during propagation, i.e., only around 13% of the dataset.

Consequently, the statistics for accelerating CMEs are not well resolved.

Alternatively, we categorised the CMEs according to solar wind conditions experienced during propagation to generate a distribution for the free DBM parameters. Exploiting the work of Napoletano et al. [2022], the solar wind type information (Column: SW_type -S/F, see Table A.1) was included, determined by proximity of Coronal Holes to the CME source region. However, the set of CMEs formed according to coronal hole presence produced two essentially overlapping distributions for fast and slow solar wind speeds. This overlap does not support the anticipated difference between fast and slow solar wind conditions. This disparity most likely resulted from the PDF for solar wind being calculated with the inclusion of coronal hole presence without considering the value of solar wind speed. In many cases, CME was not encountering a stream of fast solar wind during its propagation, and this correlation became incorrect.

The DBM inversion frequently produced small values of w, but the presence of coronal holes misidentified those values as fast solar wind. Hence, those mismatches result in overlapping distribution. Furthermore, the model's accuracy is compromised by the high standard deviation in these distributions, which makes it less suitable for robust real-time space weather forecasting. In order to tackle this problem, the threshold of roughly $w_{sim} \geq 500km/s$ was applied to discriminate the fast solar wind from the slow one. This threshold is consistent with the one used by Napoletano et al. [2018]. Figure 3.8 demonstrates the (γ,w) phase space for the two solar wind categorisation schemes: the original "SW_type" and revised "Wind_type". It is essential to bear in mind that the tail areas of any distribution that appear in the negative domain are a consequence of the charting method and not an indication that the dataset contained negative values. We will be focusing on this revised solar wind speed labelling approach for all further analysis.

3.5.3.3 Solar Wind Speed PDF

From the joint distribution presented in Figure 3.6, we derived a Probability Distribution Function (PDF) for the solar wind speed w. To achieve this, we fitted Gaussian, Student's-t, and lognormal distribution functions on the values obtained from the DBM inversion procedure. These functions are selected because of their best-fit score among the several PDF available in the "distfit"

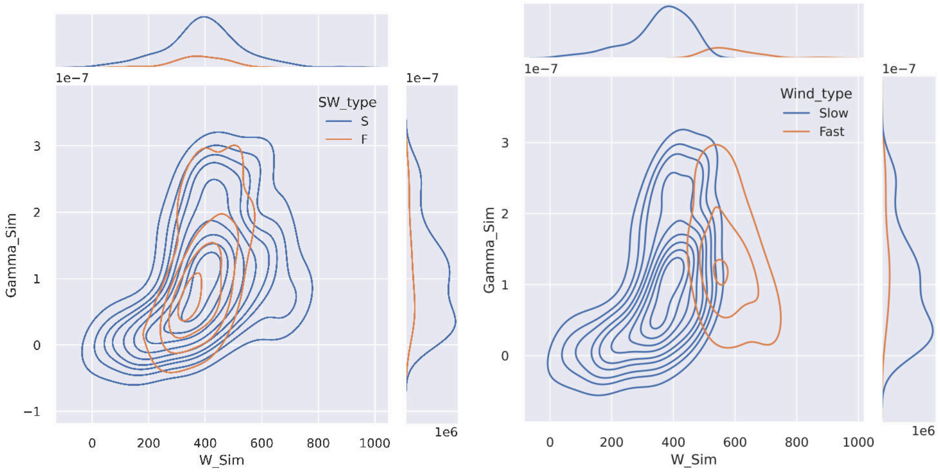

Figure 3.8: (γ, w) phase space for different solar wind speed classification schemes. The x-axis represents the solar wind speed obtained from DBM inversion W_{sim} (in km/s), while on the y-axis, the drag parameter Γ_{sim} is shown (with km^{-1} as the unit).

package [Taskesen, 2023]. Figure 3.9 illustrates the histogram obtained from the dataset, along with the best-fitted PDFs. In most cases where CME events are categorised as accelerated or decelerated, the three distribution functions yielded comparable Residual Sum of Square (RSS) values, as reflected in the figure. The parameters for the fitted distributions are presented in Table 3.1. On the contrary, RSS values differed significantly between the slow and fast solar wind conditions. For CMEs travelling through the slow solar wind (hereafter slow CMEs), the student's-t distribution provided the best fit, while CMEs propagating through the fast solar wind (hereafter fast CMEs) the log-normal distribution function was the most suitable. It is important to note that the hard threshold employed to distinguish between the solar wind types had a significant impact on these distributions.

Paouris et al. [2021a] considered the same 16 CME-ICME events from the Dumbović et al. [2018] to investigate the optimal values for the solar wind speed w and drag parameter γ through the inversion technique. The optimal values of w from different studies are shown in Table 3.2, which also emphasises that the increased standard deviation seen in the results is probably explained by the bigger sample sizes utilised in Napoletano et al. [2022] and this thesis.

CME Group	PDF	$\bar{w}$[km/s]	σ_w[km/s]	Args	RSS
Accelerated	Normal	503.356	55.848	-	0.000538
	Student's-t	503.356	55.848	1.526×10^6	0.000538
	Lognormal	-0.407	3.910	349.009	0.001469
Decelerated	Normal	409.168	117.545	-	0.00046
	Student's-t	409.168	117.543	1.479×10^5	0.00046
	Lognormal	9.524	0.009	-1.328×10^4	0.000458
Slow	Normal	370.530	88.585	-	0.000714
	Student's-t	383.169	64.944	4.101	0.000622
	Lognormal	9.784	0.005	-1.738×10^4	0.00072
Fast	Normal	579.058	67.871	-	0.002862
	Student's-t	579.058	67.872	1.837×10^6	0.002862
	Lognormal	4.084	0.883	494.597	0.001934

Table 3.1: Parameters for the different functions used to model the solar wind speed distribution. For the Lognormal function, tabulated values can not be used directly as average and standard deviation. The transformation from the fitting parameters to values used in the model can be done by the Equation A.38.

	Optimal Solar wind speed w [km/s]	Standard deviation σ_w [km/s]
Dumbović et al. [2018]	350	50
Napoletano et al. [2018] (slow)	400	33
Napoletano et al. [2018] (fast)	600	66
Paouris et al. [2021a]	431	57
Čalogović et al. [2021]	453	64
Napoletano et al. [2022] (slow)	370	80
Napoletano et al. [2022] (fast)	490	100
Mugatwala et al. [2024] (slow)	370	88
Mugatwala et al. [2024] (fast)	579	68

Table 3.2: Optimal(mean) values for solar wind speed w from different studies. Adapted from Mugatwala et al. [2024]

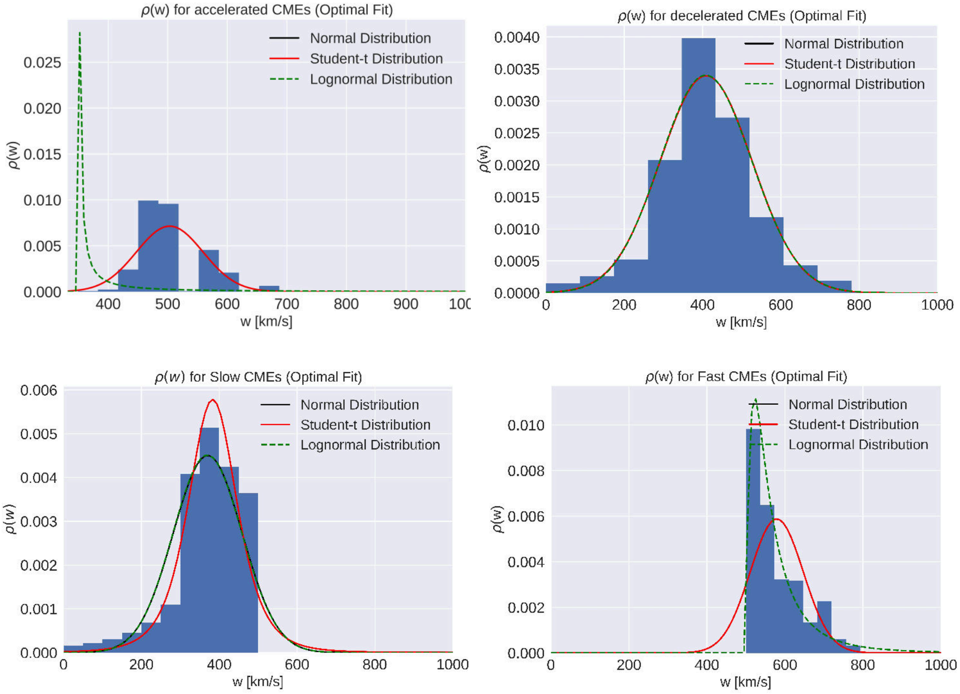

Figure 3.9: Various PDFs fitting for the solar wind. Top-left: accelerated CMEs. Top-right: decelerated CMEs. Bottom-left: slow CMEs Bottom-right: fast CMEs. Adapted from Mugatwala et al. [2024].

3.5.3.4 Drag Parameter PDF

For the drag parameter γ, we applied the same methodology and distribution functions as those used for the solar wind speed to derive PDFs. There was a significant amount of variance in the RSS values that were determined from the various fits. When compared with the other distribution functions, the lognormal distribution consistently delivered the optimal fit throughout most, if not all, cases. Figure 3.10 illustrates the fitted distribution function for the four CME categorisations. Table 3.3 displays the fitting parameters for the drag parameter γ for four distribution functions.

CME Group	PDF	$\bar{\gamma}$ [km^{-1}]	σ_γ [km^{-1}]	Args	RSS
Accelerated	Normal	1.590×10^{-7}	5.793×10^{-8}	-	2.528×10^{13}
	Student's-t	1.503×10^{-7}	4.247×10^{-8}	1.988	2.490×10^{13}
	Lognormal	-15.642	0.354	-1.186×10^{-8}	6.385×10^{12}
Decelerated	Normal	9.339×10^{-08}	7.562×10^{-08}	-	1.089×10^{15}
	Student's-t	6.899×10^{-08}	5.016×10^{-08}	1.988	8.029×10^{14}
	Lognormal	-16.178	0.652	0.6518	2.723×10^{14}
Slow	Normal	8.609×10^{-08}	7.419×10^{-08}	-	1.519×10^{15}
	Student's-t	5.936×10^{-08}	4.595×10^{-08}	1.988	1.010×10^{15}
	Lognormal	-16.252	0.658	-2.276×10^{-08}	4.034×10^{14}
Fast	Normal	1.256×10^{-07}	7.342×10^{-08}	-	5.319×10^{14}
	Student's-t	1.079×10^{-07}	5.238×10^{-08}	1.988	4.749×10^{14}
	Lognormal	-15.884	0.518	-1.838×10^{-08}	2.575×10^{14}

Table 3.3: Parameters for different PDFs used to model drag parameter distribution. For the Lognormal function, tabulated values can not be used directly as average and standard deviation. The transformation from the fitting parameters to values used in the model can be done by the equation A.38. Adapted from Mugatwala et al. [2024]

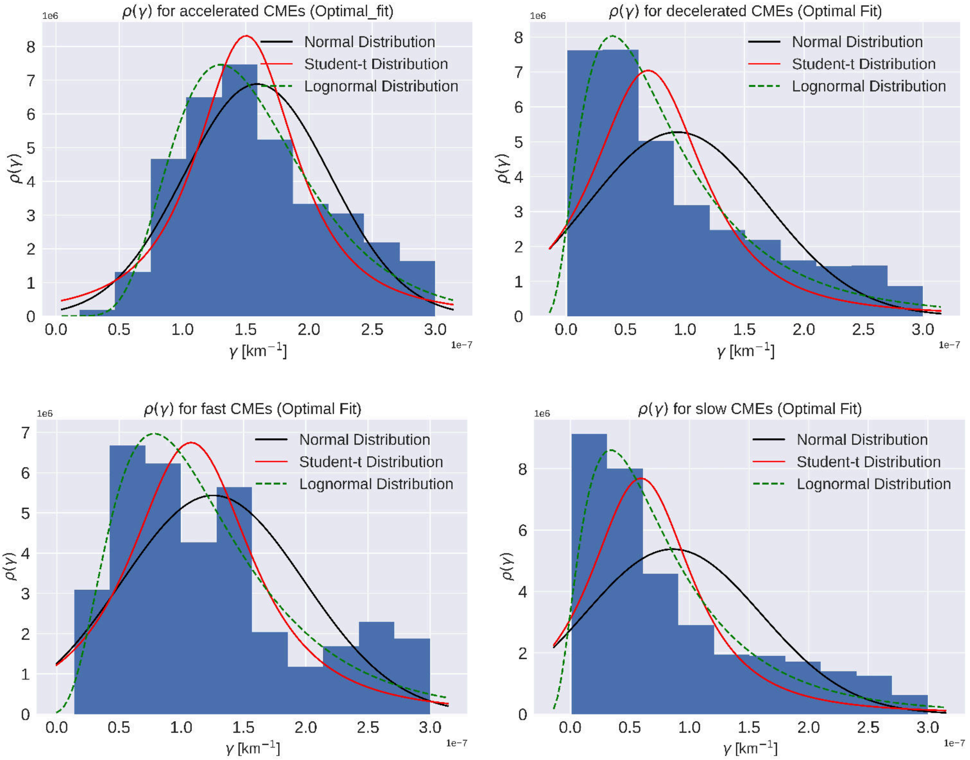

Figure 3.10: Various PDFs fitting for the drag parameter γ. Top-left: accelerated CMEs. Top- right: decelerated CMEs. Bottom- left: slow CMEs Bottom-right: fast CMEs. Adapted from Mugatwala et al. [2024].

Chapter 4

ICME Detection in the Heliosphere

This chapter focuses on the expanding capabilities of P-DBM to predict CME arrival time in the heliosphere. The chapter begins with outlining various planetary ICME datasets that hold significant interest in this study. Following this, a concise explanation on CME-ICME Lineup Catalogue preparation is provided. The chapter concludes by outlining the preliminary results obtained through the P-DBM application to this newly developed catalogue.

4.1 Introduction

Space weather research has entered a new era of remarkable observational capabilities, thanks to the deployment of a diverse set of spacecraft dedicated to investigating the Sun, solar wind, and planetary conditions across the solar system. These missions encompass SOHO, STEREO, SDO, SolO, PSP, Wind, Bepicolombo, MESSENGER, MAVEN, VEX, and Juno, and have been sued to make numerous multi-point observations. The combined data from these spacecraft provide a genuine goldmine of resources for investigating interplanetary space and its complicated connections with solar activity. The advantage of these missions is not just their number but also the range of perspectives they bring. The fleet consists of observatories that observe the Sun from various perspectives (for example, STEREO's dual spacecraft provide several angles on solar events) as well as spacecraft positioned across the heliosphere, including at planets (e.g., MESSENGER at Mercury, MAVEN at Mars). As a consequence, the current scientific environment facilitates multi-viewpoint observations of CMEs, as well as multi-point in-situ measurements of ICMEs as they pass through the solar wind and influence multiple regions of the solar system.

This diversified and comprehensive dataset provides an excellent chance to improve the precision and scope of space weather forecasting models.

Researchers can gain a better understanding of the spatial and temporal evolution of CMEs and other solar phenomena by combining observations from multiple spacecraft throughout the heliosphere. This ability is critical not only for protecting assets near Earth but also for forecasting space weather conditions in other parts of the solar system, where missions and human activities are anticipated to increase in the coming years. The existence of spacecraft on many planets further enables us to make detailed space weather forecasts for regions beyond near-Earth space, such as Mars, Venus, and even Jupiter. Despite the huge amount of data, various problems remain that prevent the full use of these resources. Two significant issues arise in the research of space weather and the heliospheric impacts of solar eruptions:

1. Establishing a connection between solar eruptions observed in the solar corona and their signatures measured in situ by spacecraft in interplanetary space;

2. Finding events where more than one spacecraft measures the ICME characteristics at different locations in the heliosphere.

Addressing these issues is crucial for improving space weather forecasts. The ability to properly link solar eruptions to their interplanetary counterparts would improve prediction models of CME propagation and impact, allowing for more precise forecasts of space weather occurrences. Furthermore, extensive analyses of multi-spacecraft ICME data would provide new insights into the physical processes that drive CME evolution and interaction with the solar wind, thereby improving our understanding of solar-terrestrial connections.

4.2 Planetary ICME Catalogues

Before 2010, mostly ICME have been studied near the Earth using various spacecraft such as Wind, ACE (Richardson and Cane [2010], Schwenn et al. [2005], Zhang et al. [2008], Mitsakou and Moussas [2014] are just a few of many). Very few efforts have been made to investigate ICMEs in the inner heliosphere through Helios mission too [Cane et al., 1997, Leitner et al., 2007]. But just after 2010, data from various planetary missions resulted in ICME studies in inner heliosphere and beyond 1 AU [Winslow et al., 2015, Zhao et al., 2021, Good and Forsyth, 2016, Falkenberg et al., 2011, Witasse et al., 2017]. These various ICME studies from different planetary missions serve as key building blocks for the preparation of CME-ICME lineup events, and a few of them are briefly discussed here.

4.2.1 MESSENGER ICME List

The MErcury Surface, Space ENvironment, GEochemistry and Ranging (MESSENGER) spacecraft was designed to study the planetary formation of process, geological history and nature of the magnetic field of Mercury [Solomon et al., 2007]. Among its suite of onboard instruments aimed to achieve its science goal, Magnetometer (MAG) is the instrument that contributed significantly to the study of ICMEs propagating towards Mercury. During the initial phase, MESSENGER had an orbit period of 12 hr, during that phase spacecraft used to spend 8-10 hr in the interplanetary medium. Later on, the orbit period decreased to 8 hr, reducing the time spent in interplanetary space to 3-5 hours per orbit. Despite these relatively small windows outside Mercury's bow shock and magnetosphere, MESSENGER was able to observe Mercury-directed ICMEs. Winslow et al. [2015] has used MESSENGER-MAG data between 23^{rd} March 2011 and 17^{th} September 2014 and prepared a catalogue of ICME events observed near Mercury.

Usually, ICME identification is based on the combination of magnetic fields, plasma dynamics and particle signatures in in-situ data. However, MESSENGER lacks a dedicated onboard solar wind plasma analyser, and identifying ICME solely based on the magnetic field data is subject to uncertainties. For this reason, strict criteria were implemented in Winslow et al. [2015] for ICME identification.

1. Clear Interplanetary shock at arrival time,
2. shock was followed by sheath and Magentic Ejecta (ME) region.
3. Event lasted for the duration of at least one MESSENGER orbit through the magnetosphere.
4. Event caused a visible distortion of Mercury's magnetosphere in the magnetic field observation.

with this criteria, catalogued ICMEs are shock-driving ICMEs with strong ME,introducing an observational bias towards fast CMEs with strong magnetic fields. A total of 61 ICME events were identified in the study of Winslow et al. [2015]. This ICME catalogue includes detailed information about each ICME event, such as ICME shock arrival-end time, ME arrival-end time, average magnetic field magnitude before and after shock, maximum and mean magnetic field for entire ICME,ME and sheath. Additionally, efforts have been made to identify CME counterpart of each ICME event using SOHO/LASCO and STEREO/SECCHI observations. Once CME-ICME links were established, kinematic properties of CME have been obtained from CDAW CME catalogue and DONKI. (See Winslow et al. [2015] for more detailed discussion on the ICME identification and further analysis about ICME properties at Mercury and it's comparison at 1AU using near Earth ICME)

4.2.2 MAVEN ICME List

The Mars Atmosphere and Volatile EvolutioN (MAVEN) spacecraft was launched to investigate the effects on the Martian magnetosphere and upper atmosphere by the Sun and solar wind [Jakosky et al., 2015]. Particles and field measurement instruments on board the spacecraft such as Solar Wind Ion Analyzer (SWIA),Solar Wind Electron Analyzer (SWEA), MAG and Solar Energetic Particle (SEP) instrument provided opportunities to investigate ICME properties near Mars. Even with the presence of magnetic field and particle measurement instruments, ICME identification is not straightforward due to the fact that Mars does not have a global magnetic field. Therefore, the Martian atmosphere directly interacts with the solar wind [Möstl et al., 2017, Ma et al., 2018].

Considering this limitation, Zhao et al. [2021] used the solar wind proton flux data from SWIA to prepare a list of ICME observed at MAVEN. The primary criteria for ICME identification used by those authors is an abnormally low proton temperature, i.e. a condition where proton temperature is very low for the corresponding observed solar wind velocity. In their study, they obtained the relationship between temperature T and velocity V for qualitative diagnostics to infer depression in solar wind temperature using 57 intervals of slow streams and 34 intervals of high streams from unperturbed coronal holes [Zhao et al., 2021]. If onboard measured T is relatively low to expected temperature T_{exp} from $T - V$ relationship, this suggests an ICME association. Additionally, the combination of ICME signatures, such as enhanced magnetic field intensity, smooth rotation in a magnetic field and low plasma β, are used to identify the ICMEs. Using the criteria mentioned above, Zhao et al. [2021] identified the 24 ICMEs in MAVEN data during the time span of December 2014 to February 2019. We have identified the CMEs associated with the measured ICMEs and added them to our catalogue. (See Zhao et al. [2021] for addition in depth discussion on ICME identification and ICME properties near Mars)

4.2.3 HELIO4CAST - LineupCAT

The LineupCAT[1] is a catalogue of ICMEs observed by multiple spacecraft. For this study, we have used version 1.0 of the catalogue covering the multipoint CME events observed from April 2020 to April 2021 [Möstl et al., 2022]. This list is one of the primary blocks for the CME-ICME lineup catalogue that is prepared for this thesis. The event list published as a result of Möstl et al. [2022] consists of 16 events where the connection between HI-A observation and at least one in-situ spacecraft was made. Therefore, this event list has significantly reduced our work in terms of finding in-situ measurements for lineup ICMEs. Additionally, the link to remote observations through HI-A significantly helped to find the responsible CME in SOHO and STEREO data.

The LineupCAT is prepared using a few existing CME-ICME catalogues resulting from HELCATS project. The catalogues used for LineupCAT are:

1. HIGeoCAT[2]

   This catalogue is a source of CME kinematics such as propagation direction and speed derived from the HI-A observations [Barnes et al., 2019].

2. ARRCAT[3]

   This catalogue provides the modelled arrival time of CMEs at various spacecraft and planets using STEREO/HI data.

3. ICMECAT[4]

   This catalogue provides ICME observations from various spacecraft and is discussed briefly in Section 2.7.4.

---

[1] Link to HELIO4CAST/LineupCAT: `https://www.helioforecast.space/lineups`

[2] HIGeoCAT: `https://www.helcats-fp7.eu/catalogues/wp3_cat.html`

[3] ARRCAT: (I)-`https://www.helioforecast.space/arrcat`
(II)-`https://www.helcats-fp7.eu/catalogues/wp4_arrcat.html`

[4] ICMECAT: V1.0- `https://www.helcats-fp7.eu/catalogues/wp4_icmecat.html`
V2.0- `https://www.helioforecast.space/icmecat`

Using data from these catalogues, ICME events are considered as multipoint ICME events if the modelled time from ARRCAT is $\Delta_t < \pm 24$ hr within the in-situ arrival time of ICMECAT. The relaxation is given by the condition that the ICME misse the in-situ spacecraft by $< 20\%$ and within Δ_t limit are also considered as multipoint CME events.

4.2.4 Miscellaneous

The ICME lists mentioned in Section 4.2 serve as foundations of the catalogue that we have prepared. The ICME sources are not limited to the mention only in 4.2 and 2.7. There are various studies done in recent years where ICME lists have been compiled using various spacecraft such as ICME list by Juno [Davies et al., 2021b, Davies, 2021], PSP ICME list [Salman et al., 2024], VEX ICME list [Good and Forsyth, 2016] are also used passively in the ICME data source that we have used. Additionally, numerous studies have been conducted where radial evolution of CME-ICME have been investigated [Winslow et al., 2021, Soni et al., 2023, Davies et al., 2021a, Witasse et al., 2017, Salman et al., 2020, Asvestari et al., 2021, Davies et al., 2022, Good et al., 2019, Kilpua et al., 2021]. Events from these various studies also have scope to be added to our catalogue.

4.3 CME-ICME Lineup Event Catalogue

This catalogue is among the major data products resulting from this thesis work and will be key to extending and testing the capabilities of P-DBM in the heliosphere. We have identified a total of 60 CME-ICME lineup events using the ICME sources outlined in Section 4.2 and make the list publicly available at https://doi.org/10.6084/m9.figshare.25869190.v1. The compilation of this dataset required the careful task of linking ICME with its associated CME counterpart observed near the solar surface. Once the responsible CME is identified, its kinematics and morphological information, such as angular width and propagation direction, are used to identify the potential heliospheric targets that the ICME might have affected. For this purpose, Solar-MACH[5]- an open source tool for plotting longitudinal configuration of multiple spacecraft was implemented to visualize the location of various planets and spacecraft in

---

[5] Link to Solar-MACH web interface: https://solar-mach.github.io/

the heliosphere [Gieseler et al., 2023]. In the later stage, plasma and magnetic field data of those potential heliospheric targets (spacecraft) are exploited to determine ICME properties at the target's location. In theory, this approach is very straightforward, but it is highly demanding in terms of time and human effort.

To summarize, here is a step-by-step description of how CME-ICME Lineup Catalogue was prepared:

- **Step-1: ICME Data Source**

  In this step, ICMEs have been identified using in-situ measurements of solar wind. Various ICME properties such as the magnitude of magnetic field ($|B|$), southward magnetic field component (B_z), proton density (N) and a few others are documented for further analysis. It is important to note that ICME properties are error-prone due to, e.g. other solar wind disturbances and intrinsic measure errors. In this study, Mercury, Venus, Earth, and Mars in planet category and MESSENGER, VEX, Wind, STEREO-A/B, SolO, PSP, MAVEN, Kepler, Ulysses spacecraft are considered. The planetary ICME lists discussed in Section 4.2 served as the foundational dataset. Also, the use of existing ICME lists discussed in Section 2.7 reduces the manual workload involved in the identification of ICME.

- **Step-2: CME Information**

  This stage deals with finding the CME counterpart of each ICME near its solar source. This stage is crucial as the wrong CME-ICME association totally invalidates the analysis. Given the variability in CME kinematics, ICMEs can take anywhere from a few hours to several days to reach their targets in the heliosphere, leading to an extended time window for the research. As a result of this large time window, this step requires extensive manual investigations of all the possible CME candidates for that particular ICME. For Example, a typical ICME generally takes 2 to 5 days to reach 1 AU. Therefore, it is necessary to investigate all the CMEs from that duration to link an ICME with its unique CME counterpart. Key parameters such as CME propagation direction and half-width help significantly to make this one-to-one CME-ICME correspondence. The DONKI catalogue provides essential information for that. Once the CME-ICME connections are established, the relevant information retrieved from DONKI is also reported.

- **Step-3: ICMEs in Heliosphere**
  In this step, the angular width and propagation direction of the CMEs were used to define a "cone of interest" for potential targets. The cone is defined by an angular interval $[\phi_{CME} - \omega, \phi_{CME} + \omega]$, where ϕ_{CME} is CME propagation direction and ω is half angular width of CME. Any spacecraft or planet located within that cone during the CME launch is considered a potential target. In cases where planets or spacecraft positions miss the criteria of a cone of interest by a minor margin(5-10°), those are also considered as potential targets to include the uncertainties in the half-width and propagation direction. Once the list of potential ICME targets has been prepared, their respective in-situ data are used to determine the ICME properties. To speed up this process, existing ICME lists were used whenever possible, and appropriate entries were added to the catalogue.

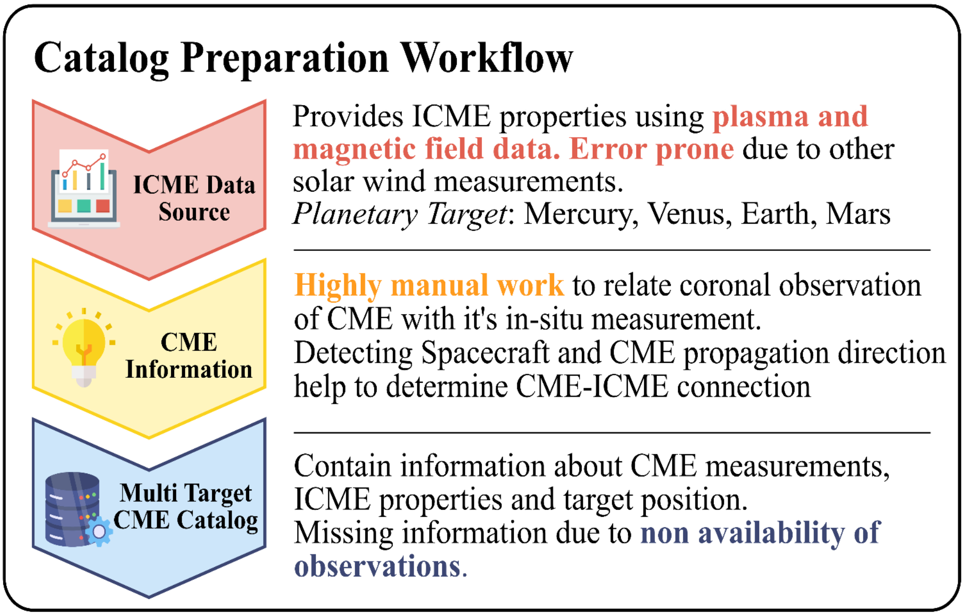

Provides ICME properties using **plasma and magnetic field data. Error prone** due to other solar wind measurements.
Planetary Target: Mercury, Venus, Earth, Mars

Highly manual work to relate coronal observation of CME with it's in-situ measurement.
Detecting Spacecraft and CME propagation direction help to determine CME-ICME connection

Contain information about CME measurements, ICME properties and target position.
Missing information due to **non availability of observations**.

Figure 4.1: The flow chart displaying systemic steps that have been used to prepare the "CME-ICME Lineup catalogue".

To wrap it up, a rigorous and systematic method was employed to build the CME-ICME Lineup Catalogue, which involved combining observational data from multiple sources. This dataset provides an essential resource for studying the propagation of ICMEs in the heliosphere and their impact on different heliospheric targets. The availability of this dataset will significantly improve studies on space weather and enhance models that predict CMEs and ICMEs in the heliosphere. Figure 4.1 illustrates the process of CME-ICME lineup catalogue.

4.3.1 Variation in CME-ICME Properties

Figure 4.2 presents the variation of observed transit time and arrival speed of each ICMEs events from the catalogue. The top panel suggests that the transit time of ICME is increasing with the heliocentric distance, and its variation also rises e.g., for ICME, It takes from a few hours up to two days to reach Mercury while it takes between 2 to 5 days to reach Earth. In the bottom panel, it is evident that ICME is catching up with ambient solar wind, which is consistent with the typical deceleration of ICMEs as they propagate through the heliosphere. This is supported by the fact that major ICMEs have speeds ranging between 350 or less to 600 km/s near Earth, which is measured as typical solar wind speed at 1AU. Figure 4.3 illustrates the variation in the mean value of a magnetic field and its relation with the speed of magnetic ejecta. It is important to note that latitudinal variations have been neglected in this study. This exclusion introduces challenges in the analysis of ICME properties, as each spacecraft observes different parts of the ICME structure.

The primary objective of this thesis is to investigate the P-DBM application in the heliosphere beyond 1AU. Therefore, the DBM inversion procedure has been applied to this catalogue as well. Table A.2 shows the various observed properties of ICME and CME, along with quantities derived from Drag Based Model fitting for each ICME lineup events in the catalogue. Figure 4.4 shows the correlation between the CME kinematics derived from the coronagraphic observation and the in-situ measurements of the corresponding ICME properties. Figure 4.5 illustrates the DBM parameters, namely w and γ as a function of heliocentric distance. The values are colour-coded by the speed of CME to investigate any dependencies of model parameters on it. Figure 4.8 displays the correlation between measured CME-ICME properties and the DBM parameters. This comparison allows for a deeper understanding of the relationship between the remote sensing of CMEs, their evolution as

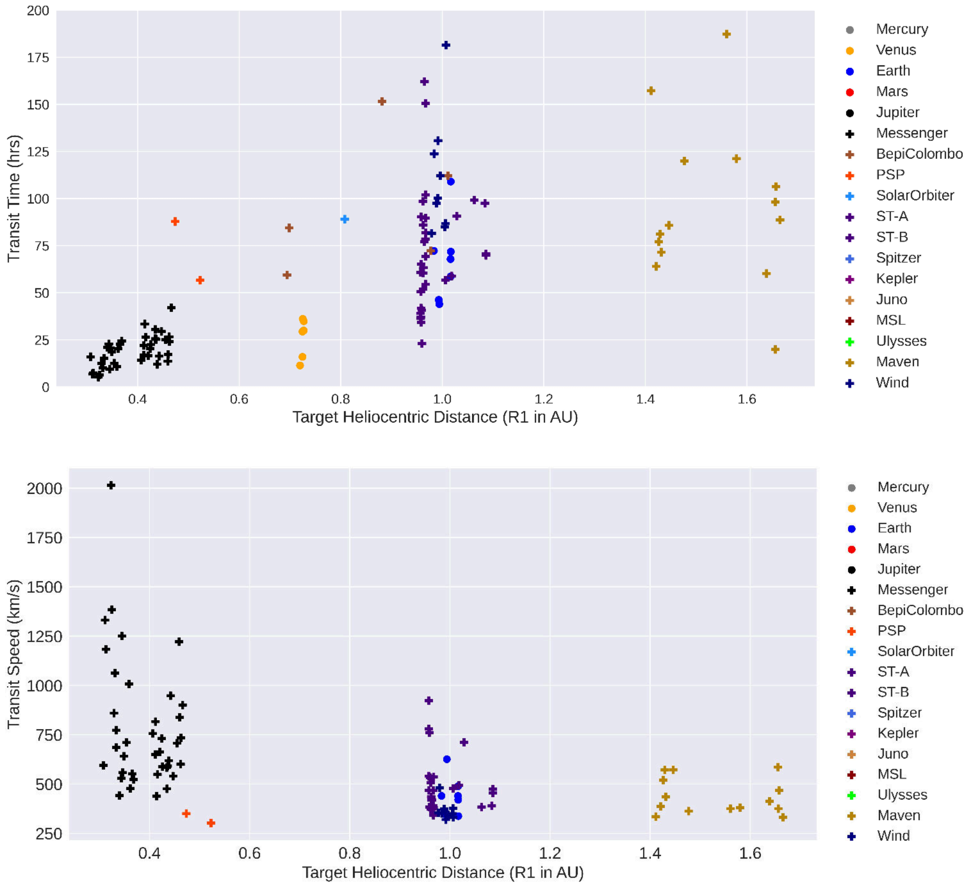

Figure 4.2: The plots displaying the variation in ICME arrival time and speed as ICME propagate in the heliosphere. The top panel shows the transit time of ICME as a function of heliocentric distance, while the bottom panel represents the ICME transit speed. The planets are demonstrated as filled circles (●), whereas spacecraft are represented as + to identify the target type.

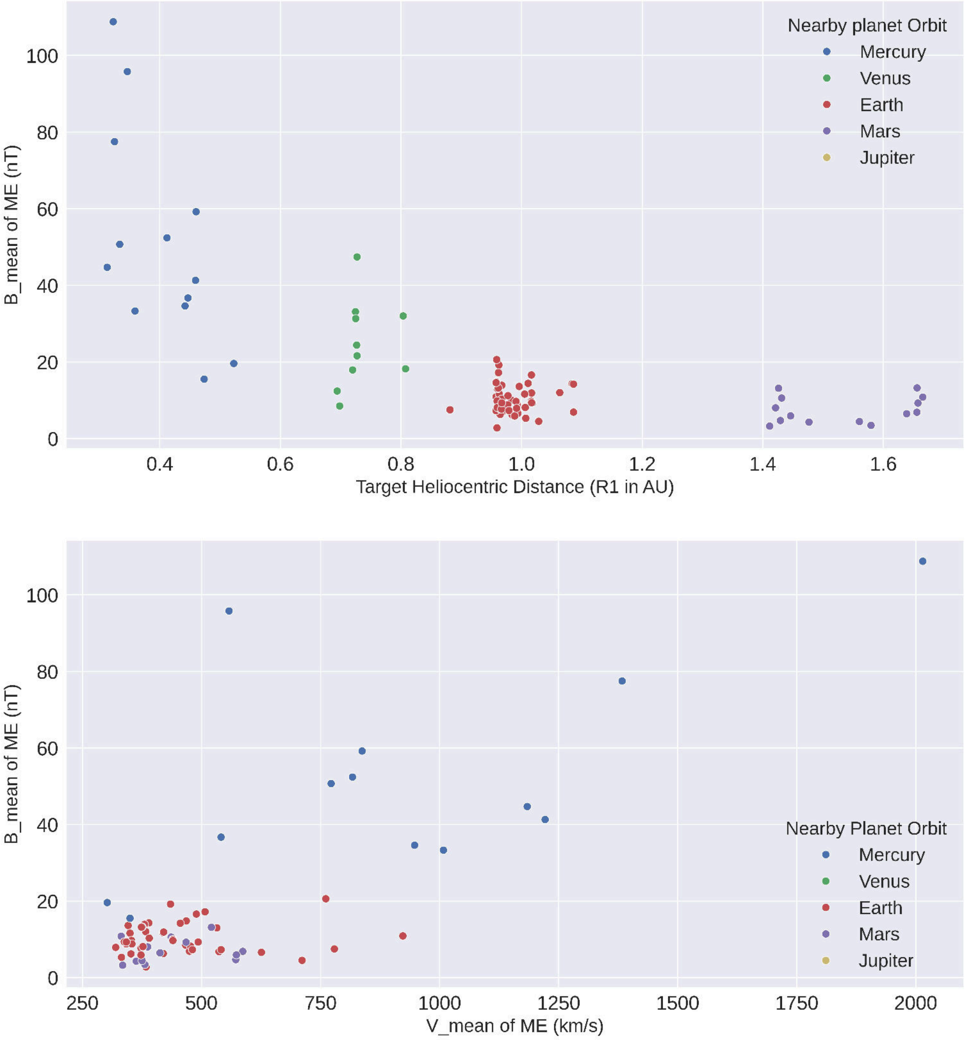

Figure 4.3: The plot representing a magnetic field intensity of ICME as a function of heliocentric distance and ICME speed.

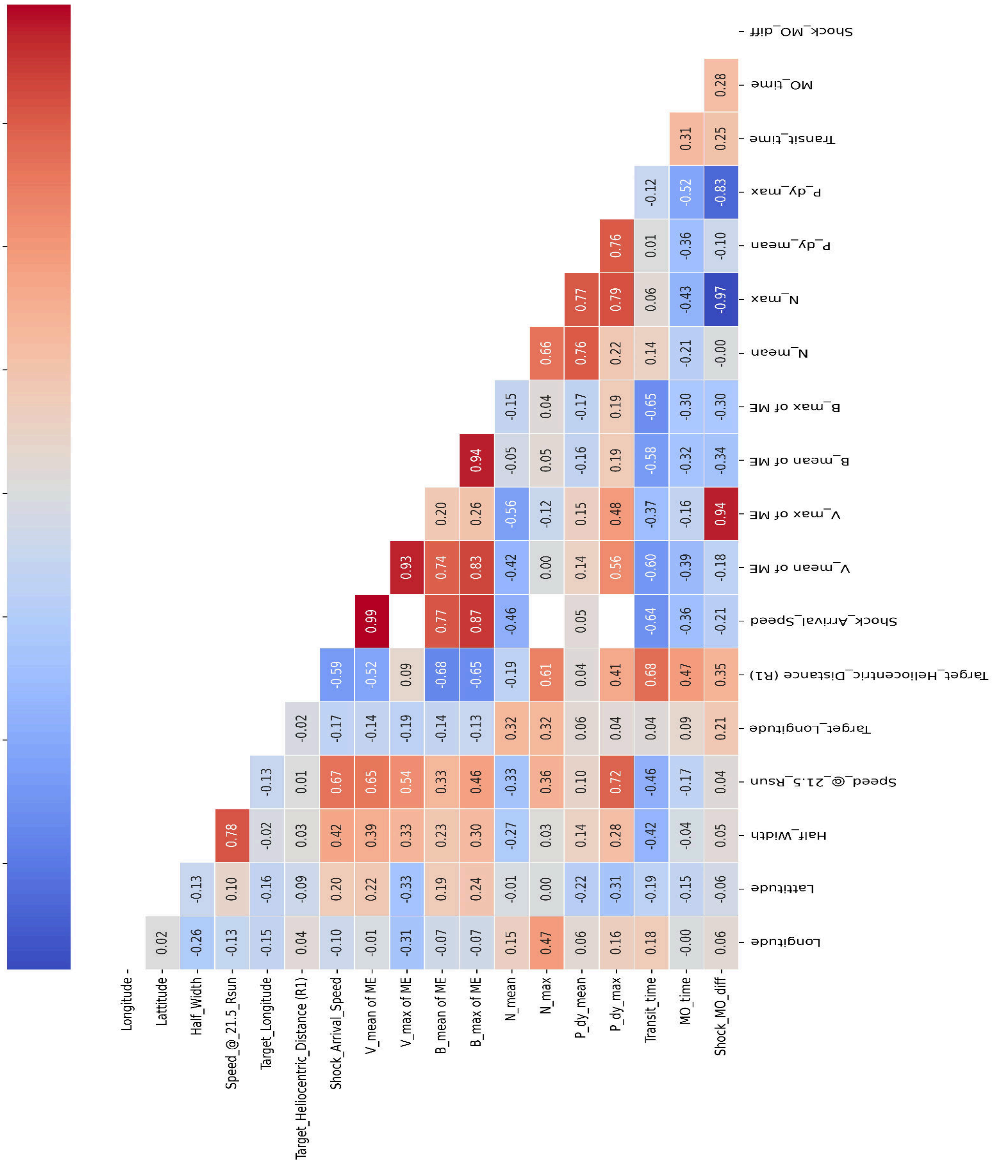

	Longitude	Lattitude	Half_Width	Speed_@_21.5_Rsun	Target_Longitude	Target_Heliocentric_Distance (R1)	Shock_Arrival_Speed	V_mean of ME	V_max of ME	B_mean of ME	B_max of ME	N_mean	N_max	P_dy_mean	P_dy_max	Transit_time	MO_time	Shock_MO_diff
Longitude																		
Lattitude	0.02																	
Half_Width	-0.26	-0.13																
Speed_@_21.5_Rsun	-0.13	0.10	0.78															
Target_Longitude	-0.15	-0.16	-0.02	-0.13														
Target_Heliocentric_Distance (R1)	0.04	-0.09	0.03	0.01	-0.02													
Shock_Arrival_Speed	-0.10	0.20	0.42	0.67	-0.17	-0.59												
V_mean of ME	-0.01	0.22	0.39	0.65	-0.14	-0.52	0.99											
V_max of ME	-0.31	-0.33	0.33	0.54	-0.19	0.09		0.93										
B_mean of ME	-0.07	0.19	0.23	0.33	-0.14	-0.68	0.77	0.74	0.20									
B_max of ME	-0.07	0.24	0.30	0.46	-0.13	-0.65	0.87	0.83	0.26	0.94								
N_mean	0.15	-0.01	-0.27	-0.33	0.32	-0.19	-0.46	-0.42	-0.56	-0.05	-0.15							
N_max	0.47	0.00	0.03	0.36	0.32	0.61		0.00	-0.12	0.05	0.04	0.66						
P_dy_mean	0.06	-0.22	0.14	0.10	0.06	0.04	0.05	0.14	0.15	-0.16	-0.17	0.76	0.77					
P_dy_max	0.16	-0.31	0.28	0.72	0.04	0.41		0.56	0.48	0.19	0.19	0.22	0.79	0.76				
Transit_time	0.18	-0.19	-0.42	-0.46	0.04	0.68	-0.64	-0.60	-0.37	-0.58	-0.65	0.14	0.06	0.01	-0.12			
MO_time	-0.00	-0.15	-0.04	-0.17	0.09	0.47	-0.36	-0.39	-0.16	-0.32	-0.30	-0.21	-0.43	-0.36	-0.52	0.31		
Shock_MO_diff	0.06	-0.06	0.05	0.04	0.21	0.35	-0.21	-0.18	0.94	-0.34	-0.30	-0.00	-0.97	-0.10	-0.83	0.25	0.28	

Figure 4.4: The matrix demonstrating the correlation between the CME kinematics derived from remote observation and the ICME properties measured in in-situ data of spacecraft.

observed through in-situ data at different points in the heliosphere along with the capabilities of P-DBM to predict ICME arrival time and speed.

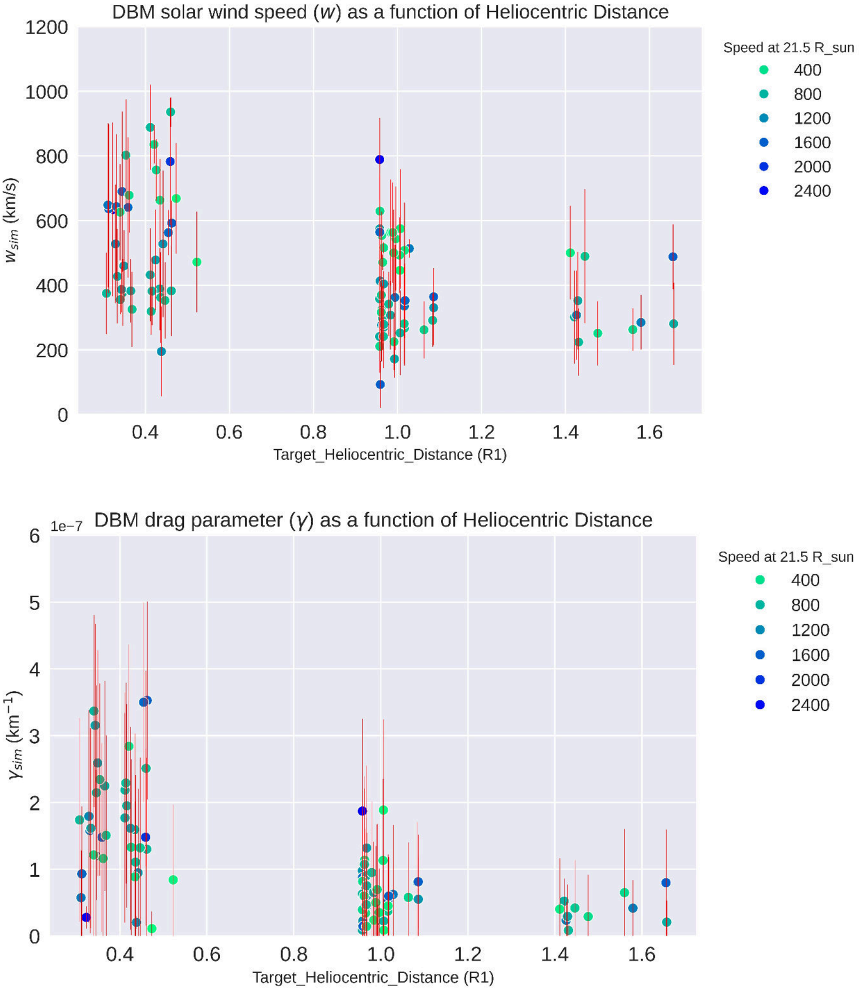

Figure 4.5: The plot illustrating variation in DBM free parameters as a function of heliocentric distance.The top panel shows the fluctuations in modelled solar wind speed, and the bottom panel demonstrates the modelled drag efficiency obtained using the DBM inversion method.

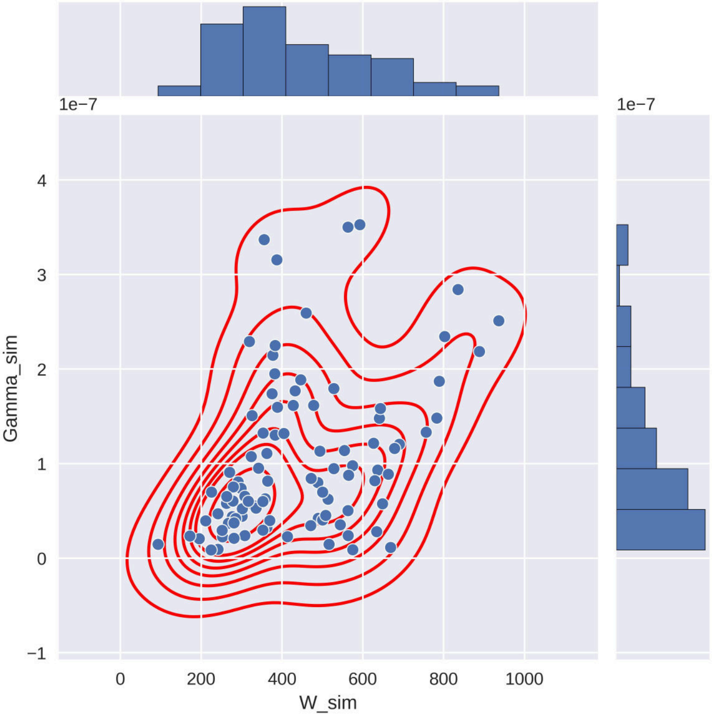

Figure 4.6: The plot displaying the joint distribution of DBM model parameters and their marginal distribution.

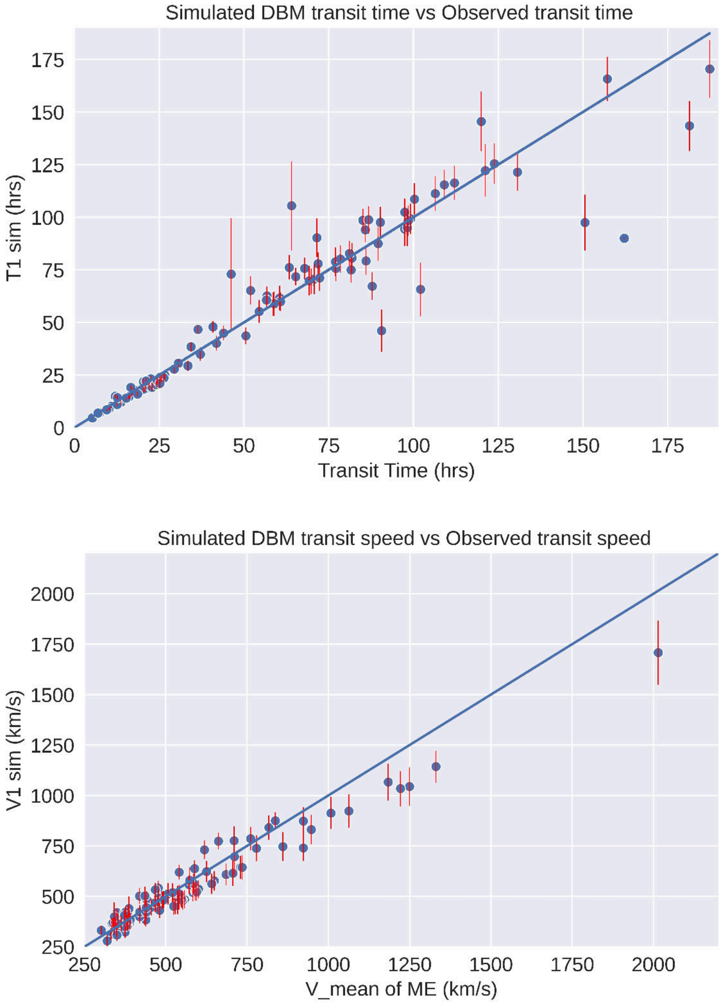

Figure 4.7: The plots showing P-DBM predicted arrival time and speed of ICME and their comparison with observations

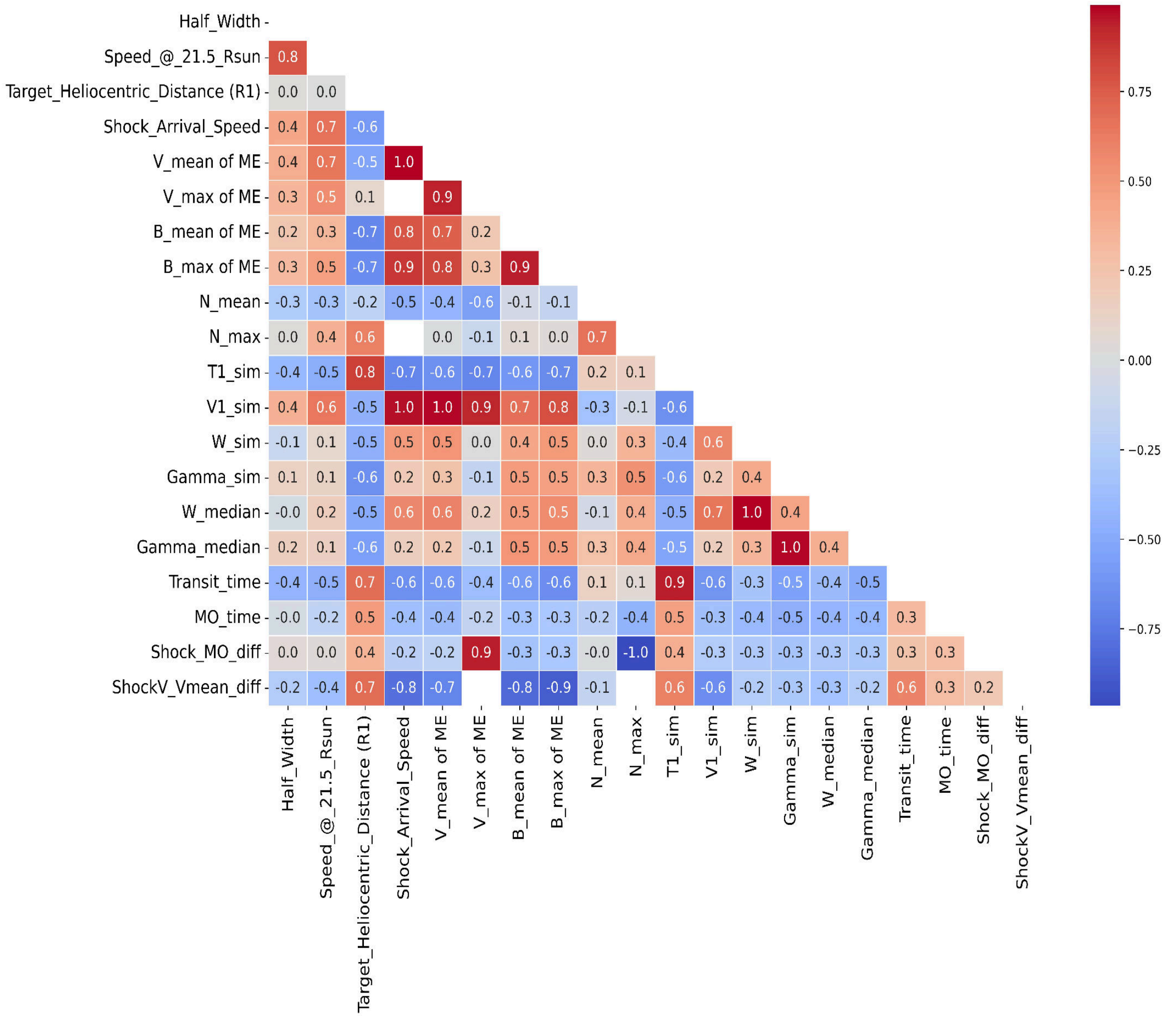

	Half_Width	Speed_@_21.5_Rsun	Target_Heliocentric_Distance (R1)	Shock_Arrival_Speed	V_mean of ME	V_max of ME	B_mean of ME	B_max of ME	N_mean	N_max	T1_sim	V1_sim	W_sim	Gamma_sim	W_median	Gamma_median	Transit_time	MO_time	Shock_MO_diff	ShockV_Vmean_diff
Half_Width																				
Speed_@_21.5_Rsun	0.8																			
Target_Heliocentric_Distance (R1)	0.0	0.0																		
Shock_Arrival_Speed	0.4	0.7	-0.6																	
V_mean of ME	0.4	0.7	-0.5	1.0																
V_max of ME	0.3	0.5	0.1		0.9															
B_mean of ME	0.2	0.3	-0.7	0.8	0.7	0.2														
B_max of ME	0.3	0.5	-0.7	0.9	0.8	0.3	0.9													
N_mean	-0.3	-0.3	-0.2	-0.5	-0.4	-0.6	-0.1	-0.1												
N_max	0.0	0.4	0.6		0.0	-0.1	0.1	0.0	0.7											
T1_sim	-0.4	-0.5	0.8	-0.7	-0.6	-0.7	-0.6	-0.7	0.2	0.1										
V1_sim	0.4	0.6	-0.5	1.0	1.0	0.9	0.7	0.8	-0.3	-0.1	-0.6									
W_sim	-0.1	0.1	-0.5	0.5	0.5	0.0	0.4	0.5	0.0	0.3	-0.4	0.6								
Gamma_sim	0.1	0.1	-0.6	0.2	0.3	-0.1	0.5	0.5	0.3	0.5	-0.6	0.2	0.4							
W_median	-0.0	0.2	-0.5	0.6	0.6	0.2	0.5	0.5	-0.1	0.4	-0.5	0.7	1.0	0.4						
Gamma_median	0.2	0.1	-0.6	0.2	0.2	-0.1	0.5	0.5	0.3	0.4	-0.5	0.2	0.3	1.0	0.4					
Transit_time	-0.4	-0.5	0.7	-0.6	-0.6	-0.4	-0.6	-0.6	0.1	0.1	0.9	-0.6	-0.3	-0.5	-0.4	-0.5				
MO_time	-0.0	-0.2	0.5	-0.4	-0.4	-0.2	-0.3	-0.3	-0.2	-0.4	0.5	-0.3	-0.4	-0.5	-0.4	-0.4	0.3			
Shock_MO_diff	0.0	0.0	0.4	-0.2	-0.2	0.9	-0.3	-0.3	-0.0	-1.0	0.4	-0.3	-0.3	-0.3	-0.3	-0.3	0.3	0.3		
ShockV_Vmean_diff	-0.2	-0.4	0.7	-0.8	-0.7		-0.8	-0.9	-0.1		0.6	-0.6	-0.2	-0.3	-0.3	-0.2	0.6	0.3	0.2	

Figure 4.8: The matrix displaying the correlation between observed properties of CME-ICME and P-DBM simulated results.

Chapter 5
Discussion and Conclusion

This chapter highlights the key findings and outcomes of this thesis. The chapter begins with a review of the geo-effective CME-ICME catalogue and its possible usefulness to the space weather community. Subsequently, a detailed discussion of the PDF for DBM parameters w and γ is given, along with an explanation of how it may be applied to the operational forecast. The significance of the CME-ICME lineup catalogue is briefly mentioned, and then a plan for the expansion of this lineup catalogue is outlined. The chapter closes with the presentation of a Python-based GUI for the P-DBM and future plans regarding validation.

The application of the P-DBM beyond 1 AU has demonstrated its utility in forecasting the arrival of CMEs across the heliosphere (discussed in Chapter 4). This thesis extends previous investigations by utilising a comprehensive catalogue of CME-ICME occurrences, resulting in a framework for enhancing prediction models at far distances from Earth. The findings given in this thesis emphasize the difficulties involved with implementing DBM in a dynamic, non-linear domain like the heliosphere, as well as how these issues might be handled to increase forecast accuracy.

5.1 P-DBM Application at 1AU

5.1.1 A Catalogue of Geo-effective CME-ICME properties

The CME-ICME dataset published by Napoletano et al. [2022] has been updated by integrating predicted DBM data, PDF fitting parameters, and other essential variables such as CME arrival time, speed, Dst index, source location, and the B$_z$ component. These factors are relevant to each CME-ICME event, resulting in a more comprehensive dataset. A subset of CME-ICME pairings that are well described by the DBM during their heliospheric propagation were identified by quantifying the success rate of the DBM inversion procedure. This categorization is essential for the space weather community since it provides insight into scenarios when the DBM forecast fails to reliably estimate CME transit times. Conversely, in CME occurrences where the DBM forecast is accurate, the model can provide valuable information regarding the parameters w and γ. Thus, CME-ICME pairs that do not align with the DBM approximation require further investigation, as it is difficult to tell if a 'no solution', a "suboptimal" or an "inadequate" label comes from a possible error in the initial CME-ICME association, insufficient details in the geometrical description of the ICME, or a phenomenon happening during the ICME propagation that cannot be described by the DBM (e.g., a CME-CME interaction). Investigating these aspects involves an in-depth analysis of each ICME, which is beyond the scope of the current investigation but might be addressed in future research. The updated CME-ICME dataset delivers further details, such as the solar wind conditions observed during CME propagation, parameters for verifying the DBM hypothesis, and information concerning acceleration or deceleration mechanisms. A summary of the improvements over the previous dataset from Napoletano et al. [2022] can be found in Table A.1. Making this catalogue a living one, which updates automatically after a certain time frame, is another important step toward cataloguing.

5.1.2 PDF for DBM Parameters

One of the key obstacles in heliospheric propagation of CMEs, is the variability of solar wind conditions across different regions. The drag experienced by CME is heavily influenced by the speed and density of the background solar wind, resulting in variations in CME deceleration as it travels through the heliosphere. This variability induces substantial errors in the prediction of CME arrival times and impact speeds, which the P-DBM framework aims to address through a probabilistic approach.

In addition to variability in solar wind speed and drag, both terms are practically unknown. Therefore, the subset of CME events that align with the DBM approximation can be used to extract the w and γ parameters through a Monte Carlo-style inversion procedure. Only CME events with an inversion process acceptance rate greater than 50% have been studied to establish sufficient confidence in DBM modelling of CME propagation. Importantly, these calculations do not take into account the cone geometry of CMEs; instead, the analysis is based on the one-dimensional version of the DBM. Future calculations could include improved versions of the DBM that consider different cone geometries, as detailed in Dumbović et al. [2021], Schwenn et al. [2005], by incorporating extra free variables in the DBM inversion process.

From 213 ICMEs, w and γ were successfully retrieved for 204 events, enabling to obtain robust statistics. The empirical PDF for solar wind speed w is modelled using two distinct distributions for slow and fast solar wind, with a threshold of $w = 500$ km/s to differentiate the two regimes. Previous studies, such as Dumbović et al. [2018], Dumbović et al. [2021], Napoletano et al. [2018, 2022], used a Gaussian distribution as the input PDF for w. In this study, the threshold of $w = 500$ km/s for fast solar wind speed makes the Gaussian distribution less applicable, and the Student's t-distribution emerges as a superior fit for most CME instances. This conclusion is further confirmed by PDF fitting for w using a single CME approach. In Figure 5.1, a histogram of the best-fitting PDFs for w in individual CMEs is presented. Although the Student's t-distribution exhibits bias due to the hard threshold, and the RSS metrics for both the Student's t-distribution and the Gaussian distribution are equivalent, the Gaussian PDF is eventually encouraged for the solar wind w in this study. The mean value for slow solar wind is $w_{\text{slow}} = 370$ km/s, with a standard deviation of 88 km/s, agreeing with Napoletano et al. [2022]. For fast solar wind, the mean value is $w_{\text{fast}} = 579 \pm 68$ km/s, which is slightly higher than previous studies. The median values are 386 km/s and 547 km/s for slow solar and fast solar wind respectively. The inversion method accepts extreme values, therefore these mean values differ slightly from the median values. For example, low values shift the mean of the slow solar wind speed to the left, whereas high values push the mean of the fast solar wind speed to the right. A comparison of solar wind speed values from various studies is provided in Table 3.2. Additionally, Table 5.1 lists the most probable values for solar wind speed under different conditions, including slow, fast, decelerating, and accelerating solar wind scenarios.

The choice of the PDF for the drag parameter γ has been a subject of discussion in prior studies, such as Napoletano et al. [2018], Napoletano et al. [2022], Dumbović et al. [2018], Dumbović et al. [2021], and Čalogović

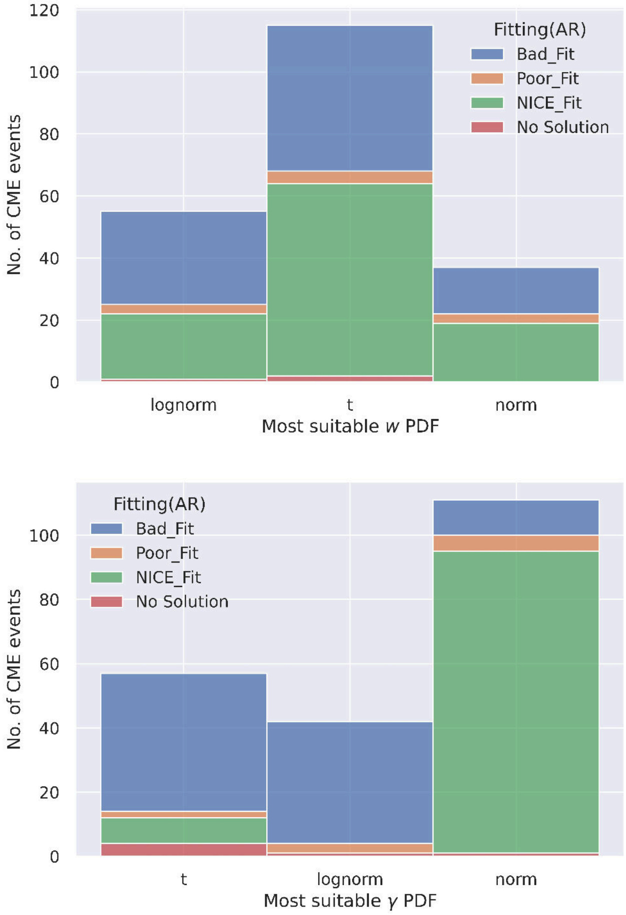

Figure 5.1: The histogram shows the optimal PDF for solar wind speed w and drag parameter γ in a single CME approach. Each PDF contains various types of CME events that are categorized and efficiently stacked on top of each other. Adapted from Mugatwala et al. [2024]

et al. [2021]. One group of researchers favours a lognormal distribution, while another group advocates for a Gaussian distribution as the input PDF for γ. In this study, we attempted to fit both distributions throughout the entire dataset as well as individual CME instances, getting insight into the preferences for these two distinct functions. From the results summarized in Table 3.3, it is evident that the lognormal distribution emerges as the most favourable PDF for γ across the full dataset, as it yields the lowest RSS among the competing PDFs. However, when estimating PDFs for specific CME events, the Gaussian distribution appears to be a superior fit. Figure 5.1 illustrates a histogram

	Slow	Fast	Decelerating	Accelerating
Solar wind speed w (km/s)				
Mean	371	579	409	503
Median	386	547	402	494
σ	89	68	118	56
drag parameter $\gamma(\times 10^{-7}\ \mathrm{km}^{-1})$				
Mean	0.86	1.26	0.93	1.59
Median	0.56	1.10	0.70	1.50
σ	0.74	0.73	0.76	0.58

Table 5.1: Statistical values for all CME occurrences marked as “Optimal Fit” were analyzed combined to produce drag parameter γ and ambient solar wind speed w using DBM inversion process. Adapted from Mugatwala et al. [2024]

of the most suitable PDFs for γ when analyzed on a per-event basis. The large magnitude and complexity of the dataset may account for this apparent discrepancy. Our dataset contains data spanning almost two solar cycles and a wide range of CME events, including different masses and cross-sections of CMEs. Consequently, the dataset records an extensive number of variations in solar wind density during the propagation of CMEs. Therefore, the long-tailed lognormal function works better when all of these parameters are taken into account when fitting a PDF to the complete dataset since γ is a measure of drag efficiency that is affected by several variables, including the mass and cross-section of the CME and the density of the solar wind [Vršnak et al., 2013]. The drag parameter γ obtained in this study is significantly higher In comparison to the values provided by Čalogović et al. [2021], Dumbović et al. [2021], and Dumbović et al. [2018]. The lognormal function’s extended tail can account for these increased values. Table 5.1 provides statistical measurements of the drag parameter γ. It is important to emphasize that the values in Table 5.1 should not be directly used as inputs for predicting ICME arrival time and speed using the DBM. To accurately predict ICME arrival time and speed, the values from Table 5.1 must be applied, following the transformation process detailed in Appendix A.5.

5.2 P-DBM Application beyond 1AU

5.2.1 CME-ICME Lineup Event Catalogue

The CME-ICME Lineup catalogue, which was created for this thesis, has been essential in evaluating the predictive ability of the P-DBM. Through careful curation of a dataset, this catalogue establishes a connection between in-situ ICME measurements and their corresponding solar source CMEs. This makes it possible to compare in situ measurements of ICME parameters with CME kinematics obtained from remote sensing data, providing insight into the evolution of CMEs as they move through various regions of the heliosphere.

On the complete opposite side, this kind of catalogue provides opportunities to refine the ICME propagation models, hence enhancing the reliability of forecast models. For example, PDF for DBM parameters can be obtained for different heliocentric distance ranges and implementing them in DBM calculation can partially remove the constant w approximation. Additionally, it also provides an opportunity to investigate the radial evolution in ICME properties, which opens a window for the new model development.

The catalogue curated as a part of this thesis is in its very early stage, and significant improvements have to be made in future. One major improvement is the inclusion of as many as possible ICME data sources. Additionally, novel methods have to be invented to make cataloguing more efficient and minimize human intervention. Also, the analysis scheme has to be determined to consider both radial and longitudinal evolution of ICME properties. The recent developments in AI/ML based ICME prediction models can also significantly benefit from the catalogues prepared by this model. The Bayesian approach has been implemented on the catalogued prepared by us to determine the PDFs of P-DBM parameters [Chierichini et al., 2024]. Additionally, physics-informed neural networks are developed using P-DBM and the prior version of the catalogue [Guastavino et al., 2023, Dani et al., 2022]

5.2.2 P-DBM GUI

The P-DBM's potential for operational space weather forecasting is shown by its ability to accurately anticipate the arrival times of ICMEs at various spacecraft locations across the heliosphere. Additionally, the dynamic nature of DBM input parameters allows to integrate various CME morphological models such as Ellipse Evolution with Heliospheric Imager (ELEvoHI) [Rollett et al., 2016, Möstl et al., 2015], GCS [Thernisien et al., 2006, Thernisien, 2011] seamlessly into the model. Furthermore, the value of free parameters of DBM offered by various studies could be useful to predict ICME arrival time. Therefore, a python-based GUI is also being developed to ease the calculation and visualization of results obtained through P-DBM. This GUI gives control over each parameter that P-DBM needs as an input, along with this traditional approach GUI also contains various features to minimize the human intervention to make the prediction more efficient. 5.2.2 represents the boundary condition file that has been created for the input of P-DBM calculation. Where the initial condition for the CME kinematics has to be provided by a user. Later, the user-provided DBM free parameters are recorded, but in the case of "$Auto\_DBM\_Parametrs$" : $true$, the user-given values are neglected, and the PDF obtained in Mugatwala et al. [2024] is used for calculation. The other parameters have the usual meaning that has been discussed in the thesis. The boundary condition files show the dynamic behaviour of the GUI where a semi-automatic approach has been implemented. Additionally, GUI's ability to link with any other module can make it a prominent candidate for operational space weather forecast modules. The working version 1.0 of this GUI is publicly avilable and access by the user through `https://github.com/astronish16/P-DBM-GUI`. In the future, a web app for this GUI will also be created so that users can perform P-DBM simulations easily through an active internet connection from anywhere in the world. Also, more features may be integrated into the GUI for better analysis of ICME prediction. Figuure 5.3 is user interface window of the GUI showing input and output area for the model calculation. Figure 5.2 is the output provided by the GUI that helps in the visualization of the ICME propagation in the heliosphere.

```
{
"Event_Date": "2020-12-31 16:17",
"Possible_Event_delay": 3600.0,
"Initial_Position": 21.5,
"Error_Initial_Position": 1.0,
"Initial_Speed": 1000.0,
"Error_Initial_Speed": 100.0,
"Solar_wind_Speed": 400.0,
"Error_Solar_wind_Speed": 50.0,
"Drag_Parameter": 0.2e-7,
"Error_Drag_Parameter": 0.1e-7,
"Auto_DBM_Parameters": true,
"Wind_Type": "Slow",
"2D_CONE_DBM": false,
"Half_Width_CME": 30.0,
"Error_Half_Width_CME": 10.0,
"CME_Propagation_Direction": 30.0,
"Error_CME_Propagation_Direction": 5.0,
"Slef_Similar_Expansion": false,
"Flattening_Cone_Expansion": true,
"P-DBM": true,
"Number_of_Runs": 1000,
"Plots": true,
"Target": "Earth",
"Inner_Planets": ["Mercury","Venus","Earth","Mars"],
"Outer_Planets": ["Jupiter","Saturn","Uranus","Neptune"],
"Space_Crafts": ["Messenger","VEX","PSP","SolO","BepiCol","
    Spitzer","Wind",     "ST-A","ST-B","Kepler","Ulysses","MSL","
    Maven","Juno"]
}
```

Listing 5.1: Snippet of Boundary condition file created as an input for the P-DBM calculation

5.3 Validation and Benchmark Comparison

The catalogue of geo-effective CME events serves as the basis for determining the PDFs of P-DBM's parameter [Mugatwala et al., 2024]. Two distinct solar wind speed PDFs, classified based on a critical value of 500 km/s, are employed as P-DBM input to predict CME arrival time at L1 point. At this stage, a rigorous validation and benchmarking procedure is essential to ensure

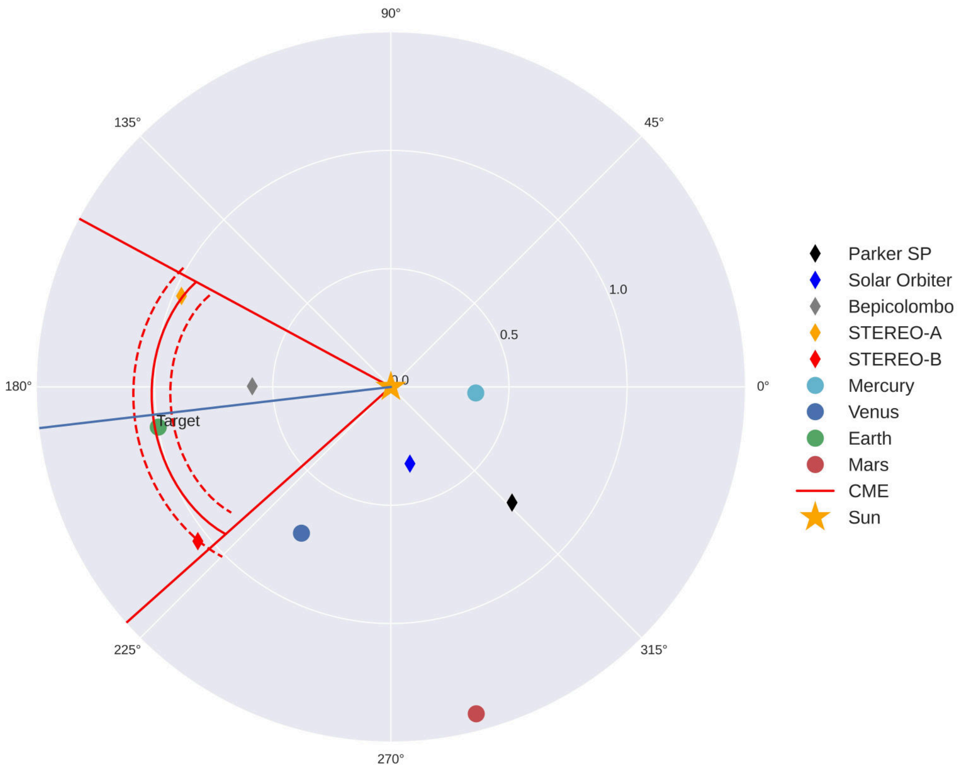

Figure 5.2: The simulated ICME edge at the time of arrival at the target using P-DBM is illustrated. The red solid line represents the ICME edge associated with the mean value of ICME arrival time. On the other hand, the dashed line indicates the uncertainty in the forecast.

the reliability of the obtained PDFs in the P-DBM application. In future, validation will be performed using a set of CME-ICME events which are not considered in the process to obtain those PDFs. Benchmarking efforts will involve comparing the predicted CME arrival times against the observed ones. The established skill scores such as probability of Detection (POD), Success Ratio (SR), MAE and others will be used against the existing state-of-the-art models such as EUHFORIA, WSA-ENLIL + cone, ELEvoHI, to evaluate the relative performance of the model [Verbeke et al., 2019]. Through community-agreed metrics and validation methods, we plan to enhance model credibility and contribute to the continuous improvement of operational space weather forecasting capabilities. Appendix A.7 summarises the various community agreed metrics and skill scores for CME arrival predictions.

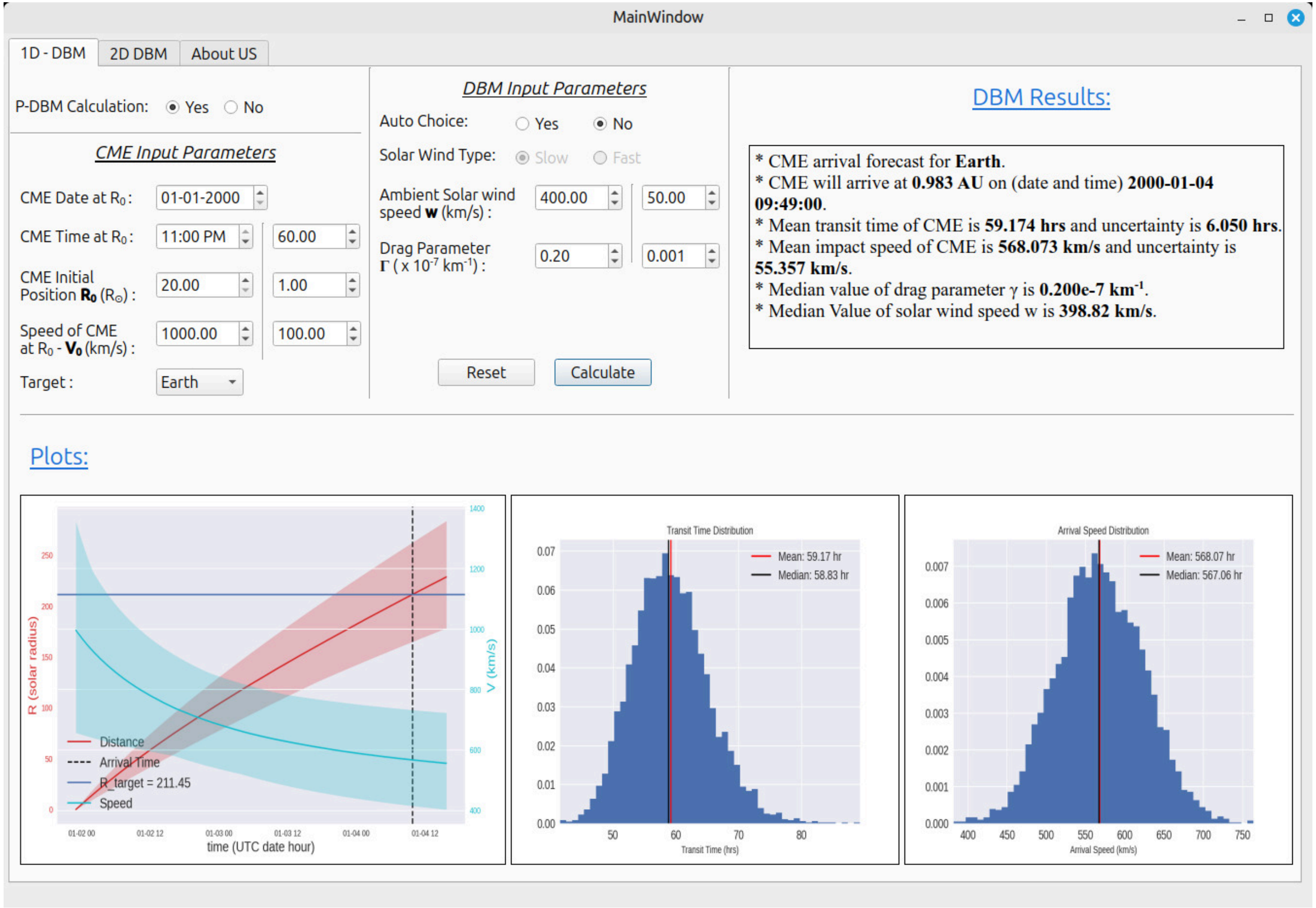

P-DBM Calculation: ● Yes ○ No

CME Date at R₀: 01-01-2000

CME Time at R₀: 11:00 PM 60.00

CME Initial Position $\mathbf{R_0}$ ($R_\odot$): 20.00 1.00

Speed of CME at R₀ - $\mathbf{V_0}$ (km/s): 1000.00 100.00

Target: Earth

Auto Choice: ○ Yes ● No

Solar Wind Type: ● Slow ○ Fast

Ambient Solar wind speed **w** (km/s): 400.00 50.00

Drag Parameter Γ ($\times 10^{-7}$ km^{-1}): 0.20 0.001

* CME arrival forecast for **Earth**.
* CME will arrive at **0.983 AU** on (date and time) **2000-01-04 09:49:00**.
* Mean transit time of CME is **59.174 hrs** and uncertainty is **6.050 hrs**.
* Mean impact speed of CME is **568.073 km/s** and uncertainty is **55.357 km/s**.
* Median value of drag parameter γ is **0.200e-7 km^{-1}**.
* Median Value of solar wind speed w is **398.82 km/s**.

Figure 5.3: A window of P-DBM GUI showing the input form and output pane for the one dimension P-DBM.

Chapter A

Appendix

A.1 Derivation of analytical solution for DBM equation

Intergration Rule

$$I = \int \frac{dx}{ax^2 + bx + c} = \frac{2}{\sqrt{4ac - b^2}} \arctan\left(\frac{2ax+b}{\sqrt{4ac-b^2}}\right) + C \tag{A.1}$$

Step-1: Completing a square

A quadratic expression $ax^2 + bx + c$ can be written as:
$ax^2 + bx + c = a\left(x + \frac{b}{2a}\right)^2 + \frac{4ac-b^2}{4a}$

Step-2: Substitution

Let's substitute $x + \frac{b}{2a} = t$ and $\frac{4ac-b^2}{4a} = u$ then $dx = dt$.
The integral becomes $\int \frac{dt}{at^2+u}$.

Step-3: Simplifying the integral to standard form:

Factor out the a, $\int \frac{dt}{at^2+u} = \frac{1}{a} \int \frac{dt}{t^2+\frac{u}{a}}$.
The $\int \frac{dx}{x^2+p^2} = \frac{1}{p} \arctan \frac{x}{p} + C$ is standard integral form and therefore above integration becomes
$\frac{1}{a} \int \frac{dt}{t^2+\frac{u}{a}} = \frac{1}{\sqrt{au}} \arctan\left(\frac{t}{\sqrt{\frac{u}{a}}}\right) + C.$

Step-4: Substitute back

Now, substitute back the value of t and u. The final integration will be as shown in equation A.1.

⊙ **Special Case:**

when $4ac - b^2 = 0$, the substitution $u = 0$ and therefore integral from step-2 becomes another standard form
$\int \frac{dt}{at^2} = \frac{1}{a} \int \frac{dt}{t^2} = -\frac{1}{at} + C$.
In this special case, the equation A.1 simplifies to:

$$I = \int \frac{dx}{ax^2 + bx + c} = -\frac{2}{b + 2ax} + C \tag{A.2}$$

The equation of motion under DBM approximation is,

$$a(r) = -\gamma \times \Big(v(r) - w\Big) \times |v(r) - w| \tag{A.3}$$

consider $a = \frac{d^2r}{dt^2}$ and $v = \frac{dr}{dt}$ and initial conditions for equation at $t = 0$ are $r(0) = r_0$ and $\dot{r}(0) = v_0$

Case-1: $v > w$
with the mentioned consideration, the equation A.3 becomes,

$$\ddot{r} = -\gamma \times (\dot{r} - w)(\dot{r} - w)$$
$$\ddot{r} + \gamma \dot{r}^2 - 2\gamma \dot{r} w + \gamma w^2 = 0$$

Let's substitute, $-2w\gamma = P$ and $\gamma w^2 = Q$, so differential equation will be:

$$\ddot{r} + \gamma \dot{r}^2 + P\dot{r} + Q = 0 \tag{A.4}$$

consider $\dot{r} = A \implies \ddot{r} = \dot{A}$. Therefore, the boundary condition becomes $A = v_0$ at $t = 0$

$$\frac{dA}{dt} + \gamma A^2 + PA + Q = 0$$

using a method of variable separation reduces the equation as follows:

$$\frac{dA}{\gamma A^2 + PA + Q} = -dt$$
$$\int \frac{dA}{\gamma A^2 + PA + Q} = -\int dt$$

The integration solution can be found using equation A.2.

$$\frac{2}{2\gamma A + P} = t + K \tag{A.5}$$

where K is an arbitrary constant. The value of K can be found using the new boundary condition, i.e., $A = v_0$ at $t = 0$ in equation A.5.

$$\frac{2}{2\gamma v_0 + P} = K \tag{A.6}$$

Substituting the value of A in equation A.5 will make the equation a first-order differential equation as follows:

$$2\gamma \frac{dr}{dt} + P = \frac{2}{t + K} \tag{A.7}$$

Integrating the equation A.7 with t gives a solution:

$$2\gamma r + Pt = 2 \ln |t + K| \ + M \tag{A.8}$$

where M is another arbitrary constant. The value of M can be found using the initial condition, i.e., $r = r_0$ at $t = 0$ in equation A.8.

$$M = 2\gamma r_0 - 2 \ln |k| \tag{A.9}$$

Now, substituting equation A.9 in equation A.8 and rewriting it will make the equation more readable.

$$r = \frac{1}{\gamma} \ln |\frac{t + K}{K}| \ - \frac{Pt}{2\gamma} + r_0 \tag{A.10}$$

Now $\frac{t+K}{K} = 1 + \frac{t}{K}$ and substituting equation A.6 in here will make the equation more readable $\frac{t+K}{K} = 1 + \gamma(v_0 - w)t$. Substituting all values in Equation A.10 and A.7 gives the solution of DBM equation of motion:

$$r = \frac{1}{\gamma} \ln |1 + \gamma(v_0 - w)t| \ + wt + r_0 \tag{A.11}$$

$$v = \frac{v_0 - w}{1 + \gamma(v_0 - w)t} + w \tag{A.12}$$

Case-2: $v < w$

In this case, equation A.3 can be rewritten as:

$$\ddot{r} - \gamma \dot{r}^2 + 2\gamma w \dot{r} - \gamma w^2 = 0 \tag{A.13}$$

and we substitute $P = 2\gamma w$ and $Q = -\gamma w^2$. Solving the equation the same as above will give a solution to the DBM equation of motion as follows:

$$r = -\frac{1}{\gamma} \ln |1 - \gamma(v_0 - w)t| \ + wt + r_0 \tag{A.14}$$

$$v = \frac{v_0 - w}{1 - \gamma(v_0 - w)t} + w \tag{A.15}$$

A.2 Derivation of geometrical relation of cone geometry for ICMEs

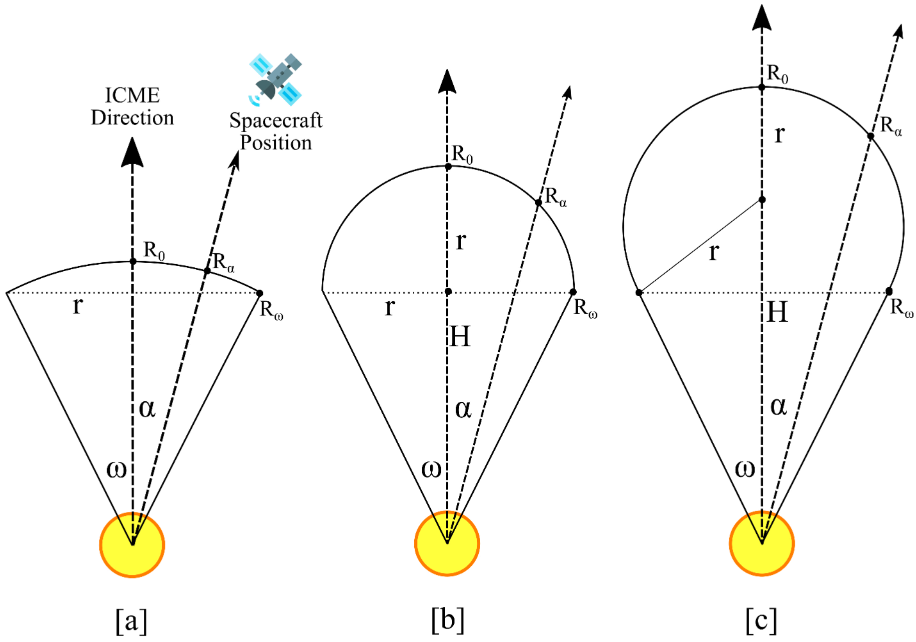

Figure A.1: A schematic of three options of the ICME cone geometry. [Reproduced from Schwenn et al. [2005]]

<u>Case-a</u>:

In this geometry, the ICME leading edge is assumed to be a circular arc that is concentric with the solar surface. In this case, the off-centred element of ICME leading edge has the same heliocentric distance as CME apex point. Therefore,

$$R_\alpha = R_0 = R_\omega$$

Case-b:

In this geometry, the ICME leading edge is considered as a semi-circle that spans the total angular width 2ω of ICME.

For the geometric relations of the cone shape, consider $\triangle OAC$ and $\triangle OAB$. These two triangles are connected with constraints of $\overline{\mathrm{AB}} \perp \overline{\mathrm{OC}}$. From $\triangle OAB$ and $\triangle OAD$ it is clear that,

$$\sin\alpha = \frac{AB}{H} \implies AB = H\sin\alpha \tag{A.16}$$

$$\cos\alpha = \frac{OB}{H} \implies OB = H\cos\alpha \tag{A.17}$$

$$\tan\omega = \frac{r}{H} \implies r = H\tan\omega \tag{A.18}$$

Applying Pythagoras' theorem on $\triangle ABC$ and putting the above equation in there provides us,

$$BC^2 = AC^2 - AB^2 = r^2 - (H\sin\alpha)^2 \tag{A.19}$$

$$BC = \sqrt{r^2 - (H\sin\alpha)^2} \tag{A.20}$$

From the Figure A.1[b], Equations A.18, A.17 and A.20, it is easy to obtain,

$$R_0 = H + r = H + H\tan\omega = H\,(1+\tan\omega) \tag{A.21}$$

$$R_\alpha = OB + BC = H\cos\alpha + \sqrt{r^2 - (H\sin\alpha)^2} \tag{A.22}$$

$$= H\cos\alpha + \sqrt{(H\tan\omega)^2 - (H\sin\alpha)^2} \tag{A.23}$$

$$= H\left[\cos\alpha + \sqrt{\tan^2\omega - \sin^2\alpha}\right] \tag{A.24}$$

$$R_\alpha = R_0\frac{\cos\alpha + \sqrt{\tan^2\omega - \sin^2\alpha}}{1+\tan\omega} \tag{A.25}$$

The Equation A.25 is a relationship between the heliocentric distance of the ICME apex R_0 and an element located at the angle α, R_α. A time derivative of Equation A.25 provides a similar relationship for the speed.

$$V_\alpha = V_0 \frac{\cos\alpha + \sqrt{\tan^2\omega - \sin^2\alpha}}{1 + \tan\omega} \tag{A.26}$$

Note: In this geometry maximum possible value of $\omega = 90°$. And this situation is equivalent to case-a. Also, when $\omega \geq 90°$ then semi-circular ICME leading edge is not possible and hence it will lead to only possible situation which is case-a.

Case-c:

In this geometry, the ICME leading edge is assumed to be a circular arc that is tangentially connected to the CME leg. Due to this consideration, $\angle ODA = 90°$ and therefore

$$\sin\omega = \frac{r}{H} \implies r = H\sin\omega \tag{A.27}$$

For the geometric relation of this cone shape, The calculation up to equation A.23 remain the same and the only difference in the final transformation will come from the equation A.27.

$$R_\alpha = OB + BC = H\cos\alpha + \sqrt{r^2 - (H\sin\alpha)^2} \tag{A.28}$$

$$= H\cos\alpha + \sqrt{(H\sin\omega)^2 - (H\sin\alpha)^2} \tag{A.29}$$

$$= H\left[\cos\alpha + \sqrt{\sin^2\omega - \sin^2\alpha}\right] \tag{A.30}$$

$$R_\alpha = R_0 \frac{\cos\alpha + \sqrt{\sin^2\omega - \sin^2\alpha}}{1 + \sin\omega} \tag{A.31}$$

The equation A.31 relate the off-centered element of the ICME leading edge with the CME apex point. The time derivative of equation A.31 connects the speed of off-centered point with the apex.

$$V_\alpha = V_0 \frac{\cos\alpha + \sqrt{\sin^2\omega - \sin^2\alpha}}{1 + \sin\omega} \tag{A.32}$$

Note: Since the conical leg has to be tangential to the circular arc then for $\triangle OAD$ has to follow the constraint $\omega + \angle A = 90°$. Also, the feasible solution of the equation A.31 is only possible if $\sin^2\omega \geq \sin^2\alpha$. This condition will only satisfy if $\omega < 90°$ as *sine* function is decreasing function in second quadrant. For $\omega \geq 90°$, this geometry transformed to the case-a.

A.3 DBM inversion procedure

If ICME follows the DBM and its boundary conditions namely - initial position r_0, speed at initial position v_0, TOA t_{1AU} and impact speed v_{1AU} at 1 AU are known, the free parameters of the model w and γ can be determined through mathematical inversion of the Equations 3.5 and 3.4.

$$\frac{(v_0 - w)(v_{1AU} - w)t_{1AU}}{(v_0 - v_{1AU})} \ln\left[\frac{(v_0 - v_{1AU})}{(v_{1AU} - w)} + 1\right] + wt_{1AU} + r_0 - r_{1AU} = 0. \tag{A.33}$$

$$\gamma = \frac{(v_0 - v_{1AU})}{(v_0 - w)(v_{1AU} - w)t_{1AU}}. \tag{A.34}$$

The so-called DBM inversion procedure mentioned here and throughout the thesis is the reverse modelling of DBM.

A.4 Description of Revised Geo-effective CME-ICME List

Table A.1: Column description of the dataset that has been created for this study. Adopted from Mugatwala et al. [2024]

Name	**Keyword**	**Description**	**Source**
LASCO Start	LASCO _Start	First CME appearance in LASCO C2/C3 coronagraphs	LASCO CDAW 2.6.1
Start Date	Start_Date	Time when CME reaches to 20 R$\odot$	Napoletano et al. [2022]
Arrival Date	Arrival_Date	Estimated arrival time of ICME using insitu signatures	R & C 2.7.1

(Continued)

Name	**Keyword**	**Description**	**Source**
Plasma Event Duration	PE_duration	End of ICME plasma signatures after col 3 is recorded	R & C
Arrival Speed	Arrival_v	ICME arrival speed at L1 (km/s)	R & C
Transit Time	Transit_time	(hrs) Computed between col 1 and col 3	Napoletano et al. [2022]
Transit Time Error	Transit_time _err	(hrs) Error associated to the start date of CME	Napoletano et al. [2022]
LASCO date	LASCO _Date	Most likely associated CME observed by LASCO	LASCO CDAW
LASCO speed	LASCO_v	(km/s) speed correspond to the fastest moving point of CME in LASCO FOV	LASCO CDAW
Position Angle	LASCO_pa	(deg) Counterclockwise (from solar North) angle of appearance into coronographs	LASCO CDAW
Angular Width	LASCO_da	(deg.) Angular expansion of CME into coronographs	LASCO CDAW
Halo	LASCO_halo	If LASCO_da is >270° then 'FH' (full halo), if >180° 'HH' (half halo), if >90° 'PH'(partial halo), otherwise 'NO	LASCO CDAW
De-Projected Speed	v_r	(km/s) De-projected CME speed	Napoletano et al. [2022]
De-Projected Speed Error	v_r_err	(km/s) Uncertainty of CME initial speed	Napoletano et al. [2022]
Theta Source	Theta_source	(arcsec) Longitude of the most likely source of CME	Napoletano et al. [2022]

(Continued)

Name	**Keyword**	**Description**	**Source**
Phi Source	Phi_source	(arcsec) Co-latitude of the most likely source of CME	Napoletano et al. [2022]
Source POS error	source_err	(deg.) Uncertainty of the most likely CME source	Napoletano et al. [2022]
POS source angle	POS_source _angle	(deg.) Principal angle of the most likely CME source	Napoletano et al. [2022]
Relative width	rel_wid	(rad.) De-projected width of CME	Napoletano et al. [2022]
Mass	Mass	(gm) Estimated CME Mass	LASCO/ CDAW
Solar Wind Type(CH)	SW_type	Solar wind (slow, S, or fast, F) interacting with the ICME based on the presence of coronal hole near CME location	Napoletano et al. [2022]
Bz	Bz	(nT) z-component of magnetic field at L1 and CME arrival time	R & C
Dst	DST	Geomagnetic Dst index recorded at CME arrival	R & C
Statistical de projected speed	v_r_stat	(km/s) Statistical de-projected CME speed, that is, $v\_r\_stat = LASCO\_v * 1.027 + 41.5$	
Acceleration	Accel.	(m/s 2) Residual acceleration at last CME observation	Napoletano et al. [2022]
Analytical Wind	Analyitic_w	(km/s) solar wind from DBM exact inversion	Napoletano et al. [2022]

(Continued)

Name	**Keyword**	**Description**	**Source**
Analytical gamma	Analyitic _gamma	(km^{-1}) drag parameter, γ, from DBM exact inversion	Napoletano et al. [2022]
Transit Time (Simulated)	T1_Sim	(hrs) Transit time calculated using P-DBM	Mugatwala et al. [2024]
Transit Time error (Simulated)	T1_Sim_err	(hrs) error associated with transit time in P-DBM	Mugatwala et al. [2024]
Impact Speed (Simulated)	V1_Sim	(km/s) calculated CME arrival speed using P-DBM	Mugatwala et al. [2024]
Impact Speed error (Simulated)	V1_Sim_err	(km/s) error associated with arrival speed in P-DBM	Mugatwala et al. [2024]
Solar Wind Speed	W_Sim	(km/s) Mean value of solar wind speed from inversion procedure	Mugatwala et al. [2024]
Solar Wind Speed Error	W_Sim_err	(km/s) Standard deviation of solar wind speed from inversion procedure	Mugatwala et al. [2024]
Gamma Simulated	Gamma_Sim_s	(km^{-1}) 's' parameter for lognormal PDF	Mugatwala et al. [2024]
Gamma Error Simulated	Gamma_Sim _loc	(km^{-1}) $'loc'$ parameter for lognormal PDF	Mugatwala et al. [2024]
Gamma Simulated (log)	Gamma_Sim _scale	$'scale'$ parameter for lognormal PDF	Mugatwala et al. [2024]
Optimal Transit Time	T1_opt	Minimally deviated transit time compared to observed one	Mugatwala et al. [2024]

(Continued)

Name	Keyword	Description	Source
Optimal Impact Speed	V1_opt	V1 correspond to T1_opt	Mugatwala et al. [2024]
Optimal W	W_opt	W correspond to T1_opt	Mugatwala et al. [2024]
Optimal gamma	Gamma_opt	gamma correspond to T1_opt	Mugatwala et al. [2024]
Optimal V_r	V_r_opt	V_r correspond to T1_opt	Mugatwala et al. [2024]
W CI min	W99_min	minimum value of 99% confidence interval for w	Mugatwala et al. [2024]
W CI max	W99_max	maximum value of 99% confidence interval for w	Mugatwala et al. [2024]
Gamma CI min	Gamma99_min	minimum value of 99% confidence interval for gamma	Mugatwala et al. [2024]
Gamma CI max	Gamma99 _max	maximum value of 99% confidence interval for gamma	Mugatwala et al. [2024]
CME Type (V_r_opt)	CME_type	CME type based on W_sim (Accelerating/ Decelerating)	Mugatwala et al. [2024]
CME Type (V_r)	CME_type_v0	CME type based on W_opt (accelerating: A/ decelerating D)	Mugatwala et al. [2024]
Solar wind Type (Wth)	Wind_type	Solar wind (based on threshold value) interacting with ICME	Mugatwala et al. [2024]

(Continued)

Name	**Keyword**	**Description**	**Source**
Target distance	R1(AU)	(AU) Sun-Earth Distance at CME start date (Col2)	Mugatwala et al. [2024]
Fitting	Fitting(AR)	Goodness of Inversion procedure: Optimal / Suboptimal / Inadequate	Mugatwala et al. [2024]
Acceptance Rate	Acceptance _Rate	Acceptance rate of inversion procedure	Mugatwala et al. [2024]
Best W PDF	Best_fit_W	Most suitable PDF for W	Mugatwala et al. [2024]
Best gamma PDF	Best_fit _gamma	Most suitable PDF for gamma	Mugatwala et al. [2024]

A.5 Lognormal Distribution - Comparative description

To estimate the parameters of a lognormal PDF, we utilized the Python package *distfit* [Taskesen, 2023], which depends on *SciPy* [Virtanen et al., 2020]. The standard lognormal function is defined as:

$$f(x,s) = \frac{1}{sx\sqrt{2\pi}} \exp(\frac{-\ln^2 x}{2s^2}). \tag{A.35}$$

SciPy adds two parameters, *loc* and *scale*, to shift and scale the distribution: The new function with these two additional parameters will be:

$$f(x,s,loc,scale) = \frac{f(y,s)}{scale}, \quad where\, y = \frac{x-loc}{scale} \tag{A.36}$$

When a variable X follows a normal distribution with parameters μ and σ, the lognormal variable $Y = exp(X)$ has $\mu = \ln(scale)$ and $\sigma = s$. The resulting form will be:

$$
\begin{aligned}
f(x,s,loc,scale) &= \frac{1}{sy\sqrt{2\pi}}\frac{\exp(\frac{-\ln^2 x}{2s^2})}{scale} \\
&= \frac{1}{s(\frac{x-loc}{scale})\sqrt{2\pi}}\frac{1}{scale}\exp\left(\frac{-\ln^2(\frac{x-loc}{scale})}{2s^2}\right) \\
&= \frac{1}{s(x-loc)\sqrt{2\pi}}\exp\left(\frac{-\big(\ln(x-loc)-\ln(scale)\big)^2}{2s^2}\right)
\end{aligned}
$$

$$
f(x,s,loc,scale) = \frac{1}{s(x-loc)\sqrt{2\pi}}exp\left[-\left(\frac{(ln(x-loc)-\mu)}{\sqrt{2}s}\right)^2\right], \tag{A.37}
$$

while a lognormal function used by Napoletano et al. [2018] is

$$
f(x,) = \frac{1}{s\sqrt{2\pi}}exp\left[-\left(\frac{(lnx-\mu)}{\sqrt{2}s}\right)^2\right]. \tag{A.38}
$$

A.6 Description of Lineup Catalogue

Table A.2: Description of the CME-ICME Lineup list.

Keyword	Description	Source
Event_No	To which lineup event the row belongs. Also includes a keyword for the parent paper from which the ICME event has been taken (e.g., Winslow_1, Zaho_1, Helio4cast_1).	
CME_Launch _Date_and_Time	CME launch date and time.	DONKI
ICME_dataset_id	ID from corresponding ICME data source for lookup.	R&C, DONKI [Möstl et al., 2022]
Detecting_ Spacecraft	Spacecraft in which CME was first observed in a coronagraphic image (A: STEREO-A, B: STEREO-B, C: SOHO/LASCO).	DONKI

Keyword	**Description**	**Source**
CDAW_Label	Halo / Partial Halo classification from the SOHO/LASCO CME catalogue.	CDAW
Longitude	CME longitude derived using the cone model (Stonyhurst coordinate system).	DONKI
Latitude	CME latitude derived using the cone model (Stonyhurst coordinate system).	DONKI
Half_Width	Half width of the CME cone.	DONKI
Date_and_Time _@_21.5_Rsun	Timestamp when CME reaches 21.5 solar radii.	DONKI
Speed_@_ 21.5_Rsun	Speed of CME at 21.5 solar radii (km/s).	DONKI
Targets	Planet or spacecraft experiencing CME disturbance.	This work
Category	Type of target (planet or spacecraft).	This work
Target_Longitude	Position of target in ecliptic plane (JPL Horizon system).	This work
Target_Heliocentric _Distance	Distance of target from the Sun (AU).	This work
Nearby_Planet_ Orbit	Closest planetary orbit to the target.	This work
Shock_Arrival_ Datetime	Time when shock is observed in in-situ measurement.	Möstl et al. [2022], R&C
Shock_Arrival_ Speed	Plasma speed measured in in-situ observation when shock is identified (km/s).	Möstl et al. [2022]
ME_Arrival_ Datetime	Timestamp corresponding to magnetic ejecta identification.	Möstl et al. [2022], Winslow et al. [2015], Zhao and Dryer [2014], R&C

Keyword	**Description**	**Source**
ME_End_Datetime	Timestamp marking the end of magnetic ejecta passage.	Möstl et al. [2022], Winslow et al. [2015], Zhao and Dryer [2014], R&C
V_mean_of_ME	Mean arrival speed of magnetic ejecta (km/s).	Möstl et al. [2022], Winslow et al. [2015], Zhao and Dryer [2014], R&C
V_max_of_ME	Maximum speed of magnetic ejecta (km/s).	Möstl et al. [2022]
B_mean_of_ME	Mean total magnetic field in the ejecta (nT).	Möstl et al. [2022]
B_max_of_ME	Maximum total magnetic field in the ejecta (nT).	Möstl et al. [2022]
N_mean	Mean proton density during magnetic ejecta passage (cm^{-3}).	Möstl et al. [2022]
N_max	Maximum proton density during magnetic ejecta passage (cm^{-3}).	Möstl et al. [2022]
P_dy_mean	Mean proton dynamic pressure during ejecta time (nPa).	Möstl et al. [2022]
P_dy_max	Maximum proton dynamic pressure during ejecta time (nPa).	Möstl et al. [2022]
T1_sim	Transit time from P-DBM model (hours).	This work
T1_sim_err	Uncertainty in transit time from P-DBM (hours).	This work
V1_sim	Arrival speed from P-DBM model (km/s).	This work

Keyword	**Description**	**Source**
V1_sim_err	Uncertainty in arrival speed from P-DBM (km/s).	This work
W_sim	Mean solar wind speed from DBM inversion (km/s).	This work
W_sim_err	Uncertainty in mean solar wind speed (km/s).	This work
Gamma_sim	Drag efficiency in P-DBM (km^{-1}).	This work
Gamma_sim_err	Uncertainty in drag efficiency (km^{-1}).	This work
T1_opt	Least deviated P-DBM transit time (hours).	This work
V1_opt	Least deviated P-DBM arrival speed (km/s).	This work
W_opt	Solar wind speed in P-DBM for T1_opt (km/s).	This work
Gamma_opt	Drag parameter in P-DBM for T1_opt (km^{-1}).	This work
Acceptance_Rate	Acceptance rate in DBM inversion.	This work
W_median	Median solar wind speed in DBM inversion (km/s).	This work
Gamma_median	Median drag parameter in DBM inversion (km^{-1}).	This work
Notes_for_Events	Notes and comments on CME-ICME events.	This work

A.7 Validation Metrics

The metrics for CME arrival prediction assessment are generally categorised into two parts.

1. The so-called contingency table and derived basic skill scores, which focuses on all modelled CME events, including those that do not arrive at target. (See: Figure A.2 for contingency table and Table A.3 for the various skill score)
2. Metrics specifically related to hits, where both the observed and predicted CME arrivals are correctly identified.

	Observed Arrival	No Observed Arrival
Predicted Arrival	Hit (H)	False Alarm (FA)
No Predicted Arrival	Miss (M)	Correct Rejection (CR)

Figure A.2: The contingency table describing categorical forecast of CME arrival/nonarrival. In context to CME arrival: Hit (H): Predicited CME arrival is also observed. False Alarm (FA): CME arrival is predicted but it is not observed. Miss (M): Observed CME arrival is not predicted. Correct Rejection (CR): CME arrival is neither predicted nor observed. The green colour denotes the correct prediction, while red stands for negative prediction. Credit: Verbeke et al. [2019]

Table A.3: Various skill scores derived from contingency table (Figure A.2) and its description. Adapted from: Verbeke et al. [2019]

Skill Score	**Formula**	**Perfect Score**	**Description**
Hit Rate (POD)	$\frac{H}{H+M}$	1	Fraction of observed CME arrivals that were predicted
Success Ratio (SR)	$\frac{H}{H+FA}$	1	Fraction of correctly predicted CME arrivals
Bias Score	$\frac{H+FA}{H+M}$	1	Ratio of predicted CME arrivals to observed CME arrivals. <1 : underforecast; >1: overforecast.
Critical Success Index (CSI)	$\frac{H}{H+M+FA}$	1	Fraction of correctly observded CME arrivals.
Accuracy	$\frac{H+CR}{Total}$	1	Fraction of the correct CME forecast.
False Alarm Rate (POFD)	$\frac{FA}{CR+FA}$	0	Fraction of incorrectly observed nonaarivals.
Hanssen and Kuipers Discriminant	HK = POD - POFD	1	Ability of forecast to discriminate between observed CME arrivals from non-arrivals.

Table A.4: Metrics related to CME arrival time for hit events. Adapted from: Verbeke et al. [2019]

Metric	**Formula**	**Description**
Mean Error (ME)	$ME = \frac{1}{N} \sum_{i=1}^{N} \Delta t_i$	Way to quantify the bias in the model. Negative bias represent early predicted arrivals, while positive bias denotes late predicted arrivals.
Mean Absolute Error (MAE)	$MAE = \frac{1}{N} \sum_{i=1}^{N} \lvert\Delta t_i\rvert$	
Root Mean Square Error (RMSE)	$RMSE = \sqrt{\frac{1}{N} \sum_{i=1}^{N} (\Delta t_i)^2}$	
Standard deviation (sd)	$sd = \sqrt{variance} = \sqrt{\frac{1}{N-1} \sum_{i=1}^{N} (\Delta t_i - \mathrm{ME})^2}$	

[See Wilks, 2011, Jolliffe and Stephenson, 2011, Verbeke et al., 2019, for detailed description of the metrics mentioned.]

Bibliography

M. S. Abd-Elghany. Ionospheric response to geomagnetic storm impact on secondary air traffic control radar. *London Journal of Research in Science: Natural and Formal*, 2019. 1

M.D. Andrews. Lasco and eit Observations of the Bastille day 2000 Solar Storm. *Solar Physics*, 204(1):179–196, December 2001. ISSN 1573-093X. doi: 10.1023/A:1014215923912. 2

Ester Antonucci, Marco Romoli, Vincenzo Andretta, Silvano Fineschi, Petr Heinzel, J. Daniel Moses, Giampiero Naletto, Gianalfredo Nicolini, Daniele Spadaro, Luca Teriaca, Arkadiusz Berlicki, Gerardo Capobianco, Giuseppe Crescenzio, Vania Da Deppo, Mauro Focardi, Fabio Frassetto, Klaus Heerlein, Federico Landini, Enrico Magli, Andrea Marco Malvezzi, Giuseppe Massone, Radek Melich, Piergiorgio Nicolosi, Giancarlo Noci, Maurizio Pancrazzi, Maria G. Pelizzo, Luca Poletto, Clementina Sasso, Udo Schühle, Sami K. Solanki, Leonard Strachan, Roberto Susino, Giuseppe Tondello, Michela Uslenghi, Joachim Woch, Lucia Abbo, Alessandro Bemporad, Marta Casti, Sergio Dolei, Catia Grimani, Mauro Messerotti, Marco Ricci, Thomas Straus, Daniele Telloni, Paola Zuppella, Frederic Auchère, Roberto Bruno, Angela Ciaravella, Alain J. Corso, Miguel Alvarez Copano, Regina Aznar Cuadrado, Raffaella D'Amicis, Reiner Enge, Alessio Gravina, Sonja Jejčič, Philippe Lamy, Alessandro Lanzafame, Thimo Meierdierks, Ioanna Papagiannaki, Hardi Peter, German Fernandez Rico, Mewael Giday Sertsu, Jan Staub, Kanaris Tsinganos, Marco Velli, Rita Ventura, Enrico Verroi, Jean-Claude Vial, Sebastien Vives, Antonio Volpicelli, Stephan Werner, Andreas Zerr, Barbara Negri, Marco Castronuovo, Alessandro Gabrielli, Roberto Bertacin, Rita Carpentiero, Silvia Natalucci, Filippo Marliani, Marco Cesa, Philippe Laget, Danilo Morea, Stefano Pieraccini, Paolo Radaelli, Paolo Sandri, Paolo Sarra, Stefano Cesare, Felice Del Forno, Ernesto Massa, Mauro Montabone, Sergio Mottini, Daniele Quattropani, Tiziano Schillaci, Roberto Boccardo, Rosario Brando, Arianna Pandi, Cristian Baietto, Riccardo Bertone, Alberto Alvarez-Herrero, Pilar García Parejo, María Cebollero, Mauro Amoruso, and Vito Centonze. Metis: the Solar Orbiter visible light and ultraviolet coronal imager. *Astronomy & Astrophysics*, 642:A10, October 2020. ISSN 0004-6361, 1432-0746. doi: 10.1051/0004-6361/201935338. 32

R. Arlt and Anastasia Abdolvand. First solar butterfly diagram from Schwabe's observations in 1825–1867. *Proceedings of the International Astronomical Union*, 6 (S273):286–289, August 2010. ISSN 1743-9221. doi: 10.1017/S1743921311015390. xvii, 11

E. Asvestari, J. Pomoell, E. Kilpua, S. Good, T. Chatzistergos, M. Temmer, E. Palmerio, S. Poedts, and J. Magdalenic. Modelling a multi-spacecraft coronal mass ejection encounter with EUHFORIA. *Astronomy & Astrophysics*, 652:A27, August 2021. ISSN 0004-6361, 1432-0746. doi: 10.1051/0004-6361/202140315. 84

John N. Bahcall. Solar neutrino experiments. *Reviews of Modern Physics*, 50(4): 881–903, October 1978. ISSN 0034-6861. doi: 10.1103/RevModPhys.50.881. 5

S. J. Bame, J. R. Asbridge, W. C. Feldman, E. E. Fenimore, and J. T. Gosling. Solar wind heavy ions from flare-heated coronal plasma. *Solar Physics*, 62(1):179–201, May 1979. ISSN 1573-093X. doi: 10.1007/BF00150143. 41

D. Barnes, J. A. Davies, R. A. Harrison, J. P. Byrne, C. H. Perry, V. Bothmer, J. P. Eastwood, P. T. Gallagher, E. K. J. Kilpua, C. Möstl, L. Rodriguez, A. P. Rouillard, and D. Odstrčil. CMEs in the Heliosphere: II. A Statistical Analysis of the Kinematic Properties Derived from Single-Spacecraft Geometrical Modelling Techniques Applied to CMEs Detected in the Heliosphere from 2007 to 2017 by STEREO/HI-1. *Solar Physics*, 294(5):57, May 2019. ISSN 1573-093X. doi: 10.1007/s11207-019-1444-4. 83

Yoshita Baruah, Souvik Roy, Suvadip Sinha, Erika Palmerio, Sanchita Pal, Denny M. Oliveira, and Dibyendu Nandy. The Loss of Starlink Satellites in February 2022: How Moderate Geomagnetic Storms Can Adversely Affect Assets in Low-Earth Orbit. *Space Weather*, 22(4):e2023SW003716, April 2024. ISSN 1542-7390. doi: 10.1029/2023SW003716. 1

Jacques M. Beckers. Solar Spicules. *Annual Review of Astronomy and Astrophysics*, 10 (1):73, January 1972. ISSN 0066-4146. doi: 10.1146/annurev.aa.10.090172.000445. ADS Bibcode: 1972ARA&A..10...73B. 7

Arnold O. Benz. Flare Observations. *Living Reviews in Solar Physics*, 5(1):1, December 2008. ISSN 1614-4961. doi: 10.12942/lrsp-2008-1. xvii, 16, 18

N. Bergeot, C. Bruyninx, P. Defraigne, S. Pireaux, J. Legrand, E. Pottiaux, and Q. Baire. Impact of the Halloween 2003 ionospheric storm on kinematic GPS positioning in Europe. *GPS Solutions*, 15(2):171–180, April 2011. ISSN 1521-1886. doi: 10.1007/s10291-010-0181-9. 2

D. Berghmans, B. H. Foing, and B. Fleck. Automated detection of cmes in lasco data. In *From Solar Min to Max: Half a Solar Cycle with SOHO*, volume 508, pages 437–440, June 2002. ADS Bibcode: 2002ESASP.508..437B. 45

A. Bhatnagar and William Charles Livingston. *Fundamentals of Solar Astronomy*. World Scientific, April 2005. ISBN 9789812567871. doi: 10.1142/5171. Google-Books-ID: fe7XDuxCYjcC. 5

Ludwig Biermann. Kometenschweife und solare Korpuskularstrahlung. *Zeitschrift für Astrophysik, Vol. 29, p. 274*, 29:274, 1951. 12

G. Borrini, J. T. Gosling, S. J. Bame, and W. C. Feldman. Helium abundance enhancements in the solar wind. *Journal of Geophysical Research: Space Physics*, 87(A9):7370–7378, September 1982. ISSN 2156-2202. doi: 10.1029/ja087ia09p07370. 41

G. Borrini, J. T. Gosling, S. J. Bame, and W. C. Feldman. Helium abundance variations in the solar wind. *Solar Physics*, 83(2):367–378, March 1983. ISSN 1573-093X. doi: 10.1007/BF00148286. 41

D. H. Boteler. A 21st Century View of the March 1989 Magnetic Storm. *Space Weather*, 17(10):1427–1441, October 2019. ISSN 1542-7390. doi: 10.1029/2019SW002278. 2

V. Bothmer and R. Schwenn. The structure and origin of magnetic clouds in the solar wind. *Annales Geophysicae*, 16(1):1–24, December 1997. ISSN 1432-0576. doi: 10.1007/s005850050575. 58

Doug Brinkman, Manolis Georgoulis, Justin Likar, JeffreyLove, Slava Merkin, Jeff Newmark, Phil Quinn, Ian Richardson, DimitriosVasiliadis, Kathryn Whitman, and Harry Warren. Space weather science and observation gap analysis for nasa, 2021. 53

G. E. Brueckner, R. A. Howard, M. J. Koomen, C. M. Korendyke, D. J. Michels, J. D. Moses, D. G. Socker, K. P. Dere, P. L. Lamy, A. Llebaria, M. V. Bout, R. Schwenn, G. M. Simnett, D. K. Bedford, and C. J. Eyles. The Large Angle Spectroscopic Coronagraph (LASCO). *The SOHO mission*, pages 357–402, 1995. doi: 10.1007/978-94-009-0191-9_10. 28

Jason P. Byrne. *The Kinematics and Morphologyof Solar Coronal Mass Ejections*. PhD thesis, University of Dublin, Trinity College, 2010. xvii, 5, 11, 14

Jaša Čalogović, Mateja Dumbović, Davor Sudar, Bojan Vršnak, Karmen Martinić, Manuela Temmer, and Astrid M. Veronig. Probabilistic drag-based ensemble model (DBEM) evaluation for heliospheric propagation of CMEs. *Solar Physics*, 296(7), jul 2021. ISSN 1573-093X. doi: 10.1007/s11207-021-01859-5. xx, 63, 64, 66, 67, 76, 97, 99

H. V. Cane and I. G. Richardson. Interplanetary coronal mass ejections in the near-Earth solar wind during 1996–2002. *Journal of Geophysical Research: Space Physics*, 108(A4), April 2003. ISSN 2156-2202. doi: 10.1029/2002ja009817. 48

H. V. Cane, I. G. Richardson, and T. T. von Rosenvinge. Cosmic ray decreases: 1964–1994. *Journal of Geophysical Research: Space Physics*, 101(A10):21561–21572, October 1996. ISSN 2156-2202. doi: 10.1029/96ja01964. 41

H. V. Cane, I. G. Richardson, and G. Wibberenz. Helios 1 and 2 observations of particle decreases, ejecta, and magnetic clouds. *Journal of Geophysical Research: Space Physics*, 102(A4):7075–7086, 1997. ISSN 2156-2202. doi: 10.1029/97ja00149. 80

P. J. Cargill, J. Chen, D. S. Spicer, and S. T. Zalesak. Magnetohydrodynamic simulations of the motion of magnetic flux tubes through a magnetized plasma. *Journal of Geophysical Research: Space Physics*, 101(A3):4855–4870, March 1996. ISSN 2156-2202. doi: 10.1029/95ja03769. 53

Peter J. Cargill. On the aerodynamic drag force acting on interplanetary coronal mass ejections. *Solar Physics*, 221(1):135–149, may 2004. ISSN 0038-0938. doi: 10.1023/b:sola.0000033366.10725.a2. 53, 54, 58

R. C. Carrington. Description of a Singular Appearance seen in the Sun on September 1, 1859. *Monthly Notices of the Royal Astronomical Society*, 20(1):13–15, November 1859. ISSN 0035-8711. doi: 10.1016/b978-0-08-006653-0.50020-7. 2

Simone Chierichini, Gregoire Francisco, Ronish Mugatwala, Raffaello Foldes, Enrico Camporeale, Giancarlo De Gasperis, Luca Giovannelli, Gianluca Napoletano, Dario Del Moro, and Robertus Erdelyi. A Bayesian approach to the drag-based modelling of ICMEs. *Journal of Space Weather and Space Climate*, 14:1, 2024. ISSN 2115-7251. doi: 10.1051/swsc/2023032. 67, 100

Arnab Rai Choudhuri. *The Physics of Fluids and Plasmas: An Introduction for Astrophysicists*. Cambridge University Press, Cambridge, November 1998. ISBN 9780521555432. doi: 10.1017/cbo9781139171069. 12, 13

E. W. Cliver. The 1859 space weather event: Then and now. *Advances in Space Research*, 38(2):119–129, January 2006. ISSN 0273-1177. doi: 10.1016/j.asr.2005.07.077. ADS Bibcode: 2006AdSpR..38..119C. 3

Edward W. Cliver, Carolus J. Schrijver, Kazunari Shibata, and Ilya G. Usoskin. Extreme solar events. *Living Reviews in Solar Physics*, 19(1):2, May 2022. ISSN 1614-4961. doi: 10.1007/s41116-022-00033-8. 3

Steven R. Cranmer, Sarah E. Gibson, and Pete Riley. Origins of the ambient solar wind: Implications for space weather. *Space Science Reviews*, 212:1345–1384, November 2017. ISSN 0038-6308. doi: 10.1007/s11214-017-0416-y. URL `https://ui.adsabs.`

harvard.edu/abs/2017SSRv..212.1345C. ADS Bibcode: 2017SSRv..212.1345C. 13

Tiar Dani, Johan Muhamad, Muhamad Zamzam Nurzaman, Rasdewita Kesumaningrum, Santi Sulistiani, Ayu Dyah Pangestu, Ahmad Zulfiana Utama, Elvina Ayu Ratnasari, and Mira Juangsih. Prediction of Coronal Mass Ejection Transit Time and Arrival Speed Using Machine Learning-Assisted Drag Based Model. *SSRN Electronic Journal*, December 2022. ISSN 1556-5068. doi: 10.2139/ssrn.4309777. 100

E. E. Davies, C. Möstl, M. J. Owens, A. J. Weiss, T. Amerstorfer, J. Hinterreiter, M. Bauer, R. L. Bailey, M. A. Reiss, R. J. Forsyth, T. S. Horbury, H. O'Brien, V. Evans, V. Angelini, D. Heyner, I. Richter, H.-U. Auster, W. Magnes, W. Baumjohann, D. Fischer, D. Barnes, J. A. Davies, and R. A. Harrison. In situ multi-spacecraft and remote imaging observations of the first CME detected by solar orbiter and BepiColombo. *Astronomy & Astrophysics*, 656:A2, dec 2021a. doi: 10.5194/epsc2021-533. 84

Emma Davies. *The Evolution of Interplanetary Coronal Mass Ejections in the Heliosphere*. PhD thesis, Imperial College London, May 2021. 41, 84

Emma E. Davies, Robert J. Forsyth, Réka M. Winslow, Christian Möstl, and Noé Lugaz. A Catalog of Interplanetary Coronal Mass Ejections Observed by Juno between 1 and 5.4 au. *The Astrophysical Journal*, 923(2):136, December 2021b. ISSN 0004-637X. doi: 10.3847/1538-4357/ac2ccb. 84

Emma E. Davies, Réka M. Winslow, Camilla Scolini, Robert J. Forsyth, Christian Möstl, Noé Lugaz, and Antoinette B. Galvin. Multi-spacecraft Observations of the Evolution of Interplanetary Coronal Mass Ejections between 0.3 and 2.2 au: Conjunctions with the Juno Spacecraft. *The Astrophysical Journal*, 933(2):127, July 2022. ISSN 0004-637X. doi: 10.3847/1538-4357/ac731a. 84

Judith de Patoul. *Stereoscopy and Tomography of Coronal Structures*. PhD thesis, Max-Planck-Institute for Solar System Research, Lindau, April 2012. xvii, 8

J.-P. Delaboudinière, G. E. Artzner, J. Brunaud, A. H. Gabriel, J. F. Hochedez, F. Millier, X. Y. Song, B. Au, K. P. Dere, R. A. Howard, R. Kreplin, D. J. Michels, J. D. Moses, J. M. Defise, C. Jamar, P. Rochus, J. P. Chauvineau, J. P. Marioge, R. C. Catura, J. R. Lemen, L. Shing, R. A. Stern, J. B. Gurman, W. M. Neupert, A. Maucherat, F. Clette, P. Cugnon, and E. L. Van Dessel. EIT: Extreme-UltraViolet Imaging Telescope for the SOHO Mission. pages 291–312. Springer Netherlands, Dordrecht, 1995. ISBN 9789400901919. doi: 10.1007/978-94-009-0191-9_8. 34

P. Demarque and D. B. Guenther. Helioseismology: Probing the interior of a star. *Proceedings of the National Academy of Sciences*, 96(10):5356–5359, May 1999. doi: 10.1073/pnas.96.10.5356. 5

V. Domingo, B. Fleck, and A. I. Poland. The SOHO mission: An overview. *Solar Physics*, 162(1):1–37, December 1995. ISSN 1573-093X. doi: 10.1007/BF00733425. 28

Mateja Dumbović, Jaša Čalogović, Bojan Vršnak, Manuela Temmer, M. Leila Mays, Astrid Veronig, and Isabell Piantschitsch. The drag-based ensemble model (DBEM) for coronal mass ejection propagation. *The Astrophysical Journal*, 854(2):180, feb 2018. ISSN 1538-4357. doi: 10.3847/1538-4357/aaaa66. 63, 75, 76, 97, 99

Mateja Dumbović, Jaša Čalogović, Karmen Martinić, Bojan Vršnak, Davor Sudar, Manuela Temmer, and Astrid Veronig. Drag-based model (dbm) tools for forecast of coronal mass ejection arrival time and speed. *Frontiers in Astronomy and Space Sciences*, 8:639986, May 2021. ISSN 2296-987X. doi: 10.3389/fspas.2021.639986. 64, 97, 99

T. V. Falkenberg, S. Vennerstrom, D. A. Brain, G. Delory, and A. Taktakishvili. Multipoint observations of coronal mass ejection and solar energetic particle events on Mars and Earth during November 2001. *Journal of Geophysical Research: Space Physics*, 116(A6):n/a–n/a, June 2011. ISSN 2156-2202. doi: 10.1029/2010ja016279. 80

Tzu-Wei Fang, Adam Kubaryk, David Goldstein, Zhuxiao Li, Tim Fuller-Rowell, George Millward, Howard J. Singer, Robert Steenburgh, Solomon Westerman, and Erik Babcock. Space Weather Environment During the SpaceX Starlink Satellite Loss in February 2022. *Space Weather*, 20(11):e2022SW003193, November 2022. ISSN 1542-7390. doi: 10.1029/2022sw003193. 1

U. Feldman, E. Landi, and N. A. Schwadron. On the sources of fast and slow solar wind. *Journal of Geophysical Research: Space Physics*, 110(A7), July 2005. ISSN 0148-0227. doi: 10.1029/2004ja010918. 13

L. Fletcher, B. R. Dennis, H. S. Hudson, S. Krucker, K. Phillips, A. Veronig, M. Battaglia, L. Bone, A. Caspi, Q. Chen, P. Gallagher, P. T. Grigis, H. Ji, W. Liu, R. O. Milligan, and M. Temmer. An Observational Overview of Solar Flares. *Space Science Reviews*, 159(1):19, August 2011. ISSN 1572-9672. doi: 10.1007/s11214-010-9701-8. xxiii, 16

A Fludra, JLR Saba, JC Henoux, RJ Murphy, DV Reames, JR Lemen, KT Strong, J Sylwester, and KG Widing. The many faces of the sun. *Berlin: Springer*, 4, 1999. 19

N. J. Fox, M. C. Velli, S. D. Bale, R. Decker, A. Driesman, R. A. Howard, J. C. Kasper, J. Kinnison, M. Kusterer, D. Lario, M. K. Lockwood, D. J. McComas, N. E. Raouafi, and A. Szabo. The Solar Probe Plus Mission: Humanity's First Visit to Our Star. *Space Science Reviews*, 204(1):7–48, December 2016. ISSN 1572-9672. doi: 10.1007/s11214-015-0211-6. 40

Nicola Fox. Eugene Parker (1927–2022). *Nature Astronomy*, 6(6):625–625, June 2022. ISSN 2397-3366. doi: 10.1038/s41550-022-01686-z. 12

Jan Gieseler, Nina Dresing, Christian Palmroos, Johan L. Freiherr von Forstner, Daniel J. Price, Rami Vainio, Athanasios Kouloumvakos, Laura Rodríguez-García, Domenico Trotta, Vincent Génot, Arnaud Masson, Markus Roth, and Astrid Veronig. Solar-MACH: An open-source tool to analyze solar magnetic connection configurations. *Frontiers in Astronomy and Space Sciences*, 9:384, February 2023. doi: 10.3389/fspas.2022.1058810. ADS Bibcode: 2023FrASS...958810G. 85

Tamas I. Gombosi. *Physics of the Space Environment.* Cambridge University Press, October 1998. ISBN 9780521592642. doi: 10.1017/cbo9780511529474. Google-Books-ID: WCIriLrGIRsC. 5, 10, 12, 15

S. W. Good and R. J. Forsyth. Interplanetary Coronal Mass Ejections Observed by MESSENGER and Venus Express. *Solar Physics*, 291(1):239–263, January 2016. ISSN 1573-093X. doi: 10.1007/s11207-015-0828-3. 80, 84

S. W. Good, E. K. J. Kilpua, A. T. LaMoury, R. J. Forsyth, J. P. Eastwood, and C. Möstl. Self-similarity of ICME flux ropes: Observations by radially aligned spacecraft in the inner heliosphere. *Journal of Geophysical Research: Space Physics*, 124(7):4960–4982, jul 2019. doi: 10.1029/2019ja026475. 84

N Gopalswamy. A global picture of cmes in the inner heliosphere. *The sun and the heliosphere as an integrated system*, pages 201–251, 2004. ISSN 0067-0057. doi: 10.1007/978-1-4020-2831-1_8. 19, 20, 21

N. Gopalswamy, A. Lara, R. P. Lepping, M. L. Kaiser, D. Berdichevsky, and O. C. St. Cyr. Interplanetary acceleration of coronal mass ejections. *Geophysical Research Letters*, 27(2):145–148, 2000. ISSN 1944-8007. doi: 10.1029/1999GL003639. 52

N. Gopalswamy, S. Yashiro, G. Michalek, G. Stenborg, A. Vourlidas, S. Freeland, and R. Howard. The SOHO/LASCO CME Catalog. *Earth Moon and Planets*, 104:295–313, April 2009. ISSN 0167-9295. doi: 10.1007/s11038-008-9282-7. ADS Bibcode: 2009EM&P..104..295G. xviii, 17, 20, 21, 29, 44, 67

Nat Gopalswamy. Coronal mass ejections and space weather. In *Climate and Weather of the Sun-Earth System (CAWSES): Selected Papers from the 2007 Kyoto*

Symposium, pages 77–120. Terrapub Tokyo, Japan, 2009. doi: http://www.terrapub.co.jp/onlineproceedings/ste/CAWSES2007/index.html. 54

Nat Gopalswamy, Alejandro Lara, Seiji Yashiro, Mike L Kaiser, and Russell A Howard. Predicting the 1-au arrival times of coronal mass ejections. *Journal of Geophysical Research: Space Physics*, 106(A12):29207–29217, December 2001. ISSN 0148-0227. doi: 10.1029/2001ja000177. 52

Nat Gopalswamy, Grzegorz Michałek, Seiji Yashiro, Pertti Mäkelä, Sachiko Akiyama, Hong Xie, and Angelos Vourlidas. The soho lasco cme catalog–version 2. *arXiv e-prints*, July 2024. doi: 10.48550/arXiv.2407.04165. ADS Bibcode: 2024arXiv240704165G Type: article. 29, 44

J. T. Gosling, E. Hildner, R. M. MacQueen, R. H. Munro, A. I. Poland, and C. L. Ross. The speeds of coronal mass ejection events. *Solar Physics*, 48(2):389–397, June 1976. ISSN 1573-093X. doi: 10.1007/BF00152004. 26

Sabrina Guastavino, Valentina Candiani, Alessandro Bemporad, Francesco Marchetti, Federico Benvenuto, Anna Maria Massone, Roberto Susino, Daniele Telloni, Silvano Fineschi, and Michele Piana. Physics-driven machine learning for the prediction of coronal mass ejections' travel times. Technical report, May 2023. arXiv:2305.10057 [astro-ph, physics:physics] type: article. 100

George E. Hale and Seth B. Nicholson. The Law of Sun-Spot Polarity. *The Astrophysical Journal*, 62:270, November 1925. ISSN 0004-637X. doi: 10.1086/142933. ADS Bibcode: 1925ApJ....62..270H. 10

George Ellery Hale. 16. on the probable existence of a magnetic field in sun-spots. *Astrophysical Journal*, 28:315–343, November 1908. ISSN 1538-4357. doi: 10.1086/141602. 9

Mike Hapgood, Huixin Liu, and Noé Lugaz. SpaceX—Sailing Close to the Space Weather? *Space Weather*, 20(3):e2022SW003074, 2022. ISSN 1542-7390. doi: 10.1029/2022SW003074. 1

Hodson. Mr. Carrington regrets having omitted previously to communicate the following passage in a letter from M. Schwabe, dated March, which is plainly intended for others as well as himself. *Monthly Notices of the Royal Astronomical Society*, 20(1):15–16, November 1859. ISSN 0035-8711. doi: 10.1093/mnras/20.1.15. 2

L. L. House, W. J. Wagner, E. Hildner, C. Sawyer, and H. U. Schmidt. Studies of the corona with the Solar Maximum Mission coronagraph/polarimeter. *The*

Astrophysical Journal, 244:L117–L121, March 1981. ISSN 0004-637X. doi: 10.1086/183494. ADS Bibcode: 1981ApJ...244L.117H. 19

R. A. Howard, D. J. Michels, N. R. Sheeley, Jr., and M. J. Koomen. The observation of a coronal transient directed at Earth. *The Astrophysical Journal*, 263:L101–L104, December 1982. ISSN 0004-637X. doi: 10.1086/183932. ADS Bibcode: 1982ApJ...263L.101H. 20, 26

R. A. Howard, J. D. Moses, D. G. Socker, K. P. Dere, and J. W. Cook. Sun earth connection coronal and heliospheric investigation (SECCHI). *Advances in Space Research*, 29(12):2017–2026, June 2002. ISSN 0273-1177. doi: 10.1016/S0273-1177(02)00147-3. 30

R. A. Howard, J. D. Moses, A. Vourlidas, J. S. Newmark, D. G. Socker, S. P. Plunkett, C. M. Korendyke, J. W. Cook, A. Hurley, J. M. Davila, W. T. Thompson, O. C. St Cyr, E. Mentzell, K. Mehalick, J. R. Lemen, J. P. Wuelser, D. W. Duncan, T. D. Tarbell, C. J. Wolfson, A. Moore, R. A. Harrison, N. R. Waltham, J. Lang, C. J. Davis, C. J. Eyles, H. Mapson-Menard, G. M. Simnett, J. P. Halain, J. M. Defise, E. Mazy, P. Rochus, R. Mercier, M. F. Ravet, F. Delmotte, F. Auchere, J. P. Delaboudiniere, V. Bothmer, W. Deutsch, D. Wang, N. Rich, S. Cooper, V. Stephens, G. Maahs, R. Baugh, D. McMullin, and T. Carter. Sun earth connection coronal and heliospheric investigation (secchi). *Space Science Reviews*, 136(1–4), April 2008. ISSN 1572-9672. doi: 10.1007/s11214-008-9341-4. 30, 31

R. A. Howard, A. Vourlidas, R. C. Colaninno, C. M. Korendyke, S. P. Plunkett, M. T. Carter, D. Wang, N. Rich, S. Lynch, A. Thurn, D. G. Socker, A. F. Thernisien, D. Chua, M. G. Linton, S. Koss, S. Tun-Beltran, H. Dennison, G. Stenborg, D. R. McMullin, T. Hunt, R. Baugh, G. Clifford, D. Keller, J. R. Janesick, J. Tower, M. Grygon, R. Farkas, R. Hagood, K. Eisenhauer, A. Uhl, S. Yerushalmi, L. Smith, P. C. Liewer, M. C. Velli, J. Linker, V. Bothmer, P. Rochus, J.-P. Halain, P. L. Lamy, F. Auchère, R. A. Harrison, A. Rouillard, S. Patsourakos, O. C. St Cyr, H. Gilbert, H. Maldonado, C. Mariano, and J. Cerullo. The Solar Orbiter Heliospheric Imager (SoloHI). *Astronomy & Astrophysics*, 642:A13, October 2020. ISSN 0004-6361, 1432-0746. doi: 10.1051/0004-6361/201935202. 39

Tim Howard. *Space Weather and Coronal Mass Ejections*. SpringerLink. Springer, New York, NY, 2014. ISBN 9781461479758. doi: 10.1007/978-1-4614-7975-8. Description based upon print version of record. xviii, 26

Timothy Howard. *Coronal Mass Ejections: An Introduction*. Springer New York, 2011. ISBN 9781441987891. doi: 10.1007/978-1-4419-8789-1. 17, 18, 19, 41

Hugh S. Hudson. Carrington Events. *Annual Review of Astronomy and Astrophysics*, 59(Volume 59, 2021):445–477, September 2021. ISSN 0066-4146, 1545-4282. doi: 10.1146/annurev-astro-112420-023324. 3

A. J. Hundhausen. Sizes and locations of coronal mass ejections: SMM observations from 1980 and 1984-1989. *Journal of Geophysical Research: Space Physics*, 98(A8): 13177–13200, 1993. ISSN 2156-2202. doi: 10.1029/93JA00157. 17

R. M. E. Illing and A. J. Hundhausen. Observation of a coronal transient from 1.2 to 6 solar radii. *Journal of Geophysical Research: Space Physics*, 90(A1):275–282, 1985. ISSN 2156-2202. doi: 10.1029/JA090iA01p00275. 19

B. M. Jakosky, R. P. Lin, J. M. Grebowsky, J. G. Luhmann, D. F. Mitchell, G. Beutelschies, T. Priser, M. Acuna, L. Andersson, D. Baird, D. Baker, R. Bartlett, M. Benna, S. Bougher, D. Brain, D. Carson, S. Cauffman, P. Chamberlin, J.-Y. Chaufray, O. Cheatom, J. Clarke, J. Connerney, T. Cravens, D. Curtis, G. Delory, S. Demcak, A. DeWolfe, F. Eparvier, R. Ergun, A. Eriksson, J. Espley, X. Fang, D. Folta, J. Fox, C. Gomez-Rosa, S. Habenicht, J. Halekas, G. Holsclaw, M. Houghton, R. Howard, M. Jarosz, N. Jedrich, M. Johnson, W. Kasprzak, M. Kelley, T. King, M. Lankton, D. Larson, F. Leblanc, F. Lefevre, R. Lillis, P. Mahaffy, C. Mazelle, W. McClintock, J. McFadden, D. L. Mitchell, F. Montmessin, J. Morrissey, W. Peterson, W. Possel, J.-A. Sauvaud, N. Schneider, W. Sidney, S. Sparacino, A. I. F. Stewart, R. Tolson, D. Toublanc, C. Waters, T. Woods, R. Yelle, and R. Zurek. The Mars Atmosphere and Volatile Evolution (MAVEN) Mission. *Space Science Reviews*, 195(1):3–48, December 2015. ISSN 1572-9672. doi: 10.1007/s11214-015-0139-x. 82

Ian T. Jolliffe and David B. Stephenson. *Forecast Verification: A Practitioner's Guide in Atmospheric Science*. John Wiley & Sons, December 2011. ISBN 9780470660713. Google-Books-ID: sgwIEAAAQBAJ. 122

M. L. Kaiser. The STEREO mission: an overview. *Advances in Space Research*, 36 (8):1483–1488, January 2005. ISSN 0273-1177. doi: 10.1016/j.asr.2004.12.066. 30

C. Kay, M. L. Mays, and C. Verbeke. Identifying critical input parameters for improving drag-based CME arrival time predictions. *Space Weather*, 18(1), jan 2020. doi: 10.1029/2019sw002382. 67

E. K. J. Kilpua, S. W. Good, N. Dresing, R. Vainio, E. E. Davies, R. J. Forsyth, J. Gieseler, B. Lavraud, E. Asvestari, D. E. Morosan, J. Pomoell, D. J. Price, D. Heyner, T. S. Horbury, V. Angelini, H. O'Brien, V. Evans, J. Rodriguez-Pacheco, R. Gómez Herrero, G. C. Ho, and R. Wimmer-Schweingruber. Multi-spacecraft observations of the structure of the sheath of an interplanetary coronal mass ejection and related energetic ion enhancement. *Astronomy & Astrophysics*, 656:A8, dec 2021. doi: 10.1051/0004-6361/202140838. 84

Emilia Kilpua, Hannu E. J. Koskinen, and Tuija I. Pulkkinen. Coronal mass ejections and their sheath regions in interplanetary space. *Living Reviews in Solar Physics*, 14(1):5, November 2017. ISSN 1614-4961. doi: 10.1007/s41116-017-0009-6. xix, 42

T. Kirsten. Solar Neutrino Problems. *Annals of the New York Academy of Sciences*, 759, 1995. doi: 10.1111/j.1749-6632.1995.tb17513.x. 6

L. W. Klein and L. F. Burlaga. Interplanetary magnetic clouds At 1 AU. *Journal of Geophysical Research: Space Physics*, 87(A2):613–624, 1982. ISSN 2156-2202. doi: 10.1029/JA087iA02p00613. 41

Delores J. Knipp, Brian J. Fraser, M. A. Shea, and D. F. Smart. On the Little-Known Consequences of the 4 August 1972 Ultra-Fast Coronal Mass Ejecta: Facts, Commentary, and Call to Action. *Space Weather*, 16(11):1635–1643, 2018. ISSN 1542-7390. doi: 10.1029/2018SW002024. 2

Hannu Koskinen. *Physics of Space Storms: From the Solar Surface to the Earth*. Springer Berlin Heidelberg, 2011. ISBN 9783642003196. doi: 10.1007/978-3-642-00319-6. 9, 10, 12, 15, 16, 17, 19

H. Kunow. *Coronal Mass Ejections*. Number v.21 in Space Sciences Series of ISSI Ser. Springer New York, New York, NY, 2007. ISBN 9780387450889. Description based on publisher supplied metadata and other sources. 26

Alejandro Lara and Andrea I. Borgazzi. Dynamics of interplanetary CMEs and associated type II bursts. 257:287–290, March 2009. doi: 10.1017/S1743921309029421. ADS Bibcode: 2009IAUS..257..287L. 54

Yolande Leblanc, George A. Dulk, and Jean-Louis Bougeret. Tracing the Electron Density from the Corona to 1 au. *Solar Physics*, 183(1):165–180, November 1998. ISSN 1573-093X. doi: 10.1023/A:1005049730506. 55

M. Leitner, C. J. Farrugia, C. Möstl, K. W. Ogilvie, A. B. Galvin, R. Schwenn, and H. K. Biernat. Consequences of the force-free model of magnetic clouds for their heliospheric evolution. *Journal of Geophysical Research: Space Physics*, 112(A6), 2007. ISSN 2156-2202. doi: 10.1029/2006JA011940. 80

James R. Lemen, Alan M. Title, David J. Akin, Paul F. Boerner, Catherine Chou, Jerry F. Drake, Dexter W. Duncan, Christopher G. Edwards, Frank M. Friedlaender, Gary F. Heyman, Neal E. Hurlburt, Noah L. Katz, Gary D. Kushner, Michael Levay, Russell W. Lindgren, Dnyanesh P. Mathur, Edward L. McFeaters, Sarah

Mitchell, Roger A. Rehse, Carolus J. Schrijver, Larry A. Springer, Robert A. Stern, Theodore D. Tarbell, Jean-Pierre Wuelser, C. Jacob Wolfson, Carl Yanari, Jay A. Bookbinder, Peter N. Cheimets, David Caldwell, Edward E. Deluca, Richard Gates, Leon Golub, Sang Park, William A. Podgorski, Rock I. Bush, Philip H. Scherrer, Mark A. Gummin, Peter Smith, Gary Auker, Paul Jerram, Peter Pool, Regina Soufli, David L. Windt, Sarah Beardsley, Matthew Clapp, James Lang, and Nicholas Waltham. The Atmospheric Imaging Assembly (AIA) on the Solar Dynamics Observatory (SDO). *Solar Physics*, 275(1):17–40, January 2012. ISSN 1573-093X. doi: 10.1007/s11207-011-9776-8. 36

R. Leussu, I. Usoskin, V. S. Pavai, A. Diercke, R. Arlt, C. Denker, and K. Mursula. Wings of the butterfly : sunspot groups for 1826–2015. *Astronomy and Astrophysics*, 599, 2017. doi: 10.1051/0004-6361/201629533. xvii, 11

Jiajia Liu, Yudong Ye, Chenglong Shen, Yuming Wang, and Robert Erdélyi. A new tool for cme arrival time prediction using machine learning algorithms: Cat-puma. *The Astrophysical Journal*, 855(2):109, March 2018. ISSN 0004-637X. doi: 10.3847/1538-4357/aaae69. 53

R. E. Lopez. Solar cycle invariance in solar wind proton temperature relationships. *Journal of Geophysical Research: Space Physics*, 92(A10):11189–11194, 1987. ISSN 2156-2202. doi: 10.1029/JA092iA10p11189. 41

Ramon E. Lopez, Daniel N. Baker, and Joe Allen. Sun unleashes Halloween storm. *Eos, Transactions American Geophysical Union*, 85(11):105–108, March 2004. ISSN 2324-9250. doi: 10.1029/2004eo110002. 2

Yingjuan Ma, Xiaohua Fang, Jasper S. Halekas, Shaosui Xu, Christopher T. Russell, Janet G. Luhmann, Andrew F. Nagy, Gabor Toth, Christina O. Lee, Chuanfei Dong, Jared R. Espley, James P. McFadden, David L. Mitchell, and Bruce M. Jakosky. The Impact and Solar Wind Proxy of the 2017 September ICME Event at Mars. *Geophysical Research Letters*, 45:7248–7256, August 2018. ISSN 0094-8276. doi: 10.1029/2018GL077707. ADS Bibcode: 2018GeoRL..45.7248M. 82

R. M. MacQueen, Harrie Stewart Wilson Massey, A. H. Gabriel, and Harry Elliot. Coronal transients: a summary. *Philosophical Transactions of the Royal Society of London. Series A, Mathematical and Physical Sciences*, 297(1433):605–620, January 1997. doi: 10.1098/rsta.1980.0236. 17

Anwesha Maharana, Stefaan Poedts, Luciano Rodriguez, and Jasmina Magdalenic. *Advanced CME models for improved geo-effectiveness predictions*. PhD thesis, 2024-08-28. 10

E. Walter Maunder. Sunspot Variation in Latitude. *Popular Astronomy*, 12:616–619, November 1904. ISSN 0197-7482. ADS Bibcode: 1904PA.....12..616M. 10

Prateek Mayank, Bhargav Vaidya, and D. Chakrabarty. SWASTi-SW: Space Weather Adaptive Simulation Framework for Solar Wind and Its Relevance to the Aditya-L1 Mission. *The Astrophysical Journal Supplement Series*, 262(1):23, September 2022. ISSN 0067-0049. doi: 10.3847/1538-4365/ac8551. 52

M. L. Mays, A. Taktakishvili, A. Pulkkinen, P. J. MacNeice, L. Rastätter, D. Odstrcil, L. K. Jian, I. G. Richardson, J. A. LaSota, Y. Zheng, and M. M. Kuznetsova. Ensemble Modeling of CMEs Using the WSA–ENLIL+Cone Model. *Solar Physics*, 290(6):1775–1814, June 2015. ISSN 1573-093X. doi: 10.1007/s11207-015-0692-1. 60

M. Minnaert. Fourty Years of Solar Spectroscopy. In C. De Jager, editor, *The Solar Spectrum*, pages 3–25, Dordrecht, 1965. Springer Netherlands. ISBN 9789401763769. doi: 10.1007/978-94-010-3587-3_2. 5

E. Mitsakou and X. Moussas. Statistical Study of ICMEs and Their Sheaths During Solar Cycle 23 (1996 – 2008). *Solar Physics*, 289:3137–3157, 2014. doi: 10.1007/S11207-014-0505-Y. 80

Mark Moldwin. *Introduction to Space Weather*. Cambridge University Press, 2008. ISBN 9780511393044. doi: 10.1017/9781108866538. 5, 7, 10, 17

Christian Möstl, Tanja Rollett, Rudy A. Frahm, Ying D. Liu, David M. Long, Robin C. Colaninno, Martin A. Reiss, Manuela Temmer, Charles J. Farrugia, Arik Posner, Mateja Dumbović, Miho Janvier, Pascal Démoulin, Peter Boakes, Andy Devos, Emil Kraaikamp, Mona L. Mays, and Bojan Vršnak. Strong coronal channelling and interplanetary evolution of a solar storm up to Earth and Mars. *Nature Communications*, 6(1):7135, May 2015. ISSN 2041-1723. doi: 10.1038/ncomms8135. 52, 101

Ronish Mugatwala, Simone Chierichini, Gregoire Francisco, Gianluca Napoletano, Raffaello Foldes, Luca Giovannelli, Giancarlo De Gasperis, Enrico Camporeale, Robertus Erdélyi, and Dario Del Moro. A catalogue of observed geo-effective CME/ICME characteristics. *Journal of Space Weather and Space Climate*, 14:6, 2024. ISSN 2115-7251. doi: 10.1051/swsc/2024004. xx, xxi, xxii, xxiii, xxiv, 51, 67, 71, 72, 76, 77, 78, 98, 99, 101, 102, 111, 114, 115, 116

C. Möstl, A. Isavnin, P. D. Boakes, E. K. J. Kilpua, J. A. Davies, R. A. Harrison, D. Barnes, V. Krupar, J. P. Eastwood, S. W. Good, R. J. Forsyth, V. Bothmer, M. A. Reiss, T. Amerstorfer, R. M. Winslow, B. J. Anderson, L. C. Philpott,

L. Rodriguez, A. P. Rouillard, P. Gallagher, T. Nieves-Chinchilla, and T. L. Zhang. Modeling observations of solar coronal mass ejections with heliospheric imagers verified with the Heliophysics System Observatory. *Space Weather*, 15(7):955–970, 2017. ISSN 1542-7390. doi: 10.1002/2017SW001614. 50, 82

Christian Möstl, Andreas J. Weiss, Martin A. Reiss, Tanja Amerstorfer, Rachel L. Bailey, Jürgen Hinterreiter, Maike Bauer, David Barnes, Jackie A. Davies, Richard A. Harrison, Johan L. Freiherr von Forstner, Emma E. Davies, Daniel Heyner, Tim Horbury, and Stuart D. Bale. Multipoint interplanetary coronal mass ejections observed with solar orbiter, BepiColombo, parker solar probe, wind, and STEREO-a. *The Astrophysical Journal Letters*, 924(1):L6, jan 2022. doi: 10.3847/2041-8213/ac42d0. 83, 117, 118, 119

D. Müller, O. C. St Cyr, I. Zouganelis, H. R. Gilbert, R. Marsden, T. Nieves-Chinchilla, E. Antonucci, F. Auchère, D. Berghmans, T. S. Horbury, R. A. Howard, S. Krucker, M. Maksimovic, C. J. Owen, P. Rochus, J. Rodriguez-Pacheco, M. Romoli, S. K. Solanki, R. Bruno, M. Carlsson, A. Fludra, L. Harra, D. M. Hassler, S. Livi, P. Louarn, H. Peter, U. Schühle, L. Teriaca, J. C. del Toro Iniesta, R. F. Wimmer-Schweingruber, E. Marsch, M. Velli, A. De Groof, A. Walsh, and D. Williams. The Solar Orbiter mission - Science overview. *Astronomy & Astrophysics*, 642:A1, October 2020. ISSN 0004-6361, 1432-0746. doi: 10.1051/0004-6361/202038467. 32

Gianluca Napoletano, Roberta Forte, Dario Del Moro, Ermanno Pietropaolo, Luca Giovannelli, and Francesco Berrilli. A probabilistic approach to the drag-based model. *Journal of Space Weather and Space Climate*, 8:A11, 2018. doi: 10.1051/swsc/2018003. 21, 64, 67, 74, 76, 97, 117

Gianluca Napoletano, Raffaello Foldes, Enrico Camporeale, Giancarlo de Gasperis, Luca Giovannelli, Evangelos Paouris, Ermanno Pietropaolo, Jannis Teunissen, Ajay Kumar Tiwari, and Dario Del Moro. Parameter Distributions for the Drag-Based Modeling of CME Propagation. *Space Weather*, 20(9):e2021SW002925, 2022. ISSN 1542-7390. doi: 10.1029/2021SW002925. 67, 68, 74, 75, 76, 95, 96, 97, 111, 112, 113, 114

B. Nava, J. Rodríguez-Zuluaga, K. Alazo-Cuartas, A. Kashcheyev, Y. Migoya-Orué, S.m. Radicella, C. Amory-Mazaudier, and R. Fleury. Middle- and low-latitude ionosphere response to 2015 St. Patrick's Day geomagnetic storm. *Journal of Geophysical Research: Space Physics*, 121(4):3421–3438, 2016. ISSN 2169-9402. doi: 10.1002/2015JA022299. 1

D. Nelson, Trey Jalbert, and Donald VanNess. Solar Spectroscopy. 2006. doi: 10.1002/9783527602551.ch3. 5

T. Nieves-Chinchilla, A. Vourlidas, J. C. Raymond, M. G. Linton, N. Al-haddad, N. P. Savani, A. Szabo, and M. A. Hidalgo. Understanding the Internal Magnetic Field Configurations of ICMEs Using More than 20 Years of Wind Observations. *Solar Physics*, 293(2):25, January 2018. ISSN 1573-093X. doi: 10.1007/s11207-018-1247-z. 49

D. Odstrcil, P. Riley, and X. P. Zhao. Numerical simulation of the 12 May 1997 interplanetary CME event. *Journal of Geophysical Research: Space Physics*, 109 (A2), 2004. ISSN 2156-2202. doi: 10.1029/2003JA010135. 52, 58, 59

O. Olmedo, J. Zhang, H. Wechsler, A. Poland, and K. Borne. *Automatic Detection and Tracking of Coronal Mass Ejections in Coronagraph Time Series*, pages 275–289. Springer New York, 2008. ISBN 9780387981543. doi: 10.1007/978-0-387-98154-3_20. xix, 45, 46

M. Owens and P. Cargill. Predictions of the arrival time of coronal mass ejections at 1au: an analysis of the causes of errors. *Annales Geophysicae*, 22(2):661–671, January 2004. ISSN 1432-0576. doi: 10.5194/angeo-22-661-2004. 54

Sanchita Pal. *Space Weather Drivers and their Geoeffectiveness*. PhD thesis, Centre of Excellence in Space Sciences, Indian Institute of Science Education and Research Kolkata, 2020. 41

Evangelos Paouris and Helen Mavromichalaki. Effective Acceleration Model for the Arrival Time of Interplanetary Shocks driven by Coronal Mass Ejections. *Solar Physics*, 292(12):180, November 2017. ISSN 1573-093X. doi: 10.1007/s11207-017-1212-2. 52

Evangelos Paouris, Jaša Čalogović, Mateja Dumbović, M Leila Mays, Angelos Vourlidas, Athanasios Papaioannou, Anastasios Anastasiadis, and Georgios Balasis. Propagating conditions and the time of icme arrival: A comparison of the effective acceleration model with enlil and dbem models. *Solar Physics*, 296(1), January 2021a. ISSN 1573-093X. doi: 10.1007/s11207-020-01747-4. 52, 69, 75, 76

Evangelos Paouris, Angelos Vourlidas, Athanasios Papaioannou, and Anastasios Anastasiadis. Assessing the projection correction of coronal mass ejection speeds on time-of-arrival prediction performance using the effective acceleration model. *Space Weather*, 19(2), feb 2021b. doi: 10.1029/2020sw002617. 53, 67, 69

W. Dean Pesnell, B. J. Thompson, and P. C. Chamberlin. The Solar Dynamics Observatory (SDO). pages 3–15. Springer US, New York, NY, 2012. ISBN 9781461436737. doi: 10.1007/978-1-4614-3673-7_2. 36

Kenneth J. H. Phillips. *Guide to the Sun.* Cambridge University Press, March 1995. ISBN 9780521397889. Google-Books-ID: idwBChjVP0gC. 5

Stefaan Poedts, Andrea Lani, Camilla Scolini, Christine Verbeke, Nicolas Wijsen, Giovanni Lapenta, Brecht Laperre, Dimitrios Millas, Maria Elena Innocenti, Emmanuel Chané, Tinatin Baratashvili, Evangelia Samara, Ronald Van der Linden, Luciano Rodriguez, Petra Vanlommel, Rami Vainio, Alexandr Afanasiev, Emilia Kilpua, Jens Pomoell, Ranadeep Sarkar, Angels Aran, Blai Sanahuja, Josep M. Paredes, Ellen Clarke, Alan Thomson, Alexis Rouilard, Rui F. Pinto, Aurélie Marchaudon, Pierre-Louis Blelly, Blandine Gorce, Illya Plotnikov, Athanasis Kouloumvakos, Bernd Heber, Konstantin Herbst, Andrey Kochanov, Joachim Raeder, and Jan Depauw. EUropean Heliospheric FORecasting Information Asset 2.0. *Journal of Space Weather and Space Climate*, 10:57, 2020. ISSN 2115-7251. doi: 10.1051/swsc/2020055. 52, 59

Jens Pomoell and S. Poedts. EUHFORIA: European heliospheric forecasting information asset. *Journal of Space Weather and Space Climate*, 8:A35, 2018. ISSN 2115-7251. doi: 10.1051/swsc/2018020. 52, 59

B. Raghavendra Prasad, Dipankar Banerjee, Jagdev Singh, S. Nagabhushana, Amit Kumar, P. U. Kamath, S. Kathiravan, Suresh Venkata, N. Rajkumar, V. Natarajan, Madhur Juneja, Pawan Somu, Vaibhav Pant, Nigar Shaji, K. Sankarsubramanian, Asit Patra, R. Venkateswaran, Abhijit Avinash Adoni, S. Narendra, T. R. Haridas, Shibu K. Mathew, R. Mohan Krishna, K. Amareswari, and Bhavesh Jaiswal. Visible Emission Line Coronagraph on Aditya-L1. *Current Science*, 113(4):613–615, 2017. ISSN 0011-3891. doi: 10.18520/cs/v113/i04/613-615. 33

E. R. Priest. *Magnetohydrodynamics of the sun.* Cambridge University Press, New York, 2014. ISBN 9780521854719. doi: 10.1017/cbo9781139020732. Includes bibliographical references and index. 7

MJ Reiner, ML Kaiser, M Karlický̀, K Jiřička, and J-L Bougeret. Bastille day event: A radio perspective. *Solar Physics*, 204:121–137, 2001. 2

I. G. Richardson and H. V. Cane. Near-Earth Interplanetary Coronal Mass Ejections During Solar Cycle 23 (1996 – 2009): Catalog and Summary of Properties. *Solar Physics*, 264(1):189–237, June 2010. ISSN 1573-093X. doi: 10.1007/s11207-010-9568-6. 48, 80

I. G. Richardson, E. W. Cliver, and H. V. Cane. Sources of geomagnetic storms for solar minimum and maximum conditions during 1972–2000. *Geophysical Research Letters*, 28(13):2569–2572, 2001. ISSN 1944-8007. doi: 10.1029/2001GL013052. 41

Pete Riley, M. Leila Mays, Jesse Andries, Tanja Amerstorfer, Douglas Biesecker, Veronique Delouille, Mateja Dumbović, Xueshang Feng, Edmund Henley, Jon A. Linker, Christian Möstl, Marlon Nuñez, Vic Pizzo, Manuela Temmer, W. K. Tobiska, C. Verbeke, Matthew J West, and Xinhua Zhao. Forecasting the arrival time of coronal mass ejections: Analysis of the CCMC CME scoreboard. *Space Weather*, 16(9):1245–1260, sep 2018. doi: 10.1029/2018sw001962. 52, 53

François Rincon and Michel Rieutord. The Sun's supergranulation. *Living Reviews in Solar Physics*, 15(1):6, September 2018. ISSN 1614-4961. doi: 10.1007/s41116-018-0013-5. 7

E. Robbrecht and D. Berghmans. Automated recognition of coronal mass ejections (CMEs) in near-real-time data. *Astronomy & Astrophysics*, 425(3):1097–1106, October 2004. ISSN 0004-6361, 1432-0746. doi: 10.1051/0004-6361:20041302. 46

E. Robbrecht, D. Berghmans, and R. A. M. Van der Linden. AUTOMATED LASCO CME CATALOG FOR SOLAR CYCLE 23: ARE CMEs SCALE INVARIANT? *The Astrophysical Journal*, 691(2):1222, February 2009. ISSN 0004-637X. doi: 10.1088/0004-637X/691/2/1222. 17

P. Rochus, F. Auchère, D. Berghmans, L. Harra, W. Schmutz, U. Schühle, P. Addison, T. Appourchaux, R. Aznar Cuadrado, D. Baker, J. Barbay, D. Bates, A. BenMoussa, M. Bergmann, C. Beurthe, B. Borgo, K. Bonte, M. Bouzit, L. Bradley, V. Büchel, E. Buchlin, J. Büchner, F. Cabé, L. Cadiergues, M. Chaigneau, B. Chares, C. Choque Cortez, P. Coker, M. Condamin, S. Coumar, W. Curdt, J. Cutler, D. Davies, G. Davison, J.-M. Defise, G. Del Zanna, F. Delmotte, V. Delouille, L. Dolla, C. Dumesnil, F. Dürig, R. Enge, S. François, J.-J. Fourmond, J.-M. Gillis, B. Giordanengo, S. Gissot, L. M. Green, N. Guerreiro, A. Guilbaud, M. Gyo, M. Haberreiter, A. Hafiz, M. Hailey, J.-P. Halain, J. Hansotte, C. Hecquet, K. Heerlein, M.-L. Hellin, S. Hemsley, A. Hermans, V. Hervier, J.-F. Hochedez, Y. Houbrechts, K. Ihsan, L. Jacques, A. Jérôme, J. Jones, M. Kahle, T. Kennedy, M. Klaproth, M. Kolleck, S. Koller, E. Kotsialos, E. Kraaikamp, P. Langer, A. Lawrenson, J.-C. Le Clech', C. Lenaerts, S. Liebecq, D. Linder, D. M. Long, B. Mampaey, D. Markiewicz-Innes, B. Marquet, E. Marsch, S. Matthews, E. Mazy, A. Mazzoli, S. Meining, E. Meltchakov, R. Mercier, S. Meyer, M. Monecke, F. Monfort, G. Morinaud, F. Moron, L. Mountney, R. Müller, B. Nicula, S. Parenti, H. Peter, D. Pfiffner, A. Philippon, I. Phillips, J.-Y. Plesseria, E. Pylyser, F. Rabecki, M.-F. Ravet-Krill, J. Rebellato, E. Renotte, L. Rodriguez, S. Roose, J. Rosin, L. Rossi, P. Roth, F. Rouesnel, M. Roulliay, A. Rousseau, K. Ruane, J. Scanlan, P. Schlatter, D. B. Seaton, K. Silliman, S. Smit, P. J. Smith, S. K. Solanki, M. Spescha, A. Spencer, K. Stegen, Y. Stockman, N. Szwec, C. Tamiatto, J. Tandy, L. Teriaca, C. Theobald, I. Tychon, L. van Driel-Gesztelyi, C. Verbeeck, J.-C. Vial, S. Werner, M. J. West, D. Westwood, T. Wiegelmann, G. Willis, B. Winter, A. Zerr, X. Zhang, and A. N. Zhukov. The Solar Orbiter EUI instrument: The Extreme Ultraviolet Imager. *Astronomy & Astrophysics*, 642:A8, October 2020. ISSN 0004-6361, 1432-0746. doi: 10.1051/0004-6361/201936663. 36

Tanja Rollett, Christian Möstl, Alexey Isavnin, Jackie A Davies, Manuel Kubicka, Ute V Amerstorfer, and Richard A Harrison. ElEvoHI: A NOVEL CME PREDICTION TOOL FOR HELIOSPHERIC IMAGING COMBINING AN ELLIPTICAL FRONT WITH DRAG-BASED MODEL FITTING. *The Astrophysical Journal*, 824(2):131, jun 2016. doi: 10.3847/0004-637x/824/2/131. 101

Nishtha Sachdeva. *Dynamics of solar CoronalMass Ejections: forces that impact their propagation*. PhD thesis, INDIAN INSTITUTE OF SCIENCE EDUCATION AND RESEARCH, PUNE, 2018. 7, 26, 55, 59

Nishtha Sachdeva, Prasad Subramanian, Robin Colaninno, and Angelos Vourlidas. Cme propagation : Where does aerodynamic drag "take over" ? *The Astrophysical Journal*, 809(2):158, aug 2015. doi: 10.1088/0004-637x/809/2/158. 59

T. M. Salman, R. M. Winslow, and N. Lugaz. Radial evolution of coronal mass ejections between MESSENGER, *venusexpress* STEREO, and l1: Catalog and analysis. *Journal of Geophysical Research: Space Physics*, 125(1), jan 2020. doi: 10.1029/2019ja027084. 84

Tarik Mohammad Salman, Teresa Nieves-Chinchilla, Lan K. Jian, Noé Lugaz, Fernando Carcaboso, Emma E. Davies, and Yaireska M. Collado-Vega. A Survey of Coronal Mass Ejections Measured In Situ by Parker Solar Probe during 2018–2022. *The Astrophysical Journal*, 966(1):118, April 2024. ISSN 0004-637X. doi: 10.3847/1538-4357/ad320c. 84

Carolus J. Schrijver, Kirsti Kauristie, Alan D. Aylward, Clezio M. Denardini, Sarah E. Gibson, Alexi Glover, Nat Gopalswamy, Manuel Grande, Mike Hapgood, Daniel Heynderickx, Norbert Jakowski, Vladimir V. Kalegaev, Giovanni Lapenta, Jon A. Linker, Siqing Liu, Cristina H. Mandrini, Ian R. Mann, Tsutomu Nagatsuma, Dibyendu Nandy, Takahiro Obara, T. Paul O'Brien, Terrance Onsager, Hermann J. Opgenoorth, Michael Terkildsen, Cesar E. Valladares, and Nicole Vilmer. Understanding space weather to shield society: A global road map for 2015–2025 commissioned by COSPAR and ILWS. *Advances in Space Research*, 55(12):2745–2807, jun 2015. doi: 10.1016/j.asr.2015.03.023. 3

Heinrich Schwabe and Hofrath Schwabe Herrn. Sonnen — Beobachtungen im Jahre 1843. *Astronomische Nachrichten*, 21(15):234–235, January 1844. ISSN 1521-3994. doi: 10.1002/asna.18440211505. 10

R. Schwenn, A. Dal Lago, E. Huttunen, and W. D. Gonzalez. The association of coronal mass ejections with their effects near the earth. *Annales Geophysicae*, 23 (3):1033–1059, March 2005. ISSN 1432-0576. doi: 10.5194/angeo-23-1033-2005. xxii, 80, 97, 108

N. R. Sheeley, Y.-M. Wang, S. H. Hawley, G. E. Brueckner, K. P. Dere, R. A. Howard, M. J. Koomen, C. M. Korendyke, D. J. Michels, S. E. Paswaters, D. G. Socker, O. C. St Cyr, D. Wang, P. L. Lamy, A. Llebaria, R. Schwenn, G. M. Simnett, S. Plunkett, and D. A. Biesecker. Measurements of Flow Speeds in the Corona Between 2 and 30 R⊙. *The Astrophysical Journal*, 484(1):472, July 1997. ISSN 0004-637X. doi: 10.1086/304338. 55

Michael Sheetz. SpaceX to lose as many as 40 Starlink satellites due to space storm, February 2022. 1

A. V. Shirochkov, L. N. Makarova, V. D. Nikolaeva, and A. L. Kotikov. The storm of March 1989 revisited: A fresh look at the event. *Advances in Space Research*, 55 (1):211–219, January 2015. ISSN 0273-1177. doi: 10.1016/j.asr.2014.09.010. 2

Sean C. Solomon, Ralph L. McNutt, Robert E. Gold, and Deborah L. Domingue. MESSENGER Mission Overview. *Space Science Reviews*, 131(1):3–39, August 2007. ISSN 1572-9672. doi: 10.1007/s11214-007-9247-6. 81

Shirsh Lata Soni, R. Selvakumaran, and R. Satheesh Thampi. Assessment of the arrival signatures of the March 2012 CME–CME interaction event with respect to Mercury, Venus, Earth, STEREO-B, and Mars locations. *Frontiers in Astronomy and Space Sciences*, 9, January 2023. ISSN 2296-987X. doi: 10.3389/fspas.2022.1049906. 84

E. A. Spiegel and J. P. Zahn. The solar tachocline. *Astronomy and Astrophysics*, 265: 106–114, November 1992. ISSN 0004-6361. ADS Bibcode: 1992A&A...265..106S. 7

Davor Sudar, Bojan Vršnak, and Mateja Dumbović. Predicting coronal mass ejections transit times to Earth with neural network. *Monthly Notices of the Royal Astronomical Society*, 456(2):1542–1548, February 2016. ISSN 0035-8711. doi: 10.1093/mnras/stv2782. 53

Erdogan Taskesen. Distfit is a python library for probability density fitting, 2023. 75, 116

M. Temmer. Kinematical properties of coronal mass ejections. *Astronomische Nachrichten*, 337(10):1010–1015, nov 2016. doi: 10.1002/asna.201612425. 21

M. Temmer and V. Bothmer. Characteristics and evolution of sheath and leading edge structures of interplanetary coronal mass ejections in the inner heliosphere based on Helios and Parker Solar Probe observations. *Astronomy and Astrophysics*, 665:A70, September 2022. ISSN 0004-6361. doi: 10.1051/0004-6361/202243291. ADS Bibcode: 2022A&A...665A..70T. xviii, 20

Manuela Temmer. Space weather: the solar perspective. *Living Reviews in Solar Physics*, 18(1), jun 2021. doi: 10.1007/s41116-021-00030-3. 17, 20, 21

Manuela Temmer, Tanja Rollett, Christian Möstl, Astrid M Veronig, Bojan Vršnak, and Dusan Odstrčil. Influence of the ambient solar wind flow on the propagation behavior of interplanetary coronal mass ejections. *The Astrophysical Journal*, 743 (2):101, November 2011. ISSN 0004-637X. doi: 10.1088/0004-637X/743/2/101. 58

Manuela Temmer, Bojan Vršnak, Tanja Rollett, Bianca Bein, Curt A. de Koning, Ying Liu, Eckhard Bosman, Jackie A. Davies, Christian Möstl, Tomislav Žic, Astrid M. Veronig, Volker Bothmer, Richard Harrison, Nariaki Nitta, Mario Bisi, Olga Flor, Jonathan Eastwood, Dusan Odstrcil, and Robert Forsyth. Characteristics of kinematics of a coronal mass ejection during the 2010 august 1 cme-cme interaction event. *The Astrophysical Journal*, 749(1):57, March 2012. ISSN 0004-637X. doi: 10.1088/0004-637X/749/1/57. 58

Manuela Temmer, Camilla Scolini, Ian G. Richardson, Stephan G. Heinemann, Evangelos Paouris, Angelos Vourlidas, Mario M. Bisi, N. Al-Haddad, T. Amerstorfer, L. Barnard, D. Buresova, S. J. Hofmeister, K. Iwai, B. V. Jackson, R. Jarolim, L. K. Jian, J. A. Linker, N. Lugaz, P. K. Manoharan, M. L. Mays, W. Mishra, M. J. Owens, E. Palmerio, B. Perri, J. Pomoell, R. F. Pinto, E. Samara, T. Singh, D. Sur, C. Verbeke, A. M. Veronig, and B. Zhuang. CME propagation through the heliosphere: Status and future of observations and model development. *Advances in Space Research*, July 2023. ISSN 0273-1177. doi: 10.1016/j.asr.2023.07.003. 53

A. Thernisien. IMPLEMENTATION OF THE GRADUATED CYLINDRICAL SHELL MODEL FOR THE THREE-DIMENSIONAL RECONSTRUCTION OF CORONAL MASS EJECTIONS. *The Astrophysical Journal Supplement Series*, 194(2):33, May 2011. ISSN 0067-0049. doi: 10.1088/0067-0049/194/2/33. 64, 101

A. Thernisien, A. Vourlidas, and R. A. Howard. Forward Modeling of Coronal Mass Ejections Using STEREO/SECCHI Data. *Solar Physics*, 256(1):111–130, May 2009. ISSN 1573-093X. doi: 10.1007/s11207-009-9346-5. 64

A. F. R. Thernisien, R. A. Howard, and A. Vourlidas. Modeling of Flux Rope Coronal Mass Ejections. *The Astrophysical Journal*, 652(1):763, November 2006. ISSN 0004-637X. doi: 10.1086/508254. 64, 101

Roger J. Thomas and Richard G. Teske. Solar soft X-rays and solar activity. *Solar Physics*, 16(2):431–453, February 1971. ISSN 1573-093X. doi: 10.1007/BF00162486. 16

Durgesh Tripathi, A. N. Ramaprakash, Aafaque Khan, Avyarthana Ghosh, Subhamoy Chatterjee, Dipankar Banerjee, Pravin Chordia, Achim Gandorfer, Natalie Krivova, Dibyendu Nandy, Chaitanya Rajarshi, and Sami K. Solanki. The Solar Ultraviolet Imaging Telescope on-board Aditya-L1. *Current Science*, 113:616, August 2017. doi: 10.18520/cs/v113/i04/616-619. ADS Bibcode: 2017CSci..113..616T. 38

Durgesh Tripathi, D. Chakrabarty, A. Nandi, B. Raghvendra Prasad, A. N. Ramaprakash, Nigar Shaji, K. Sankarasubramanian, R. Satheesh Thampi, and V. K. Yadav. The Aditya-L1 mission of ISRO. *Proceedings of the International Astronomical Union*, 372(S372):17–27, January 2023. ISSN 1743-9221. doi: 10.1017/S1743921323001230. ADS Bibcode: 2023IAUS..372...17T. 33

Bernard J. Vasquez, Charles J. Farrugia, Sergei A. Markovskii, Joseph V. Hollweg, Ian G. Richardson, Keith W. Ogilvie, Ronald P. Lepping, Robert P. Lin, and Davin Larson. Nature of fluctuations on directional discontinuities inside a solar ejection: Wind and IMP 8 observations. *Journal of Geophysical Research: Space Physics*, 106(A12):29283–29298, 2001. ISSN 2156-2202. doi: 10.1029/2001JA000142. 41

C. Verbeke, M. L. Mays, M. Temmer, S. Bingham, R. Steenburgh, M. Dumbović, M. Núñez, L. K. Jian, P. Hess, C. Wiegand, A. Taktakishvili, and J. Andries. Benchmarking cme arrival time and impact: Progress on metadata, metrics, and events. *Space Weather*, 17(1):6–26, 2019. ISSN 1542-7390. doi: 10.1029/2018SW002046. xxii, xxiv, 53, 103, 121, 122

Pauli Virtanen, Ralf Gommers, Travis E Oliphant, Matt Haberland, Tyler Reddy, David Cournapeau, Evgeni Burovski, Pearu Peterson, Warren Weckesser, Jonathan Bright, et al. Scipy 1.0: fundamental algorithms for scientific computing in python. *Nature methods*, 17(3):261–272, 2020. doi: https://dx.doi.org/10.1038/s41592-019-0686-2. 116

A Vourlidas, D Buzasi, RA Howard, and E Esfandiari. Mass and energy properties of lasco cmes. In *Solar variability: from core to outer frontiers*, volume 506, pages 91–94, 2002. 17

A. Vourlidas, S. Patsourakos, and N. P. Savani. Predicting the geoeffective properties of coronal mass ejections: current status, open issues and path forward. *Philosophical Transactions of the Royal Society A: Mathematical, Physical and Engineering Sciences*, 377(2148):20180096, may 2019. doi: 10.1098/rsta.2018.0096. 53

Angelos Vourlidas, Russell A. Howard, Simon P. Plunkett, Clarence M. Korendyke, Arnaud F. R. Thernisien, Dennis Wang, Nathan Rich, Michael T. Carter, Damien H. Chua, Dennis G. Socker, Mark G. Linton, Jeff S. Morrill, Sean Lynch, Adam Thurn, Peter Van Duyne, Robert Hagood, Greg Clifford, Phares J. Grey, Marco Velli, Paulett C. Liewer, Jeffrey R. Hall, Eric M. DeJong, Zoran Mikic, Pierre Rochus, Emanuel Mazy, Volker Bothmer, and Jens Rodmann. The Wide-Field Imager for Solar Probe Plus (WISPR). *Space Science Reviews*, 204(1):83–130, December 2016. ISSN 1572-9672. doi: 10.1007/s11214-014-0114-y. 40

B. Vršnak, T. Žic, T. V. Falkenberg, C. Möstl, S. Vennerstrom, and D. Vrbanec. The role of aerodynamic drag in propagation of interplanetary coronal mass ejections. *Astronomy and Astrophysics*, 512:A43, mar 2010. doi: 10.1051/0004-6361/200913482. 54, 58

B. Vršnak, M. Temmer, T. Žic, A. Taktakishvili, M. Dumbović, C. Möstl, A. M. Veronig, M. L. Mays, and D. Odstrčil. Heliospheric propagation of coronal mass ejections: Comparison of numerical wsa-enlil + cone model and analytical drag-based model. *The Astrophysical Journal Supplement Series*, 213(2):21, jul 2014. doi: 10.1088/0067-0049/213/2/21. 63

Bojan Vršnak. Deceleration of coronal mass ejections. *Solar Physics*, 202:173–189, 2001. 53

Bojan Vršnak and Nat Gopalswamy. Influence of the aerodynamic drag on the motion of interplanetary ejecta. *Journal of Geophysical Research: Space Physics*, 2002. doi: 10.1029/2001ja000120. 55

Bojan Vršnak and Tomislav Žic. Transit times of interplanetary coronal mass ejections and the solar wind speed. *Astronomy & Astrophysics*, 2007. doi: 10.1051/0004-6361:20077499. 55

Bojan Vršnak, Domagoj Ruždjak, Davor Sudar, and Nat Gopalswamy. Kinematics of coronal mass ejections between 2 and 30 solar radii - What can be learned about forces governing the eruption? *Astronomy & Astrophysics*, 423(2):717–728, August 2004. ISSN 0004-6361, 1432-0746. doi: 10.1051/0004-6361:20047169. 58

Bojan Vršnak, Tomislav Žic, Dijana Vrbanec, Manuela Temmer, Tanja Rollett, Christian Möstl, Astrid Veronig, Jaša Čalogović, Mateja Dumbović, Slaven Lulić, et al. Propagation of interplanetary coronal mass ejections: The drag-based model. *Solar physics*, 285(1-2):295–315, 2013. doi: 10.1007/s11207-012-0035-4. 22, 53, 58, 63, 69, 99

Shinichi Watari, Manabu Kunitake, and Takashi Watanabe. The bastille day 14 july 2000 event in historical large sun earth connection events. *Solar Physics*, 204(1): 425–438, December 2001. ISSN 1573-093X. doi: 10.1023/A:1014273227639. 2

David F. Webb and Russell A. Howard. The solar cycle variation of coronal mass ejections and the solar wind mass flux. *Journal of Geophysical Research: Space Physics*, 99(A3):4201–4220, 1994. ISSN 2156-2202. doi: 10.1029/93JA02742. 17, 18

David F. Webb and Timothy A. Howard. Coronal mass ejections: Observations. *Living Reviews in Solar Physics*, 9, 2012. doi: 10.12942/lrsp-2012-3. xviii, 17, 18, 21, 25, 26, 27, 31

Daniel S. Wilks. *Statistical Methods in the Atmospheric Sciences.* Academic Press, July 2011. ISBN 9780123850232. Google-Books-ID: fxPiH9Ef9VoC. 122

Robert M. Wilson. A comparison of wolf's reconstructed record of annual sunspot number with schwabe's observed record of 'clusters of spots' for the interval of 1826 1868. *Solar Physics*, 182:217–230, September 1998. ISSN 0038-0938. doi: 10.1023/A:1005046820210. ADS Bibcode: 1998SoPh..182..217W. 10

Reka M. Winslow, Noé Lugaz, Lydia C. Philpott, Nathan A. Schwadron, Charles J. Farrugia, Brian J. Anderson, and Charles W. Smith. Interplanetary coronal mass ejections from MESSENGER orbital observations at mercury. *Journal of Geophysical Research: Space Physics*, 120(8):6101–6118, aug 2015. doi: 10.1002/2015ja021200. 80, 81, 82, 118, 119

Reka M. Winslow, Noé Lugaz, Camilla Scolini, and Antoinette B. Galvin. First simultaneous in situ measurements of a coronal mass ejection by parker solar probe and STEREO-a. *The Astrophysical Journal*, 916(2):94, aug 2021. doi: 10.3847/1538-4357/ac0821. 84

O. Witasse, B. Sánchez-Cano, M. L. Mays, P. Kajdič, H. Opgenoorth, H. A. Elliott, I. G. Richardson, I. Zouganelis, J. Zender, R. F. Wimmer-Schweingruber, L. Turc, M. G. G. T. Taylor, E. Roussos, A. Rouillard, I. Richter, J. D. Richardson, R. Ramstad, G. Provan, A. Posner, J. J. Plaut, D. Odstrcil, H. Nilsson, P. Niemenen, S. E. Milan, K. Mandt, H. Lohf, M. Lester, J.-P. Lebreton, E. Kuulkers, N. Krupp, C. Koenders, M. K. James, D. Intzekara, M. Holmstrom, D. M. Hassler, B. E. S. Hall, J. Guo, R. Goldstein, C. Goetz, K. H. Glassmeier, V. Génot, H. Evans, J. Espley, N. J. T. Edberg, M. Dougherty, S. W. H. Cowley, J. Burch, E. Behar, S. Barabash, D. J. Andrews, and N. Altobelli. Interplanetary coronal mass ejection observed at STEREO-a, mars, comet 67p/churyumov-gerasimenko, saturn, and new horizons en route to pluto: Comparison of its forbush decreases at 1.4, 3.1, and 9.9 AU. *Journal of Geophysical Research: Space Physics*, 122(8):7865–7890, aug 2017. doi: 10.1002/2017ja023884. 80, 84

Wolf. Abstract of his latest results. *Monthly Notices of the Royal Astronomical Society*, 21(3):77–78, January 1861. ISSN 0035-8711. doi: 10.1093/mnras/21.3.77. 10

J. Zhang, W. Poomvises, and I. Richardson. Sizes and relative geoeffectiveness of interplanetary coronal mass ejections and the preceding shock sheaths during intense storms in 1996–2005. *Geophysical Research Letters*, 35, 2008. doi: 10.1029/2007GL032045. 80

Dan Zhao, Jianpeng Guo, Hui Huang, Haibo Lin, Yichun Hong, Xueshang Feng, Jun Cui, Yong Wei, Yang Wang, Yongyong Feng, Lei Li, and Libo Liu. Interplanetary Coronal Mass Ejections from MAVEN Orbital Observations at Mars. *The Astrophysical Journal*, 923(1):4, December 2021. ISSN 0004-637X. doi: 10.3847/1538-4357/ac294b. 80, 82, 83

Xinhua Zhao and Murray Dryer. Current status of cme/shock arrival time prediction. *Space Weather*, 12(7):448–469, jul 2014. doi: 10.1002/2014sw001060. 53, 118, 119

Thomas H. Zurbuchen and Ian G. Richardson. In-situ solar wind and magnetic field signatures of interplanetary coronal mass ejections. *Space Science Reviews*, 123 (1-3):31–43, sep 2006. doi: 10.1007/s11214-006-9010-4. xxiii, 41, 43

This publication is part of the Space Weather Awareness Training Network (SWATNet), which has received funding from the European Union's Horizon 2020 research and innovation programme under the Marie Skłodowska-Curie Innovative Training Networks, Grant Agreement No 955620. The publication reflects only the author's view and does not represent the opinion of the European Commission (EC), and the EC is not responsible for any use that might be made of the information contained.

Design Credit: @sanchwho

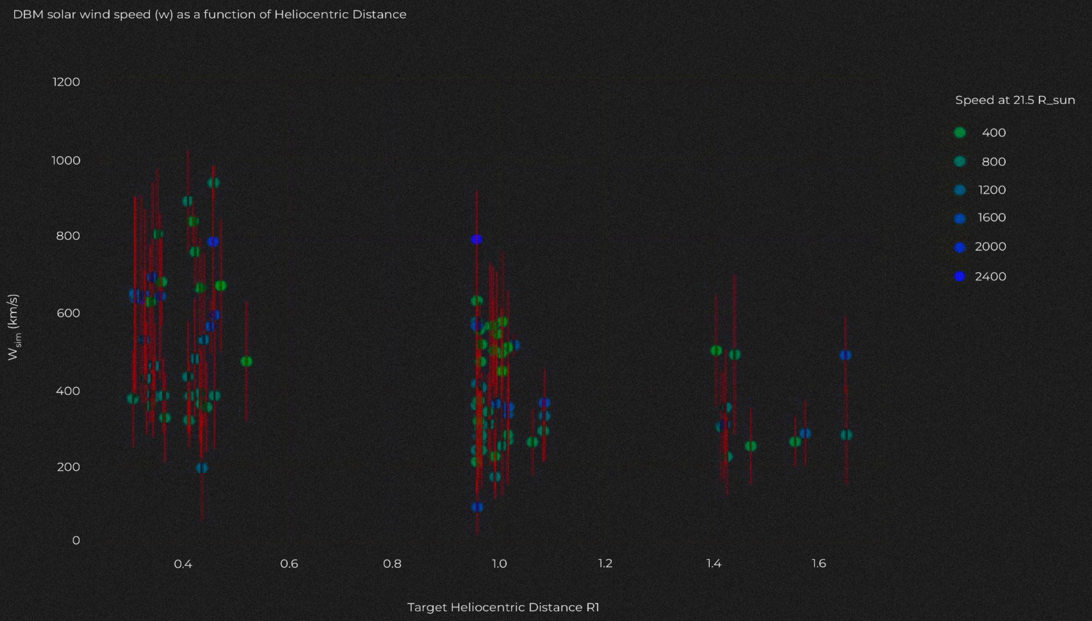

The plot illustrates the fluctuations in modelled solar wind speed as a function of heliocentric distance.

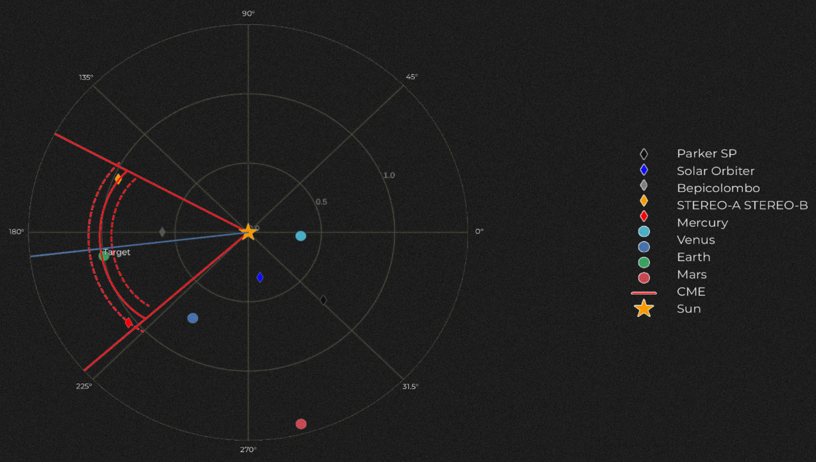

The simulated ICME edge at the time of arrival at the target using P-DBM is illustrated.The red solid line represents the ICME edge associated with the mean value of ICME arrival time.On the other hand, the dashed line indicates the uncertainty in the forecast.

This thesis contributes to the field of space weather forecasting by enhancing the prediction of Coronal Mass Ejection (CME) arrival times using the Probabilistic Drag-Based Model (P-DBM). By building robust catalogues of geo-effective CME-ICME events and extending CME tracking beyond 1 AU using in-situ and remote observations from multiple spacecraft, the thesis evaluates the variability of solar wind drag and CME parameters across heliocentric distances, presenting a semi-empirical framework with improved statistical accuracy.

University of Sheffield

SWATNet

TOR VERGATA
UNIVERSITÀ DEGLI STUDI DI ROMA